Kinematic variables and feature engineering for particle phenomenology

Roberto Franceschini[*]

Università degli Studi Roma Tre and INFN Roma Tre, Via della Vasca Navale 84, I-00146 Roma, Italy

Doojin Kim[†]

Mitchell Institute for Fundamental Physics and Astronomy, Department of Physics and Astronomy, Texas A&M University, College Station, Texas 77843, USA

Kyoungchul Kong[‡]

Department of Physics and Astronomy, University of Kansas, Lawrence, Kansas 66045, USA

Konstantin T. Matchev[§]

Institute for Fundamental Theory, Physics Department, University of Florida, Gainesville, Florida 32611, USA

Myeonghun Park[‖]

School of Natural Sciences, Seoultech, 232 Gongneung-ro, Nowon-gu, Seoul, 01811, Korea and School of Physics, KIAS, Seoul 02455, Korea

Prasanth Shyamsundar[¶]

Fermilab Quantum Institute, Fermi National Accelerator Laboratory, Batavia, Illinois 60510, USA

(published 21 November 2023)

Kinematic variables play an important role in collider phenomenology, as they expedite discoveries of new particles by separating signal events from unwanted background events and allow for measurements of particle properties such as masses, couplings, and spins. For the past ten years, an enormous number of kinematic variables have been designed and proposed, primarily for the experiments at the CERN Large Hadron Collider, allowing for a drastic reduction of high-dimensional experimental data to lower-dimensional observables, from which one can readily extract underlying features of phase space and develop better-optimized data-analysis strategies. Recent developments in the area of phase-space kinematics are reviewd, and new kinematic variables with important phenomenological implications and physics applications are summarized. Recently proposed analysis methods and techniques specifically designed to leverage new kinematic variables are also reviewed. As machine learning is currently percolating through many fields of particle physics, including collider phenomenology, the interconnection and mutual complementarity of kinematic variables and machine-learning techniques are discussed. Finally, the manner in which utilization of kinematic variables originally developed for colliders can be extended to other high-energy physics experiments, including neutrino experiments, is discussed.

DOI: 10.1103/RevModPhys.95.045004

[*]roberto.franceschini@uniroma3.it
[†]doojin.kim@tamu.edu
[‡]kckong@ku.edu
[§]matchev@ufl.edu
[‖]parc.seoultech@seoultech.ac.kr
[¶]prasanth@fnal.gov

CONTENTS

I. Introduction 2
A. The curse of dimensionality and the zoo of kinematic variables 2
B. Goal, scope, and organization 2
II. Kinematic Variable Run-Through 3
A. Preprocessing of the input data 3
B. Constructing kinematic variables and the associated challenges 4

C. Typical uses and applications 5
III. Standard Kinematic Information 5
A. Conventions and notation 5
B. Simple kinematic observables 6
IV. Inclusive Event Variables 7
A. Event-shape-type variables 7
B. Missing momentum 10
C. Variables sensitive to the overall energy scale 11
V. Exclusive Event Variables: Invariant Mass 11
A. Mass variables of collections of visible particles 12
B. Mass variables of semi-invisible collections of particles 15
1. One invisible daughter particle 15
2. Two invisible daughter particles 16
C. Singularity variables 20
VI. Exclusive Event Variables: Energy, Time, and Distance 21
A. Energy peak 21
B. Timing 23
C. Distance variables 24
VII. Other Exclusive Event Variables 25
A. Dimensionless variables 25
B. ISR methods 27
VIII. Variables and Methods Using Ensembles of Events 29
A. Polynomial method 29
B. Focus-point method 30
C. Kinematic end-point methods 30
D. Matrix-element and likelihood methods 32
E. Edge detection 32
F. Interference effects 33
IX. Kinematic Variables in the Machine-Learning Era 34
A. Feature engineering 34
B. Domain-inspired machine learning 34
C. Interpretability and explainability 35
D. Advantage of quantum computation for identifying event topologies 35
X. Kinematic Variables in Different Experiments 35
XI. Conclusions and Outlook 37
Acknowledgments 38
Appendix A: Real-World Challenges 38
1. Experimental uncertainties 38
2. Theoretical uncertainties 38
Appendix B: Real-World Examples: W and Top Physics 39
1. W-boson mass (m_W) 40
2. Top quark mass (m_t) 40
Appendix C: Tools and Codes for Kinematic Variables 44
References 44

I. INTRODUCTION

The defining objective of particle physics is to understand the elementary constituents of our Universe and their interactions at the most fundamental level. Advancing our understanding of nature at the smallest possible scales requires in turn extraordinarily large and complex particle physics experiments. For example, the Large Hadron Collider (LHC) at CERN is not only the largest man-made experiment on Earth but also the most prolific producer of scientific data. The data delivery rate at its upcoming upgrade, the High-Luminosity LHC (HL-LHC), will increase 100-fold to about 1 exabyte per year, bringing quantitatively and qualitatively new challenges due to its event size, data volume, and complexity, thereby straining the available computational resources. New particle physics discoveries in this era of big data will be possible only with novel methods of data collection, processing, and analysis.

A. The curse of dimensionality and the zoo of kinematic variables

Modern particle physics data are extremely high dimensional: typical events result in multiple (∼1000) particles in the final state. The dimensionality of the data will increase even further at the HL-LHC. Ideally, one wants to make use of the full information encoded in the raw experimental data, but this approach would run into serious challenges.

- From a theorist's point of view, the ultimate goal is to understand the fundamental laws of nature at the microscopic level. However, it is highly nontrivial to decipher the underlying physics and/or develop physical intuition by looking at the raw data.
- From a practitioner's point of view, working with the full raw dataset quickly becomes computationally prohibitive as the dimensionality of the data increases (Albertsson *et al.*, 2018).

Given the size and nature of the experimental dataset, modern particle physics analyses inevitably involve some kind of dimensionality reduction to fewer variables (features), which are suitably chosen to be optimal for the goal of the particular experiment. These higher-level variables are derived from the measured particle kinematic information, and therefore are generically referred to as kinematic variables; see Fig. 1. There is no unique or "best" way to perform this dimensional reduction: the perceived benefits of any given technique depend on a variety of factors, for instance, the experimental signature, the goal of the analysis, the control over the physics and instrumental backgrounds, and finally one's judging criteria, which can be subjective to begin with.

Moreover, if the final state contains invisible particles such as neutrinos and dark-matter candidates that appear to be missing energy, their treatment opens the door for many new possibilities. This is why numerous different approaches have been tried, and as a result a great number of kinematic variables have been proposed and investigated in the literature. The systematic organization and presentation of all of the different approaches to dealing with missing energy events is one of the main goals of this review. Depending on the underlying event topology and the target study point, they may show different levels of performance and capability (i.e., no single variable exhibits absolute superiority over the others); hence, it is prudent to keep as many tools as possible in the analysis toolbox.

B. Goal, scope, and organization

This review provides a comprehensive guide to commonly used kinematic variables, with a special focus on developments within the last decade. The review is important and timely for the following reasons:

- *A comprehensive list of kinematic variables*.—Kinematic variables are routinely used in experiments to search for new signals, as well as to perform parameter measurements in observed processes. The use of the right kinematic variables can expedite the discovery of

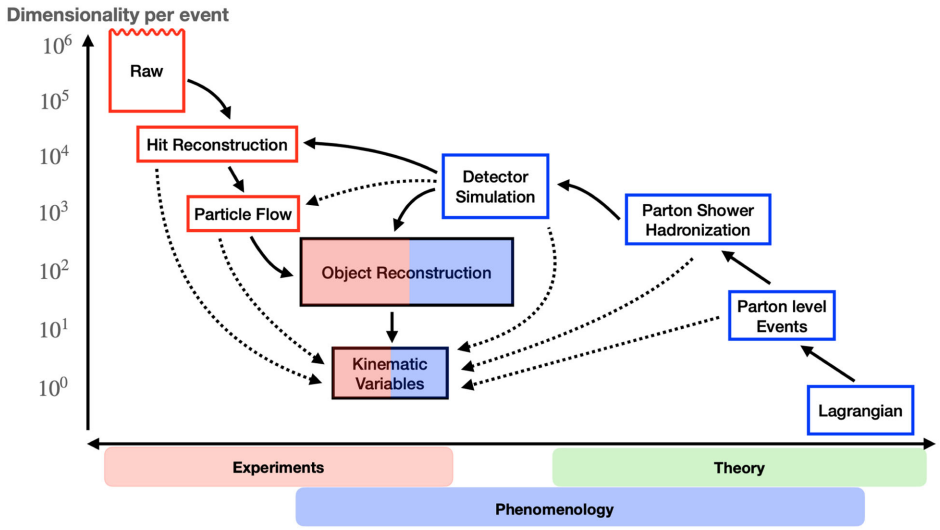

FIG. 1. Illustration of the dimensionality reduction in collider experiments and phenomenological studies. The common goal is to find the optimal low-dimensional kinematic observables. On the experimental side (the red boxes on the left) this is accomplished by reconstructing the low-level detector data into progressively more physically motivated quantities. On the theory side (the blue boxes on the right) the kinematic variables (or features in their distributions) are meant to reflect fundamental parameters in the theory Lagrangian. The solid (dotted) arrows indicate the typical flow (simplifying shortcuts) in the high-energy physics simulation chain.

new physics and can increase the sensitivity to a given parameter. This review provides a comprehensive menu from which practitioners can either pick existing kinematic variables that are the right ones for their task or derive new kinematic variables following the methodology presented here.

- *Feature engineering*.—Broadly speaking, feature engineering is the process of using domain knowledge to extract features from raw data. This is precisely the idea behind the kinematic variables described in this review: they are the result of "feature engineering" of the simple kinematic observables in the event described in Sec. III.B. In a more narrow sense, feature engineering is a main ingredient of machine learning (ML), which is now increasingly being used for data analysis in high-energy physics. It is known that the performance and the training efficiency of the ML algorithms crucially depend on the parametrization of the input features. Using the correct kinematic variables to describe the data would greatly enhance the performance of machine-learning techniques in analyzing the data. Finding the proper balance between attributes of the data that one wants to be sensitive to and those that are irrelevant to the question at hand is an art. This review can thus be used either to optimize the input for various machine-learning algorithms and tasks or to properly interpret the output from the machine in terms of human-engineered kinematic quantities.
- *The need for an up-to-date review*.—The last such review of comparable scope was written more than ten years ago (Barr and Lester, 2010), before extensive experience analyzing LHC data was gained. There are also several sets of pedagogical lectures targeting newcomers in the field that focus on standard material (Han, 2005; Perelstein, 2011; Schwartz, 2018). A few other reviews, more limited in scope, have appeared as well, focusing on, for instance, energy peaks (Franceschini, 2017) or minimum invariant mass bounds (Barr, Khoo *et al.*, 2011).

The organization of the review is as follows. Section II provides the necessary background, motivation, and context for the construction of kinematic variables. Our conventions and notation for the particle kinematics are then presented in Sec. III.A. Some basic kinematic observables are reviewed in Sec. III.B. In Sec. IV (Secs. V–VII) we describe inclusive (exclusive) event variables used to characterize a *single event*. Variables and methods relying on *ensembles of events* are discussed in Sec. VIII. The interplay between the classic kinematic methods and the more recent machine-learning approaches is discussed in Sec. IX. Section X contains examples of kinematic variables that are experiment specific, while Sec. XI is reserved for conclusions and an outlook. Appendix A reviews the experimental and theoretical challenges often encountered when one constructs and uses the kinematic variables discussed in the main text. Appendix B illustrates those ideas with a couple of real-life examples from top and W physics. Appendix C provides a guide to some commonly used tools and codes for kinematic variables.

II. KINEMATIC VARIABLE RUN-THROUGH

A. Preprocessing of the input data

The primary objective of a particle physics experiment is to test a theory model, which is usually encoded in a Lagrangian in quantum field theory. As depicted on the rightmost side of Fig. 1, one can then use this Lagrangian to predict the kinematic distributions of relevant quantities of interest (Ask *et al.*, 2012). This is a relatively straightforward procedure that takes advantage of established theoretical tools like the perturbative expansion in quantum field theory.

However, this can be done only at the parton level, i.e., in terms of the fundamental particles represented by the fields appearing in the Lagrangian. Therefore, a necessary step in any analysis is to measure the four-momenta of the fundamental particles emerging from the hard collision.

For leptons like electrons and muons, this is relatively easy since the object measured in the detector represents the fundamental particle itself. For tau leptons, the situation is a bit more complicated since taus can be identified only through their hadronic decays, in which there is a neutrino missing. However, the greatest challenge is presented by colored partons (quarks and gluons), which are observed as streams of hadrons called jets. The parton showering and hadronization processes are described by taking limits of perturbative QCD and by phenomenological models implemented in the general purpose event generators. Jet reconstruction algorithms are then needed to cluster the particles observed in the detector into individual jets, and thus to obtain the jet four-momenta, which can be related to the four-momenta of the underlying partons. Ultimately, as a result of the so-called object reconstruction procedure (see Fig. 1), one ends up with a set of four-momenta for the relevant fundamental particles in the event.[1] These four-momenta serve as the basis for constructing the kinematic variables discussed in this review. Each kinematic variable is a certain mapping f from the measured four-momenta to a single, typically scalar quantity. However, there are some practical challenges in defining the proper mapping f, as discussed next.

B. Constructing kinematic variables and the associated challenges

In the construction of any derived kinematic quantity, in general one may encounter a number of practical problems, as we now discuss.

Particle identification and reconstruction.—Object reconstruction involves a set of criteria applied on the low-level data, for example, the presence or absence of a track, the ratio of the energy deposits in the electromagnetic and hadronic calorimeter, and isolation requirements. In principle, particle identification and reconstruction are never perfect: sometimes the "wrong" types of particles may pass the requirements, leading to fake leptons, fake photons, etc. This is a potential problem in the construction of exclusive kinematic variables, which assume a certain event topology and therefore are defined in terms of the momenta of the correspondingly identified objects.

Combinatorial problem.—Whenever the final state contains several reconstructed objects of the same type, it is not clear how to associate reconstructed objects with their parton-level counterparts. This problem is known as combinatorial ambiguity and must be considered in the construction and interpretation of kinematic variables. All possible assignments must be taken into account, though one might use the fact that some assignments are more likely than others. The problem arises whenever the final state contains several reconstructed objects of the same type. The association of reconstructed objects at the detector level with their parton-level counterparts is not unique, and one has to deal with the resulting combinatorial ambiguity. The problem is exacerbated by the fact that several types of partons, namely, the light quarks and the gluons, yield jets that appear to be similar in the detector and can be discriminated only on a statistical basis (CMS Collaboration, 2013b; Aad *et al.*, 2014; Komiske, Metodiev, and Schwartz, 2017). In most practical applications, the combinatorial problem manifests itself as a partitioning ambiguity whenever we try to select the decay products of a common parent particle. For example, in the case of pair production of two parent particles, the reconstructed objects need to be separated into two groups, for instance, with the hemisphere method (Bayatian *et al.*, 2007; Matsumoto, Nojiri, and Nomura, 2007). Lester and Barr (2007) and Alwall *et al.* (2009) extended this idea to account for jets from initial-state radiation, which are considered a separate category. Other techniques to mitigate the combinatorial problem include event mixing (Albrow *et al.*, 1976), mixed event subtraction (Hinchliffe *et al.*, 1997; Agashe, Franceschini, Kim, and Wardlow, 2016), the use of ranked variables (Kim, Matchev, and Park, 2016), and the recursive jigsaw reconstruction method (Jackson and Rogan, 2017). Since different partitions of the final-state objects typically result in different values for the kinematic variables, one could use this to select the correct partition. Specific applications of this idea to the dilepton $t\bar{t}$ event topology using M_{T2} and the constrained M_2 variable were considered by Baringer *et al.* (2011) and Debnath, Kim *et al.* (2017), respectively.

Imperfect detectors.—The observed experimental objects and their kinematics can be different than the actual event due to imperfect detectors. Similarly, the observed objects can differ from the simulated Monte Carlo truth, which necessitates the detector simulation stage in the Monte Carlo chain depicted in Fig. 1. The measured energies, momenta, and timing are generally smeared from their parton-level values. While this is not necessarily a roadblock for the calculation of the kinematic variables *per se*, it should be kept in mind when interpreting the results. The more serious problem, as previously mentioned, is the misidentification of particles: for instance, imperfect b tagging would lead to additional b-tagged jets. This would contribute to the combinatorial problem of selecting the correct b jet to associate with a b-quark parton in the interpretation of the event. Finally, an important variable, used either by itself or in the construction of many kinematic variables, is the missing transverse momentum, which is defined as the transverse recoil against all visible objects in the event. Because it relies on the use of all observed objects, the missing transverse momentum is especially susceptible to mismeasurement.

Unknown new physics parameters.—For new-physics signals, one does not know *a priori* the values of the new model parameters, for instance, the mass of a dark-matter candidate. In such cases, the definitions of the kinematic variables often involve a test value for the corresponding parameter that needs to be chosen judiciously. In what follows, we use a tilde to

[1]Recently there have been suggestions to bypass the "object reconstruction" stage altogether and directly leverage low-level data. Examples include end-to-end analyses (Andrews, Alison *et al.*, 2020; Andrews, Paulini *et al.*, 2020), the use of jet images (Cogan *et al.*, 2015; Kagan, 2022), etc.

denote such trial parameter values, for example, $\tilde{m}$ for the mass of a dark-matter candidate.

Multiple solutions.—Whenever the kinematic variables are constructed as the solutions of nonlinear constraint equations, there may appear multiple solutions, and one must then design a suitable procedure to arrive at a unique answer. For example, solving for the longitudinal momentum of an unobserved neutrino typically leads to multiple solutions.

Depending on the case at hand, there are different approaches to tackling these problems. For the most part, in this review we take a theorist's viewpoint and consider idealized measurements of the particle energies and momenta in order to simplify the description of the increasingly sophisticated variables used in the experiments. In Appendix A we discuss how the realities of experimental measurements affect these idealized analyses.

C. Typical uses and applications

In analogy to the "no free lunch theorem" in machine learning, no single kinematic variable is optimal for all conceivable tasks in particle phenomenology. Even if we fix the task, the optimal variable can change with time, depending, for instance, on the running conditions of the experiments or the evolution in our theoretical understanding of the background processes. This is why a great number of kinematic variables have been considered in the recent literature, with a wide range of applications, including the following:

- Carefully chosen kinematic variables are often used for signal versus background discrimination in new-physics searches. The choice of variable(s) is tied up to the hypothesized event topology (typically in the form of a simplified model). The ideal variable would capture the salient features of the process at hand and would not be too sensitive to the full details of the underlying new-physics model.
- Kinematic variables are key inputs to modern multivariate analyses, including machine-learning approaches; see Sec. IX
- Known kinematic variables can be used to define new, higher-level kinematic variables, for instance, using the existing correlations between different variables (Allanach *et al.*, 2000) or incorporating them into the algorithmic definition (Lester and Summers, 1999).
- Kinematic variables can be used to identify events with special kinematics. For example, one can place cuts on the value of the M_{T2} kinematic variable to select a subsample of events in which the true momenta of the invisible particles are fully determined (Cho *et al.*, 2009; Kim *et al.*, 2017).
- Certain kinematic variables can be used to test and validate the results from alternative machine-learning approaches (Kim *et al.*, 2023).
- The distributions of some kinematic variables exhibit features (bumps, edges, kinks, cusps, etc.) and/or shapes that can be directly correlated with fundamental parameters in the theory Lagrangian (Hinchliffe *et al.*, 1997; Burns *et al.*, 2008; Cho *et al.*, 2008a; Han, Kim, and Song, 2010). We devote considerable space to discussions of this point in Sec. V.

III. STANDARD KINEMATIC INFORMATION

A. Conventions and notation

Collider experiments usually employ a Cartesian coordinate system in which the z axis is aligned with the beam direction, while the x and y axes define the transverse plane orthogonal to the beam; see Fig. 2. For example, in this system a particle's three-momentum $\vec{p} \equiv (p_x, p_y, p_z)$ is decomposed into a longitudinal component p_z along the z axis and a transverse component $\vec{p}_T \equiv (p_x, p_y)$ within the transverse plane. As shown in Fig. 2, some of these Cartesian components can be traded for the magnitude of the transverse momentum

$$p_T \equiv \sqrt{p_x^2 + p_y^2}, \tag{1}$$

the azimuthal angle φ defined as

$$\varphi \equiv \tan^{-1}\left(\frac{p_y}{p_x}\right) \in [0, 2\pi), \tag{2}$$

and/or the polar angle θ defined as

$$\theta \equiv \tan^{-1}\left(\frac{p_T}{p_z}\right) \in [0, \pi]. \tag{3}$$

The energy E and three-momentum $\vec{p}$ of a particle form a four-vector $p^\mu = (E, \vec{p})$ whose $(1+3)$-dimensional components are denoted with midalphabet greek indices. The invariant mass m is then defined as

$$m \equiv \sqrt{p^\mu p_\mu} = \sqrt{E^2 - \vec{p}^2}. \tag{4}$$

By analogy, the transverse energy $E_T \equiv \sqrt{m^2 + p_T^2}$ and the transverse momentum $\vec{p}_T$ form a $(1+2)$-dimensional vector $p^\alpha = (E_T, \vec{p}_T)$, whose components are denoted with greek letters from the beginning of the alphabet.

The energy E and the longitudinal momentum component p_z can be used to define the rapidity

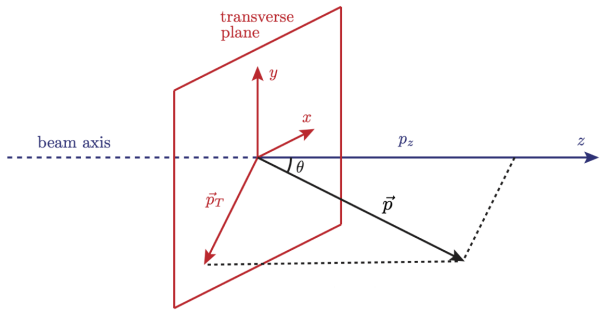

FIG. 2. The standard geometry of a collider experiment. The z axis (in blue) is oriented along the beam, while the x and y axes (in red) define the transverse plane. Any three-dimensional vector $\vec{p}$ can be uniquely decomposed into a longitudinal component p_z and a transverse component $\vec{p}_T$. From Barr, Khoo *et al.*, 2011.

$$y \equiv \frac{1}{2}\ln\left(\frac{E+p_z}{E-p_z}\right). \tag{5}$$

The pseudorapidity

$$\eta \equiv \frac{1}{2}\ln\left(\frac{1+\cos\theta}{1-\cos\theta}\right) = -\ln\left[\tan\left(\frac{\theta}{2}\right)\right] \tag{6}$$

is the limit of Eq. (5) for a massless particle. This is simpler to measure since it depends only on the angle of a track in the detector. At the LHC, it is almost always a good approximation to use the pseudorapidity as a surrogate for the rapidity for tracks of pions, kaons, and even protons and well-collimated jets.

In what follows, we use p to denote momenta of visible particles seen in the detector, while q is reserved for the momenta of invisible particles (dark-matter candidates, neutrinos, or other long-lived weakly interacting particles). Since many of the issues in this review account for invisible particles, it is worth paying close attention to this notational distinction.

In a collider experiment, the transverse momentum of the initial state is zero, which places a constraint on the final-state transverse momenta,

$$\sum_a \vec{p}_{aT} + \sum_b \vec{q}_{bT} = 0, \tag{7}$$

where the second term denotes a vectorial sum of the transverse momenta of invisible final-state particles. The measured total missing transverse momentum $\vec{\not{p}}_T$ is therefore given by

$$\vec{\not{p}}_T \equiv \sum_b \vec{q}_{bT} = -\sum_a \vec{p}_{aT}. \tag{8}$$

See also Sec. IV.B for more discussion.

At lepton colliders, the center-of-mass energy $\sqrt{s}$ is fixed and the longitudinal momentum of the initial state is also fixed (often zero). At hadron colliders, the parton-level center-of-mass energy $\sqrt{\hat{s}}$ varies from one event to the next, and the longitudinal momentum of the initial state is *a priori* unknown. This encourages the use of kinematic variables like Eqs. (5) and (6) that have convenient transformation properties under longitudinal Lorentz boosts (along the z axis).

Individual final-state particles are labeled $a, b, c, \ldots$. Collections of such particles (which are hypothesized to have a common origin) are labeled $A, B, C, \ldots$; see Fig. 3. Let $A = \{a_1, a_2, a_3, \ldots\}$ be a collection of final-state particles. The four-momentum of the entire collection is p_A^μ, while the four-momenta of the individual particles is denoted as $p_{a_i}^\mu$ or $q_{a_i}^\mu$, respectively, depending on whether the particle is visible or invisible. We use a lowercase m for the masses of final-state particles and an uppercase M for the kinematic mass variables, which typically are related to the masses of parent collections $A, B, C, \ldots$. Taking jets and leptons to be massless ($m = 0$) is usually a good approximation, but for W, Z, t, and dark-matter candidates we keep the explicit dependence on m. In the case of invisible final-state particles, as mentioned, it is often useful to treat their mass as a test parameter [denoted with a tilde ($\tilde{m}_\chi$)], regardless of whether the true mass is known or not.

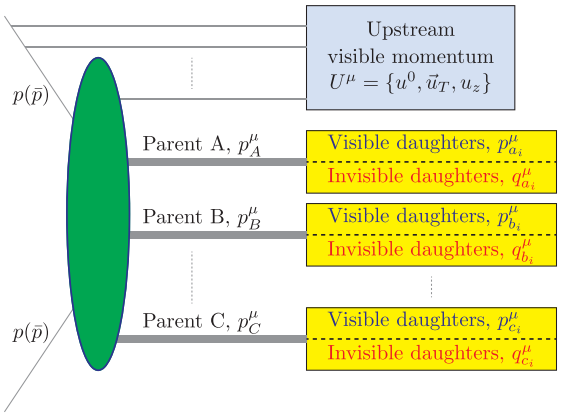

FIG. 3. The generic event topology of a collider event. The result of the initial collision (for definitiveness, we show the case of hadron colliders where the beams consist of protons p or antiprotons $\bar{p}$) is a set of final-state particles that can be grouped into collections $A, B, C, \ldots$, each containing sets of visible and invisible daughters. Adapted from Barr, Khoo *et al.*, 2011.

As shown in Fig. 3, we use U to denote the collection of particles that are not assigned to any other groups. In practice, they arise from initial-state radiation (ISR) or from decays upstream.[2]

B. Simple kinematic observables

The standard kinematic information is what is directly measured by detectors for individual particles reconstructed using particle flow; see the left side of Fig. 1. The four-momenta of the particles can be represented in Cartesian coordinates (E, p_x, p_y, p_z) or, more commonly, in cylindrical coordinates (E, p_T, φ, p_z), where p_z can also be traded for the pseudorapidity that preserves relative distance under longitudinal boosts. This kinematic information can then be compared to the expected distributions from a given theory model, which are typically done at the parton level; see the right side of Fig. 1. Therefore, one wants to match the particles observed in the detector with the fundamental parton-level particles in the standard model (SM).

- For nonhadronic particles that are stable on the detector scale (electrons, muons, and photons), this correspondence is direct.
- Neutrinos, on the other hand, are invisible and not reconstructed individually. Nevertheless, the sum of their momenta can be inferred from the imbalance between the four-momentum of the initial and final states in the event; see Sec. IV.B.
- The case of hadronic particles is much more complicated due to confinement; the quarks and gluons at the parton level appear to be collections of hadrons ("jets"), which necessitates jet reconstruction algorithms to recover the parton-level information. The situation is even more complicated due to the presence of initial- and final-state

[2]As explained in Sec. V.B, ungrouped particles downstream can be effectively eliminated from the discussion by introducing the intermediate resonances as effective invisible particles.

radiation, which results in additional jets that further muddle the picture. In a typical jet reconstruction algorithm, particles are grouped based on their relative distance in some suitably chosen metric, for instance, $\Delta R = \sqrt{\Delta\eta^2 + \Delta\varphi^2}$ in the (η, φ) space, where $\Delta\eta$ and $\Delta\varphi$ are the differences in the pseudorapidities and the azimuthal angles of the two objects, respectively.

- The heavy particles in the SM (W, Z, Higgs, and top) are then reconstructed probabilistically by grouping their decay products as illustrated in Fig. 3 and demanding that the invariant mass of the respective collection of decay products be consistent with the mass of the parent particle.

Additional variables that could be used to place cuts on select events are the number of reconstructed objects from each type: $N_j, N_b, N_{\ell}, N_e, N_\mu, N_\tau, N_\gamma$.

In a traditional cut-and-count analysis, one would (i) narrow down the number of variables to consider (dimensionality reduction), (ii) place cuts on them to define a signal region, and (iii) perform a counting experiment in the signal region. This dimensionality reduction, however, necessarily leads to some information loss. The goal of the experimenter is to utilize kinematic variables that minimize the information loss. In practice, the following two approaches (or a combination thereof) have been used:

- Make direct use of some of the previously described simple kinematic variables, including p_T, pseudorapidity, ΔR, invariant mass of a collection of particles, and the number of reconstructed objects of a given type. One could even imagine using all of the kinematic information from the event as an input to a machine-learning algorithm like a neural network classifier; see Sec. IX.
- Perform the dimensionality reduction in a more optimal way by forming suitable high-level kinematic variables, which are functions of the simple observables, and retain as much of the relevant information as possible. The main purpose of this review is to examine precisely these types of observables.

The interplay between those two approaches illustrates the tension between optimality and generalizability. The simple kinematic variables are robust and universally applicable (model independent) but not as sensitive. The high-level variables bring about higher sensitivity and physics performance but are not easily generalizable to other signal processes. With either approach, one must connect the kinematic measurements to the parton-level kinematics. This "unfolding" needs to overcome the two classes of challenges discussed in Appendix A.

IV. INCLUSIVE EVENT VARIABLES

In this section we focus on inclusive kinematic variables. They are robust and model independent since one does not make any assumptions about the underlying event topology. The downside is that they are not as sensitive to specific signals as their exclusive cousins, discussed in Secs. V–VII, which are intentionally designed to look for such signals. Nevertheless, owing to their simplicity, inclusive variables have proven to be valuable and have found wide usage at both the trigger and the analysis level.

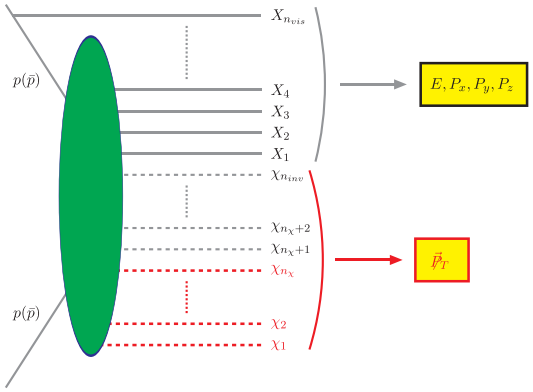

FIG. 4. Generic event topology illustrating the use of inclusive event variables from Sec. IV. From Konar, Kong, and Matchev, 2009.

Inclusive event variables are applicable to a generic event topology that is shown in Fig. 4. Unlike the case of Fig. 3, here we make no assumptions about the underlying process; hence, there is no partitioning of the final-state particles other than dividing them into visible (solid lines) and invisible (dashed lines). The black solid lines correspond to SM particles that are visible in the detector such as jets, electrons, muons, and photons. The SM particles may originate either from initial-state radiation or from the hard scattering and subsequent cascade decays (indicated by the green-shaded ellipse). The dashed lines denote neutral stable particles that are invisible in the detector. In general the set of invisible particles consists of some number of SM neutrinos (denoted with the black dashed lines), as well as some number of beyond-the-standard-model (BSM) particles (indicated as red dashed lines) that could be dark-matter candidates. The identities and the masses of the BSM invisible particles do not all necessarily have to be the same,[3] allowing for the simultaneous production of several different species of dark-matter particles. A few global event variables describing the visible particles are the total energy E, the transverse components P_x and P_y, and the longitudinal component P_z of the total visible momentum $\vec{P}$. The only experimentally available information regarding the invisible particles is the missing transverse momentum $\vec{p}_T$.

A. Event-shape-type variables

In this section, we review some classic event shape variables summarized in Table I. Other modern approaches involving jet-substructure variables were reviewed by Maltoni *et al.* (2022) and Nachman *et al.* (2022). The basic idea of the event shape variables is to give more information than just the cross section by defining the "shape" of an event (pencil-like, planar, spherical, etc.) (Banfi, Salam, and Zanderighi, 2010). Event shape variables describe the patterns and correlations of energy flow resulting from the particle collisions.

[3]Examples of particles with an effectively continuous mass spectrum include unparticles (Cheung, Keung, and Yuan, 2007; Georgi, 2007) and Kaluza-Klein gravitons in models with large extra dimensions (Arkani-Hamed, Dimopoulos, and Dvali, 1998; Mirabelli, Perelstein, and Peskin, 1999).

TABLE I. Summary of event shape variables in their definition, typical values, and associated references inspired by Fabio Maltoni's lecture (Maltoni, 2013) given at the 2013 CERN–Latin-American School of High-Energy Physics (Mulders and Perez, 2015). The first and second columns list the name and definition of the respective variable, while the defining reference is listed in the last column. Whenever applicable, the third column lists the value of the variable for the ideal cases of one-dimensional [pencil-like (Pen.)], two-dimensional [coplanar (Copl.)], and three-dimensional [isotropically symmetric (Iso.)] event topologies.

Observable	Definition	Typical values for Pen.	Copl.	Iso.	Reference(s)
Sphericity	$S = (3/2)(\lambda_2 + \lambda_3)$, $\lambda_i(\lambda_1 \geq \lambda_2 \geq \lambda_3)$, eigenvalues of $M_{ij} = \sum_{a=1}^{n_j} p_{a,i} p_{a,j} / \sum_{a=1}^{n_j} \lvert\vec{p}_a\rvert^2$, with $i, j \in \{x, y, z\}$	0	$\leq 3/4$	≤ 1	Bjorken and Brodsky (1970)
Transverse sphericity	$S_T = 2\lambda_2/(\lambda_1 + \lambda_2)$				Bjorken and Brodsky (1970)
Aplanarity	$A = (3/2)\lambda_3$	0	0	$\leq 1/2$	Bjorken and Brodsky (1970)
Planarity	$P = \lambda_2 - \lambda_3$				Bjorken and Brodsky (1970)
(Transverse) spherocity	$S_0 = (\pi^2/4)\min_{\hat{n}}(\sum_a \lvert\vec{p}_{a,T} \times \hat{n}\rvert / \sum_a \vec{p}_{a,T})^2$	0	0	≤ 1	Banfi, Salam, and Zanderighi (2010)
Thrust	$T = \max_{\hat{n}}(\sum_a \lvert\vec{p}_a \times \hat{n}\rvert / \sum_a \lvert\vec{p}_a\rvert)$	1	$\geq 2/3$	$\geq 1/2$	Brandt *et al.* (1964) and Farhi (1977)
Thrust major	$T_{\text{major}} = \max_{\hat{n}_{\text{major}} \perp \hat{n}_T}(\sum_a \lvert\vec{p}_a \cdot \hat{n}_{\text{major}}\rvert / \sum_a \lvert\vec{p}_a\rvert)$	0	$\leq 1/3$	$\leq 1/\sqrt{2}$	Brandt *et al.* (1964) and Farhi (1977)
Thrust minor	$T_{\text{minor}} = \sum_a \lvert\vec{p}_a \cdot \hat{n}_{\text{minor}}\rvert / \sum_a \lvert\vec{p}_a\rvert$ with $\hat{n}_{\text{minor}} = \hat{n}_T \times \hat{n}_{\text{major}}$	0	0	$\leq 1/2$	Brandt *et al.* (1964) and Farhi (1977)
Oblateness	$\mathcal{O} = T_{\text{major}} - T_{\text{minor}}$	0	$\leq 1/3$	0	
Normalized hemisphere mass	$M^2_{1(2)} = (1/E^2_{\text{CM}})(\sum_{a \in H_{1(2)}} p_a)^2$, with $H_{1(2)}$ hemispheres divided by the plane normal to $\hat{n}_T$				Banfi, Salam, and Zanderighi (2010)
Heavy jet mass	$M^2_H = \max(M^2_1, M^2_2)$	0	$\leq 1/3$	$\leq 1/2$	Banfi, Salam, and Zanderighi (2010)
Light jet mass	$M^2_L = \min(M^2_1, M^2_2)$				Banfi, Salam, and Zanderighi (2010)
Jet mass difference	$M^2_D = \lvert M^2_1 - M^2_2\rvert$	0	$\leq 1/3$	0	Banfi, Salam, and Zanderighi (2010)
Jet broadening	$B_{1(2)} = \sum_{a \in H_{1(2)}} \lvert\vec{p}_a \times \hat{n}_T\rvert / 2\sum_b \lvert\vec{p}_b\rvert^2$				Banfi, Salam, and Zanderighi (2010)
Wide or narrow, total broadening	$B_{W/N} = \max / \min(B_1, B_2)$, $B_T = B_W + B_N$				Banfi, Salam, and Zanderighi (2010)
Fox-Wolfram moments	$H_\ell = \sum_{i,j}(\lvert\vec{p}_i\rvert\lvert\vec{p}_j\rvert/E^2) P_\ell(\cos\theta_{ij})$				Fox and Wolfram (1979)
N jettiness	$\tau_N = (2/Q^2)\sum_k \min\{q_a \cdot p_k, q_b \cdot p_k, q_1 \cdot p_k, \ldots, q_N \cdot p_k\}$				Stewart, Tackmann, and Waalewijn (2010)
N subjettiness	$\tau_N = (1/\sum_k p_{T,k} R_0) \times \sum_k p_{T,k} \min\{\Delta R_{1k}, \Delta R_{2k}, \ldots, \Delta R_{Nk}\}$				Thaler and Tilburg (2011)
Energy-energy correlation	$\text{EEC}(\chi) = (1/\sigma) d\Sigma/d\cos\chi = \sum_{i,j} \int (E_i E_j / Q^2) \delta(\hat{p}_i \cdot \hat{p}_j - \cos\chi) d\sigma$				Basham *et al.* (1978) and Basham *et al.* (1979)

A common observable is the thrust, which is defined as

$$T = \max_{\vec{n}} \left(\frac{\sum_i |\vec{p}_i \cdot \vec{n}|}{\sum_i |\vec{p}_i|} \right). \tag{9}$$

In Eq. (9) the so-called thrust axis $\vec{n}_T$ is defined in terms of the unit vector $\vec{n}$ that maximizes T. This definition implies that for $T = 1$ the event is perfectly back to back, while for $T = 1/2$ the event is spherically symmetric. The unit vector that maximizes the thrust in the plane perpendicular to $\vec{n}_T$ is called the thrust major direction, and the vector perpendicular

to both the thrust and the thrust major is called the thrust minor direction. The thrust major and thrust minor variables are defined as

$$T_{\text{major}} = \max_{\vec{n}_{\text{major}} \perp \vec{n}_T} \left(\frac{\sum_i |\vec{p}_i \cdot \vec{n}_{\text{major}}|}{\sum_i |\vec{p}_i|} \right), \tag{10}$$

$$T_{\text{minor}} = \frac{\sum_i |\vec{p}_i \cdot \vec{n}_{\text{minor}}|}{\sum_i |\vec{p}_i|}, \tag{11}$$

where $\vec{n}_{\text{minor}} = \vec{n}_T \times \vec{n}_{\text{major}}$. The oblateness O is defined as the difference between the thrust major and thrust minor $O = T_{\text{major}} - T_{\text{minor}}$. Transverse thrust and its minor component are defined similarly but using transverse momenta ($\vec{p}_{T,i}$ instead of $\vec{p}_i$) of particles in the events.

The sphericity (S), transverse sphericity (S_T), aplanarity (A), and planarity (P) provide additional global information about the full momentum tensor M of the event via its eigenvalues,

$$M_{ij} = \frac{\sum_{a=1}^{n_j} p_{ia} p_{ja}}{\sum_{a=1}^{n_j} |\vec{p}_a|^2}, \tag{12}$$

where i and j are the spatial indices and the sum runs over all particles (or, in some applications, over the reconstructed jets). The ordered eigenvalues λ_i ($\lambda_1 > \lambda_2 > \lambda_3$) with the normalization condition $\sum_i \lambda_i = 1$ define the sphericity, transverse sphericity, aplanarity, and planarity as follows:

$$S = \tfrac{3}{2}(\lambda_2 + \lambda_3), \tag{13}$$

$$S_T = \frac{2\lambda_2}{\lambda_1 + \lambda_2}, \tag{14}$$

$$A = \tfrac{3}{2}\lambda_3, \tag{15}$$

$$P = \tfrac{2}{3}(S - 2A) = \lambda_2 - \lambda_3. \tag{16}$$

The sphericity axis is defined along the direction of the eigenvector of λ_1, and the semimajor axis is along the eigenvector for λ_2. The sphericity and transverse sphericity measure the total transverse momentum with respect to the sphericity axis defined by the four-momenta in the event. In other words, the sphericity of an event is a measure of how close in shape the spread of energy in the event is to a sphere. The allowed range for S is $0 \le S \le 1$. The transverse sphericity is defined by the two largest eigenvalues, and the allowed range is again $0 \le S_T < 1$. Aplanarity measures the amount of transverse momentum out of the plane formed by the two leading jets. The allowed range for A is $0 \le A < 1/2$. The planarity is a linear combination of the second and third eigenvalues of the quadratic momentum tensor. Note that owing to the quadratic dependence on the particle momenta the observables (13)–(16) are collinear unsafe and should be used with care (Dasgupta and Salam, 2004).

A plane through the origin whose normal vector is the thrust vector ($\vec{n}_T$) divides an event into two hemispheres H_1 and H_2. The corresponding normalized hemisphere invariant masses are defined as

$$M_i^2 = \frac{1}{E_{\text{CM}}^2} \left(\sum\nolimits_{a \in H_i} p_a \right)^2, \qquad i = 1, 2, \tag{17}$$

where p_a is the four-momentum of the ath jet. The larger of the two is called the heavy jet mass M_H and the smaller is called the light jet mass M_L,

$$M_H = \max(M_1^2, M_2^2), \tag{18}$$

$$M_L = \min(M_1^2, M_2^2). \tag{19}$$

The difference between the two is called the jet mass difference $M_D = M_H - M_L$.

A measure of the broadening of particles in the transverse momentum with respect to the thrust axis $\vec{n}_T$ is calculated as follows:

$$B_i = \frac{\sum_{a \in H_i} |\vec{p}_a \times \vec{n}_T|}{2 \sum_b |\vec{p}_b|^2}, \qquad i = 1, 2, \tag{20}$$

where b runs over all particles and a runs over particles in one of the two hemispheres. The larger of the two hemisphere broadenings is called the wide jet broadening [$B_W = \max(B_1, B_2)$], while the smaller is called the narrow jet broadening [$B_N = \min(B_1, B_2)$]. The total jet broadening is the sum of the two ($B_T = B_W + B_N$).

The C parameter

$$C = 3(\lambda_1\lambda_2 + \lambda_2\lambda_3 + \lambda_3\lambda_1) \tag{21}$$

is derived from the eigenvalues (λ_i) of the linearized momentum tensor Θ_{ij},

$$\Theta_{ij} = \frac{1}{\sum_a |\vec{p}_a|} \sum_b \frac{p_{ib} p_{jb}}{|\vec{p}_b|}, \qquad i, j = 1, 2, 3. \tag{22}$$

Many of these shapes variables are used to analyze data at both lepton colliders (Abdallah *et al.*, 2003; Ford, 2004) and hadron colliders (Weber, 2009, 2011; Banfi, 2010; Lenz, Spannowsky, and Tetlalmatzi-Xolocotzi, 2018; Aad *et al.*, 2021b).

The Fox-Wolfram moments (Fox and Wolfram, 1978, 1979) are defined as

$$H_\ell = \sum_{i,j} \frac{|\vec{p}_i||\vec{p}_j|}{E_{\text{total}}^2} P_\ell(\cos\theta_{ij}), \tag{23}$$

where θ_{ij} is the opening angle between energy clusters i and j, E_{total} is the total energy of the clusters (in the event center-of-mass frame), and $P_\ell(x)$ is the Legendre polynomial. For an event that has the structure of two back-to-back jets in the center-of-mass frame, $H_0 = 0$, $H_\ell \approx 1$ for even ℓ, and $H_\ell \approx 0$ for odd ℓ. Often the ratio between the Fox-Wolfram moments could be a useful discriminating variable against backgrounds; see Chen (2012), Englert, Spannowsky, and Takeuchi (2012), and Bernaciak *et al.* (2013) for applications of the Fox-Wolfram moments in Higgs physics and in jet substructure.

The transverse spherocity (Banfi, Salam, and Zanderighi, 2010) is defined as

$$S_\perp = \frac{\pi^2}{4}\min_{\vec{n}_T}\left(\frac{\sum_i |\vec{p}_{iT}\times\vec{n}_T|}{\sum_i p_{iT}}\right)^2, \tag{24}$$

where the minimization is performed over all possible unit transverse vectors $\vec{n}_T = (n_x, n_y, 0)$ [not to be confused with the thrust axis defined in Eq. (9)]. This variable ranges from 0 for pencil-like events to a maximum of 1 for circularly symmetric events.

The centrality

$$C = \frac{\sum |\vec{p}_{\mathrm{vis},i}|}{\sum E_{\mathrm{vis},i}} \tag{25}$$

is a measure of how much of the event is contained within the central part of the detector.

The energy-energy correlation (EEC) function (Basham *et al.*, 1978, 1979) is defined as

$$\mathrm{EEC}(\chi) = \frac{d\Sigma}{d\cos\chi} = \sum_{i,j}\int \frac{E_i E_j}{E^2_{\mathrm{total}}}\delta(\hat{p}_i\cdot\hat{p}_j - \cos\chi)d\Phi, \tag{26}$$

where i and j run over all of the final-state particles, which have the four-momenta $p_i^\mu = (E_i, \vec{p}_i)$ and $p_j^\mu = (E_j, \vec{p}_j)$, E_{total} is the total energy of the system in the center-of-mass frame, and $d\Phi$ is the phase-space measure (Dixon *et al.*, 2018). The unit vectors $\hat{p}_i$ and $\hat{p}_j$ point along the spatial components of p_i and p_j, respectively. EEC measures the differential angular distribution of particles that flow through two cells in the calorimeter separated by an angle $\chi \in (0, \pi)$ and is defined as an energy-weighted cross section corresponding to the process of interest.

Another example of a simple shape variable is y_{23}, a measure of the third jet p_T relative to the sum of the transverse momenta of the two leading jets in a multijet event, which is defined as (Akrawy *et al.*, 1990; Catani *et al.*, 1991)

$$y_{23} = \frac{p^2_{T,j_3}}{(p_{T,j_1} + p_{T,j_2})^2}, \tag{27}$$

where p_{T,j_1}, p_{T,j_2}, and p_{T,j_3} represent the leading, subleading, and third-leading jets in the event, respectively. The allowed range for y_{23} is $0 \le y_{23} < 1/4$.

There are many other event shape variables that are not discussed in this review. See Moult, Necib, and Thaler (2016) for insight into the energy correlation functions, Stewart, Tackmann, and Waalewijn (2010) and Thaler and Tilburg (2011) for N jettiness, Cesarotti, Reece, and Strassler (2021) and Cesarotti and Thaler (2020) for event isotropy using the energy mover's distance (EMD), and Banfi, Salam, and Zanderighi (2010) for other interesting event shape variables.

B. Missing momentum

Missing energy (missing momentum) refers to the amount of energy (momentum) that is not measured or detected in a particle detector but that can be inferred from the laws of energy-momentum conservation. In hadron colliders, the initial momenta of the colliding partons along the beam axis are unknown, so the missing energy and the missing total momentum cannot be determined. However, the total momentum of initial particles in the plane orthogonal to the beam is zero, and any net visible momentum in the transverse direction is therefore indicative of missing transverse momentum ($\vec{\not{p}}_T$).

Missing transverse momentum arises whenever the final state includes particles that do not interact with the electromagnetic or strong forces, and therefore escape the detector. A typical example in the SM is neutrino production. Notably, dark-matter candidates in BSM models are also invisible in the detector, making the $\vec{\not{p}}_T$ signature a smoking gun for the existence of nongravitationally interacting dark matter. Therefore, an extensive range of dark-matter searches has been performed in collider experiments, centered around the missing transverse momentum signature: for example, $\vec{\not{p}}_T$ plus monojet (Aaboud *et al.*, 2018h; Sirunyan *et al.*, 2017c), monophoton (Aaboud *et al.*, 2017c; Sirunyan *et al.*, 2017d), mono–Z/W (Aaboud *et al.*, 2018a, 2018b; Sirunyan *et al.*, 2017b, 2017c, 2021a), and mono-Higgs signatures (Aaboud *et al.*, 2017d, 2017e; Sirunyan *et al.*, 2020c).

The missing transverse momentum $\vec{\not{p}}_T$ of the hard scattering interaction is defined as the negative vectorial sum of the transverse momenta of the set of reconstructed objects including hard and soft objects (Chatrchyan *et al.*, 2011a; Aaboud *et al.*, 2018g),

$$\vec{\not{p}}_T = -\sum_{i\in\text{hard objects}} \vec{p}_{T,i} - \sum_{j\in\text{soft objects}} \vec{p}_{T,j}, \tag{28}$$

whose magnitude and angle on the transverse plane are defined, respectively, as

$$\not{E}_T = E_T^{\mathrm{miss}} = \not{p}_T = \sqrt{\not{p}^2_{Tx} + \not{p}^2_{Ty}}, \tag{29}$$

$$\varphi = \tan^{-1}\left(\frac{\not{p}_{Ty}}{\not{p}_{Tx}}\right). \tag{30}$$

As indicated in Eq. (29), it has become customary to refer to the magnitude of the missing transverse momentum as the missing transverse energy. Here the hard objects consist of selected $e^\pm$, $\mu^\pm$, and accepted γ, $\tau^\pm$, and jets, while the soft objects are not associated with any of the aforementioned hard objects but identified as the unused tracks from the primary vertex (Aaboud *et al.*, 2018g). To reduce the effect of pileup, ATLAS (Aaboud *et al.*, 2018g) required these tracks to have $p_T > 0.4$ GeV, $|\eta| < 2.5$, and a transverse (longitudinal) impact parameter $|d_0| < 1.5$ mm ($|z_0 \sin\theta| < 1.5$ mm).

The scalar sum of all transverse visible momenta is defined as

$$H_T = \sum_{i\in\text{hard objects}} p_{T,i} + \sum_{j\in\text{soft objects}} p_{T,j}. \tag{31}$$

The quantities defined in Eqs. (28)–(31) are often used to estimate the hardness of the hard scattering event in the transverse plane, and thus provide a measure for the event activity in physics analyses.

C. Variables sensitive to the overall energy scale

In the case of fully visible final states, the total invariant mass in the event provides an estimate of the energy scale $\sqrt{\hat{s}}$ of the hard scattering, where $\hat{s}$ is the parton-level Mandelstam variable. However, if the final state includes invisible particles as in Fig. 4, the task becomes more challenging, which has led to the introduction of several inclusive variables for this purpose.

One class of such variables was originally explored in the context of supersymmetry, where strong production of gluinos and/or squarks results in a multijet plus $\not{E}_T$ signature. Several versions of an "effective scale" variable $M_{\rm eff}$ for that case have been used in the literature (Hinchliffe *et al.*, 1997; Tovey, 2001); they are closely related to Eq. (31) and differ by (i) the number of jets N_j included in the sum. Typical choices for N_j are either 4 or "all" and (ii) whether or not the value of the $\not{E}_T$ is added as well,

$$M_{\rm eff}(N_j, I) = \sum_i^{N_j} p_{T,i} + I * \not{E}_T, \tag{32}$$

where $I \in \{0, 1\}$ parametrizes the binary choice between including $\not{E}_T$ or omitting it. The main advantage of the effective mass variable (32), which led to its widespread usage in the LHC community, is its simplicity. However, it also has drawbacks; for example, it misses the potential dependence on the masses of any invisible particles. Being empirically derived, it is not on a firm theoretical footing, which explains the large number of different $M_{\rm eff}$ variants in use [with H_T from Eq. (31) one such example].

An alternative approach that Konar, Kong, and Matchev (2009) advocated for was to enforce the missing energy constraint in Eq. (28) and then utilize a minimum energy principle to fix the momenta of the invisible particles, thus arriving at a more precise estimate of $\sqrt{\hat{s}}$,

$$\sqrt{\hat{s}}_{\rm min}(M_{\rm inv}) = \sqrt{E^2 - P_z^2} + \sqrt{\not{E}_T^2 + M_{\rm inv}^2}, \tag{33}$$

where E and P_z are the total visible energy and the total longitudinal visible momentum in the event, respectively. In Eq. (33) we encounter our first example of a kinematic variable that depends on a hypothesized mass parameter, namely, $M_{\rm inv}$, which is the total mass of all invisible particles in the event. By construction, $\sqrt{\hat{s}}_{\rm min}$ is the minimum possible center-of-mass energy (for a given value of $M_{\rm inv}$) that is consistent with the measured values of the total energy E and the total visible momentum $\vec{P}$, and thus has a well-defined physical meaning. However, when applied to the full event, $\sqrt{\hat{s}}_{\rm min}$ receives large contributions from QCD initial-state radiation in the forward direction that disrupt the connection to the underlying new-physics parameters (Papaefstathiou and Webber, 2009). This led to "subsystem" variants of $\sqrt{\hat{s}}_{\rm min}$ where one can focus on a set of reconstructed objects within the central region, with a measured total energy $E_{\rm (sub)} < E$ and a total longitudinal momentum $P_{z\rm (sub)}$, away from the dangers of the forward QCD radiation (Konar *et al.*, 2011; Robens, 2012),

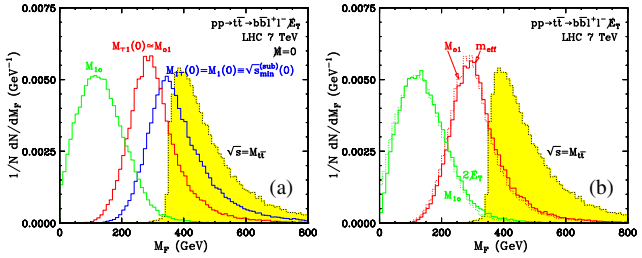

FIG. 5. Unit-normalized distributions of various inclusive event variables ($\not{E}_T$, $M_{\rm eff}$, H_T, M_1, and $\sqrt{\hat{s}}_{\rm min}$) for top quark pair production ($pp \to t\bar{t} \to b\bar{b}\ell^+\ell^-\nu\bar{\nu}$). Unlike the variables plotted in the right panel, those in the left panel require an ansatz for the invisible mass parameter $M_{\rm inv}$, which was taken to be zero. The yellow-shaded histogram shows the true $\sqrt{\hat{s}}$ distribution in the sample. From Barr, Khoo *et al.*, 2011.

$$\sqrt{\hat{s}}^{\rm (sub)}_{\rm min}(M_{\rm inv}) = \left\{ \left(\sqrt{E^2_{\rm (sub)} - P^2_{z\rm (sub)}} + \sqrt{\not{E}_T^2 + M^2_{\rm inv}} \right)^2 - \vec{u}_T^{\,2} \right\}^{1/2}, \tag{34}$$

where $\vec{u}_T = \vec{P}_T - \vec{P}_{T\rm (sub)}$ is the upstream transverse momentum due to QCD radiation and/or visible particle decays outside the subsystem; see Fig. 3. The $s_{\rm min}$ variables have been further extended to include additional constraints during minimization (Swain and Konar, 2015), and such constrained $s_{\rm min}$ variables have been applied to physics processes like $h \to \tau\tau$ (Konar and Swain, 2016b; Bhardwaj *et al.*, 2019). A sample assortment of inclusive event variables is shown in Fig. 5 for the case of dilepton top quark pair production ($pp \to t\bar{t} \to \ell^+\ell^-\nu\bar{\nu}$) (Barr, Khoo *et al.*, 2011). Note that among the different variable choices in Fig. 5, the $\sqrt{\hat{s}}^{\rm (sub)}_{\rm min}$ distribution is the one that peaks closest to the production mass threshold $2m_t$.

V. EXCLUSIVE EVENT VARIABLES: INVARIANT MASS

In Secs. V–VII we discuss kinematic variables that can be constructed and evaluated by processing information restricted to or associated with a particular set of final-state visible particles in an event by a suitable partitioning, as illustrated in Fig. 3. This section is devoted to invariant mass variables, which can be reconstructed from collections of visible particles only (Sec. V.A) or from semi-invisible collections of particles (Sec. V.B).

Mass variables have played a major role not only for measuring the masses of new particles but for discovering new physics in resonance-type searches. Techniques utilizing mass variables received a major boost in the LHC era and have been actively and extensively investigated for LHC phenomenology. Examples range from traditional $(1+3)$-dimensional invariant masses and $(1+2)$-dimensional transverse masses to the "stransverse" mass [also known as the Cambridge M_{T2} variable (Lester and Summers, 1999)] to its variations M_2 (Cho, Gainer *et al.*, 2014), the razor (Rogan, 2010), Δ_4 (Byers and Yang, 1964), etc. In the following we discuss the main

ideas and mathematical understanding of these variables, their collider implications, and typical applications.

A. Mass variables of collections of visible particles

In this subsection we review mass variables[4] that do not make use of the measured $\not{E}_T$. The standard example is the invariant mass $M_{\rm vis}$ of a set of visible particles

$$M_{\rm vis}^2 = \left(\sum\nolimits_i p_i\right)^2 = \left(\sum\nolimits_i E_i\right)^2 - \left(\sum\nolimits_i \vec{p}_i\right)^2, \tag{35}$$

where i runs over the visible particles of interest. Since it is a Lorentz-invariant quantity by definition, its physical implications can be understood consistently irrespective of the frame in which one performs measurements or analyses. This is why Eq. (35) is routinely used in a wide range of high-energy experiments, including accelerator-based ones.

The simplest application (but a sufficiently nontrivial one) is a heavy resonance A_1 decaying to a pair of visible particles a_1 and a_0, i.e., $A_1 \to a_1 a_0$. The energy-momentum conservation $p_{A_1} = p_{a_1} + p_{a_0}$ implies that the resonance mass can be reconstructed from the four-momenta of the visible decay products,

$$M_{A_1}^2 = p_{A_1}^2 = (E_{a_1} + E_{a_0})^2 - (\vec{p}_{a_1} + \vec{p}_{a_0})^2. \tag{36}$$

Mathematically, the distribution of M_{A_1} is a δ function located at the true mass m_{A_1} of A_1. However, the virtuality of the unstable A_1 forces events to spread and populate the region around m_{A_1} according to the Breit-Wigner distribution in M_{A_1} as follows:

$$\frac{dN}{dM_{A_1}} \propto \frac{1}{(M_{A_1}^2 - m_{A_1}^2)^2 + m_{A_1}^2 \Gamma_{A_1}^2}, \tag{37}$$

where Γ_{A_1} is identified as the decay width of A_1. As a consequence, the M_{A_1} distribution allows for a simultaneous determination of m_{A_1} and Γ_{A_1}. Since most events lie within a few Γ_{A_1} from m_{A_1}, by restricting to a narrow invariant mass window around m_{A_1}, one can efficiently isolate the resonance events from unwanted background events. Owing to its considerable background-rejection capability, the invariant mass variable (35) has played a crucial role in the discovery of many particles, including the Z gauge boson (Arnison *et al.*, 1983b; Bagnaia *et al.*, 1983), hadrons such as J/ψ (Aubert *et al.*, 1974; Augustin *et al.*, 1974) and Υ (Herb *et al.*, 1977), and the SM Higgs boson (Aad *et al.*, 2012b; Chatrchyan *et al.*, 2012) (left panel of Fig. 6).

Once some of the decay products are invisible in the detector, the resonance feature is no longer available. Nevertheless, the invariant mass of the remaining visible decay products still provides useful information about the underlying dynamics, and its features have been thoroughly

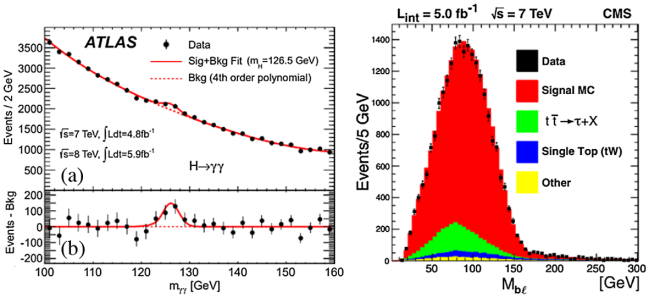

FIG. 6. Left panel: diphoton invariant mass distribution of $h \to \gamma\gamma$ events. From Aad *et al.*, 2012b. Right panel: $M_{b\ell}$ invariant mass distribution of the leptonic top quark decay events. From Chatrchyan *et al.*, 2013a.

investigated. To have a nontrivial invariant mass variable, at least two visible final-state particles are required in addition to the invisible particle(s). A well-known example is the leptonic decay of a top quark, i.e., $t \to bW, W \to \ell\nu_\ell$, giving rise to the invariant mass $M_{b\ell}$ (right panel of Fig. 6) formed by the bottom quark and the lepton

$$M_{b\ell} = (p_b + p_\ell)^2. \tag{38}$$

When it comes to BSM models, there are many such processes in connection with dark-matter candidates, for example, the decay of a heavier neutralino to a pair of leptons and the lightest neutralino (an invisible dark-matter candidate) via a supersymmetric lepton intermediary state.

We now work out the generic two-step, two-body cascade decay case $A_2 \to a_2 A_1, A_1 \to a_1 a_0$ and assume that a_2 and a_1 are visible and massless, while a_0 is invisible; see Fig. 7(a)]. For simplicity, we further assume that all particles are spinless or produced in an unpolarized fashion and focus on decay kinematics purely governed by phase space. Since a_1 and a_2 were assumed to be massless, the invariant mass squared $M_{a_2 a_1}^2$ is simply given by

$$M_{a_2 a_1}^2 = 2E_{a_2}E_{a_1}(1 - \cos\theta_{a_2 a_1}), \tag{39}$$

where $\theta_{a_2 a_1}$ is the angle between $\vec{p}_{a_2}$ and $\vec{p}_{a_1}$.

Using Lorentz invariance, one can evaluate this quantity in a convenient frame. In the A_1 rest frame, the energies $E_{a_2}^*$ and $E_{a_1}^*$ of a_2 and a_1 are given by

$$E_{a_2}^* = \frac{m_{A_2}^2 - m_{A_1}^2}{2m_{A_1}}, \tag{40}$$

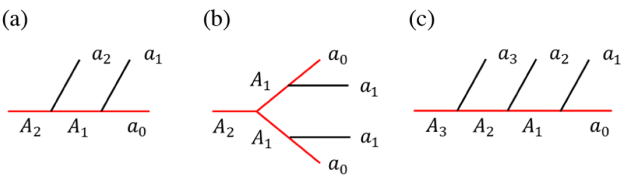

FIG. 7. (a) Two-step, two-body cascade decay topology. (b) Antler decay topology. (c) Three-step, two-body cascade decay topology.

[4]Remember that in our convention the masses of individual particles are denoted with a lowercase m, while any mass of a collection of particles is denoted with a capital M; see Sec. III.A.

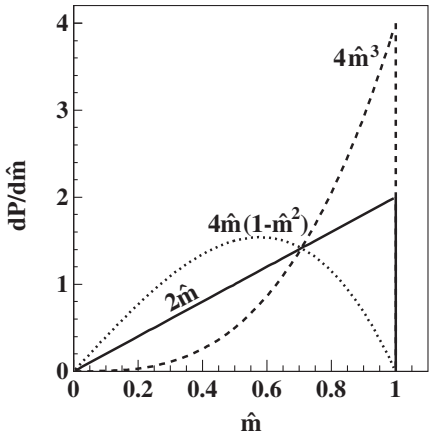

FIG. 8. Unit-normalized distribution of the rescaled invariant mass $\hat{m} = M_{a_2a_1}/M^{\max}_{a_2a_1}$ for the two-step, two-body decay topology in Fig. 7(a). The solid line shows the pure phase-space distribution from Eq. (42), while the dotted (dashed) line corresponds to the left-handed (right-handed) chiral coupling. From Barr, 2004.

$$E^*_{a_1} = \frac{m^2_{A_1} - m^2_{a_0}}{2m_{A_1}}. \tag{41}$$

Note that in this frame the pure phase-space distribution of $\cos\theta^*_{a_2a_1}$ becomes flat. Using Eqs. (39)–(41), we can derive the unit-normalized distribution of $M_{a_2a_1}$, $(1/\Gamma)d\Gamma/dM_{a_2a_1}$, as follows:

$$\begin{aligned}\frac{1}{\Gamma}\frac{d\Gamma}{dM_{a_2a_1}} &= \frac{M_{a_2a_1}}{2E^*_{a_2}E^*_{a_1}}\Theta(M^{\max}_{a_2a_1} - M_{a_2a_1}) \\ &= \frac{2M_{a_2a_1}}{(M^{\max}_{a_2a_1})^2}\Theta(M^{\max}_{a_2a_1} - M_{a_2a_1}),\end{aligned} \tag{42}$$

where $M^{\max}_{a_2a_1}$ denotes the maximum value of $M_{a_2a_1}$ arising at $\cos\theta^*_{a_2a_1} = -1$, i.e., when a_2 and a_1 move in a back-to-back direction. It is a function of the three input mass parameters

$$(M^{\max}_{a_2a_1})^2 = m^2_{A_2}(1 - R_{12})(1 - R_{01}), \tag{43}$$

where we introduce a mass ratio symbol for purposes of later convenience,[5]

$$R_{ij} \equiv m^2_{A_i}/m^2_{A_j}. \tag{44}$$

As suggested by Eq. (42) and illustrated in Fig. 8, the $M_{a_2a_1}$ distribution increases linearly and sharply falls off at the kinematic end point defined in Eq. (43). Therefore, the $M_{a_2a_1}$ invariant mass variable can be used as a kinematic cut to define the signal-rich region, and the measurement of the kinematic end point provides a relation among the three underlying mass parameters. Numerous experimental and phenomenological studies have adopted this variable for various physics applications. Examples include the top quark mass measurement (CMS Collaboration, 2014), as well as new particle searches and mass determinations in the context of supersymmetry, extra dimensions, and other BSM exotica. A more generic discussion for the mass measurement aspects of kinematic end points is given in Sec. VIII.C.

The shape described in Eq. (42) is valid as far as A_1 is either scalar or unpolarized and is produced on mass shell with a negligible particle width. A nontrivial matrix element reshuffles and reweighs the relevant phase-space density, resulting in a shape distortion while keeping the end point unchanged. Indeed, many new-physics models conceive the same experimental signatures, potentially along with the same decay topology (Cheng, Matchev, and Schmaltz, 2002a). It has been realized that shape analysis can be an important tool for understanding the underlying dynamics (Barr, 2004; Datta, Kong, and Matchev, 2005; Smillie and Webber, 2005; Alves, Eboli, and Plehn, 2006; Athanasiou *et al.*, 2006; Wang and Yavin, 2007; Burns *et al.*, 2008). For example, the dotted and dashed lines in Fig. 8 illustrate the distortion of the invariant mass spectrum due to left-handed and right-handed chiral couplings, respectively.

Different spin correlations between the visible particles may also result from different spin assignments of A_2, A_1, and a_0, giving rise to different shapes of the $M_{a_2a_1}$ distributions. For example, supersymmetric models and extradimensional models often give rise to an identical set of final-state visible particles under the same event topology; the shape analysis allows the underlying scenarios to be discriminated (Barr, 2004; Datta, Kong, and Matchev, 2005; Smillie and Webber, 2005; Alves, Eboli, and Plehn, 2006; Athanasiou *et al.*, 2006; Csaki, Heinonen, and Perelstein, 2007; Kilic, Wang, and Yavin, 2007; Wang and Yavin, 2007; Burns *et al.*, 2008). A departure from Eq. (42) may arise even in the absence of nontrivial spin correlations. It has been demonstrated that the non-negligible particle width of the intermediary particle A_1 encoded in its propagator can affect the shape, resulting in the extension of the $M_{a_2a_1}$ distribution beyond its nominal end point in Eq. (43) (Grossman, Martone, and Robinson, 2011). Study of this sort has been generalized in a more systematic manner to the case where not only A_1 but also A_2 and a_0 have non-negligible particle widths (Kim and Matchev, 2018). The distributions again extend beyond the nominal end points. Depending on the underlying mass spectrum, this end point "violation" effect can be appreciable for Γ/m as low as 1%, even in the presence of detector smearing (Kim and Matchev, 2018). In particular, this effect allows one to test the nature of the invisible a_0, which is typically assumed to be a stable dark-matter candidate. However, it is also possible that it has a nonzero width due to its invisible decays to lighter dark-sector states. Therefore, this kind of shape analysis could discriminate between a true dark-matter candidate and an unstable (invisibly decaying) dark-sector state (Kim and Matchev, 2018).

The shape in Eq. (42) may differ from the expectation if the underlying physics does not obey the assumed two-step, two-body cascade decay topology. For example, the intermediary state A_1 could be highly off shell, more invisible particles could be involved in the process in addition to a_0, or A_2 may decay to a pair of A_1's, each of which decays to a_0 and a_1 [i.e., the so-called antler topology (Han, Kim, and Song, 2010; Edelhauser,

[5]Note that $R_{01} \equiv m^2_{a_0}/m^2_{A_1}$.

Matchev, and Park, 2012; Han, Kim, and Song, 2013) $A_2 \to A_1 A_1 \to a_1 a_0 a_1 a_0$ depicted in Fig. 7(b)]. The $M_{a_1 a_1}$ distribution resulting from the antler event topology is given by

$$\frac{1}{\Gamma}\frac{d\Gamma}{dM_{a_1a_1}} \propto \begin{cases} 2\eta M_{a_1a_1}, & 0 < M_{a_1a_1}/M^{\max}_{a_1a_1} < e^{-2\eta}, \\ M_{a_1a_1}\ln(M^{\max}_{a_1a_1}/M_{a_1a_1}), & e^{-2\eta} < M_{a_1a_1}/M^{\max}_{a_1a_1} < 1, \end{cases} \tag{45}$$

where $\cosh\eta = \sqrt{R_{12}}/2$ and the end point $M^{\max}_{a_1a_1}$ is given by

$$(M^{\max}_{a_1a_1})^2 = m^2_{A_1} e^{2\eta}(1-R_{01})^2. \tag{46}$$

It is noteworthy that the distribution shows a derivative discontinuity, i.e., cusp, at $M_{a_1a_1} = e^{-2\eta} M^{\max}_{a_1a_1}$ (Han, Kim, and Song, 2010). This is a kinematic feature unaffected by the underlying dynamics; the cusp feature remains intact in the presence of nontrivial spin correlations (Edelhauser, Matchev, and Park, 2012).

In general different event topologies resulting in only two visible particles a_1 and a_2 give different $M_{a_2a_1}$ distributions, and the phase-space shape information allows one to determine the underlying physics without any prior assumptions on the process or its detailed dynamics (Cho, Kim *et al.*, 2014). The left panel of Fig. 9 displays nine possible event topologies for the decay of resonance A into two visible particles (here v_1 and v_2) and up to two invisible particles (here χ_1 and χ_2). It was demonstrated that these differing decay scenarios occupy different regions in the space of appropriately chosen kinematic variables (Cho, Kim *et al.*, 2014):

$$\frac{P}{E} = \frac{M^{\text{peak}}_{a_2a_1}}{M^{\max}_{a_2a_1}}, \tag{47}$$

$$R_2 = -\left[\frac{M^2_{a_2a_1}}{f(M^2_{a_2a_1})}\frac{d^2 f(M^2_{a_2a_1})}{dM^2_{a_2a_1}}\right]_{M_{a_2a_1}=M^{\text{peak}}_{a_2a_1}}. \tag{48}$$

In Eq. (48) $f(M_{a_2a_1})$ describes the shape of the $M_{a_2a_1}$ distribution whose peak position is identified at $M_{a_2a_1} = M^{\text{peak}}_{a_2a_1}$. The right panel of Fig. 9 depicts the regions spanned by the nine decay topologies in the $(P/E, (2/\pi)\tan^{-1}R_2)$ plane (Cho, Kim *et al.*, 2014). It was further shown that the topology identification using this strategy can be done with statistics as small as a few hundred signal events, depending on the

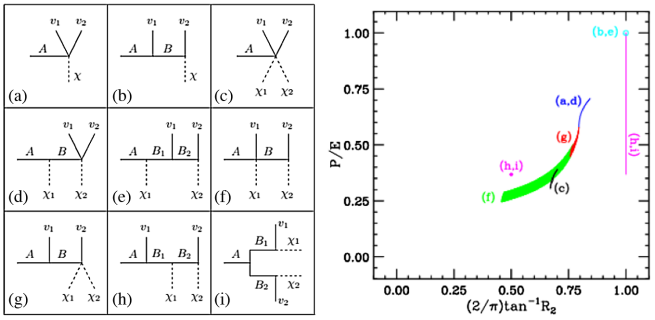

FIG. 9. Left panel: the nine event topologies considered for the decay of a heavy resonance A into two visible particles and up to two invisible particles. Right panel: the disambiguation of the nine decay topologies in the $(P/E, (2/\pi)\tan^{-1}R_2)$ space. From Cho, Kim *et al.*, 2014.

underlying model details. As an application of such topology disambiguation, one can infer the number of invisible or dark-matter particles from the shape analysis and determine whether or not the associated dark-matter stabilization symmetry is a Z_2 parity (Agashe *et al.*, 2010). As another application, it has been demonstrated that these various $M_{a_2a_1}$ distributions can mimic resonance-induced distributions with a broad width, especially at earlier stages of experiments, in the context of the 750 GeV diphoton excess (Cho, Kim *et al.*, 2016).

These considerations have been extended to other event topologies, resulting in a larger number of visible particles, such as three-step cascade decays (Allanach *et al.*, 2000; Lester, 2001; Gjelsten, Miller, and Osland, 2004, 2005b; Miller, Osland, and Raklev, 2006; Burns, Matchev, and Park, 2009; Costanzo and Tovey, 2009; Matchev *et al.*, 2009; Agashe *et al.*, 2010; Kim, Matchev, and Park, 2016; Matchev, Moortgat, and Pape, 2019) and $\geq$ 3-body invariant mass variables (Gjelsten, Miller, and Osland, 2005b; Alves, Eboli, and Plehn, 2006; Bisset, Lu, and Kersting, 2011; Kim, Matchev, and Park, 2016). We now illustrate the three-step, two-body cascade decay case $A_3 \to a_3 A_2$, $A_2 \to a_2 A_1$, and $A_1 \to a_1 a_0$ and again assume that a_3, a_2, and a_1 are visible and massless, while a_0 is invisible and potentially massive; see Fig. 7(c). The shapes and end points of the $M_{a_3a_2}$ and $M_{a_2a_1}$ invariant mass distributions follow Eqs. (42) and (43), with mass parameters appropriately replaced. The unit-normalized $M_{a_3a_1}$ distribution is (Miller, Osland, and Raklev, 2006)

$$\frac{1}{\Gamma}\frac{d\Gamma}{dM_{a_3a_1}} = \begin{cases} 2M_{a_3a_1}\ln R_{21}/(M^{\max}_{a_3a_1})^2(1-R_{12}), & 0 < M_{a_3a_1}/M^{\max}_{a_3a_1} < \sqrt{R_{12}}, \\ [2M_{a_3a_1}\ln(M^{\max}_{a_3a_1})^2/M^2_{a_3a_1}]/(M^{\max}_{a_3a_1})^2(1-R_{12}), & \sqrt{R_{12}} < M^2_{a_3a_1}/M^{\max}_{a_3a_1} < 1, \end{cases} \tag{49}$$

where the end point $M^{\max}_{a_3a_1}$ is given by

$$(M^{\max}_{a_3a_1})^2 = m^2_{A_3}(1-R_{23})(1-R_{01}). \tag{50}$$

Note that the distribution again features a cusp at $M_{a_3a_1} = M^{\max}_{a_3a_1}\sqrt{R_{12}}$, as in the antler topology. The existence of the cuspy structure can be utilized in a model-independent fashion to distinguish Z_3-stabilized dark-matter models from Z_2-stabilized dark-matter models (Agashe *et al.*, 2010), as it is unaffected by the underlying model details.

As discussed in Sec. II.B, it is often difficult to uniquely identify a_1, a_2, and a_3 on an event-per-event basis. For example, light quarks and gluons are never observed as isolated objects, but instead as a clustering of hadronic

objects, and it is difficult to tell them apart on an individual case basis. For charged leptons, their electric charges are identified, but the order of appearance is ambiguous unless they come from the decay of long-lived particles and their emission vertices along the decay path are measurable. Therefore, the two-body invariant mass variables in the process accompanying ≥ 3 visible particles are generally plagued by this combinatorial ambiguity.

The classic example from supersymmetry, which is often referred to as the $q\ell\ell$ chain, is the decay of a supersymmetric quark $\tilde{q}$ to a quark, an opposite-sign lepton pair, and a lightest neutralino $\tilde{\chi}_1^0$ through two intermediary states: a heavier neutralino $\tilde{\chi}_2^0$ and a supersymmetric lepton $\tilde{\ell}$, i.e., $\tilde{q} \to q\tilde{\chi}_2^0, \tilde{\chi}_2^0 \to \ell_n^{\pm}\tilde{\ell}^{\mp}, \tilde{\ell}^{\mp} \to \ell_f^{\mp}\tilde{\chi}_1^0$. Here $\ell_{n(f)}$ denotes the final-state lepton closer to (farther from) the quark. Owing to the combinatorial ambiguity associated with the leptons, $M_{q\ell_n}$ and $M_{q\ell_f}$ are not experimentally measurable quantities. One possible trial would be to put them together in a single combined distribution $M_{q\ell} \equiv M_{q\ell_n} \cup M_{q\ell_f}$ (Matchev *et al.*, 2009). The larger end point, i.e., $\max(M_{q\ell_n}^{\max}, M_{q\ell_f}^{\max})$, is measurable, whereas the smaller one may be buried in the middle of the $M_{q\ell}$ distribution. Nevertheless, this approach may be advantageous in the sense that the associated mass inversion formulas have a twofold rather than threefold ambiguity (Matchev *et al.*, 2009). On the other hand, the two ordered invariant masses $M_{q\ell}^{>} \equiv \max(M_{q\ell_n}, M_{q\ell_f})$ and $M_{q\ell}^{<} \equiv \min(M_{q\ell_n}, M_{q\ell_f})$ are experimentally measurable, and their respective end points can provide either of two independent mass relations depending on the underlying particle mass hierarchy. These ordered invariant masses have been extensively studied in the context of the supersymmetric $q\ell\ell$ chain (Allanach *et al.*, 2000; Lester, 2001; Gjelsten, Miller, and Osland, 2004, 2005b; Miller, Osland, and Raklev, 2006; Burns, Matchev, and Park, 2009; Matchev *et al.*, 2009), and in a seesaw scenario (Dev, Kim, and Mohapatra, 2016).

The idea of ordering the invariant masses was later generalized to the case where all visible particles in the final state are completely indistinguishable (Kim, Matchev, and Park, 2016). For a chosen fixed number of final-state particles sampled from the final state, all possible invariant mass combinations are formed and then ranked, and the corresponding distributions are then inspected for the appearance of any upper kinematic end points. This systematic approach allows particular phase-space configurations to be accessed through the respective kinematic end points and thus obtain independent mass relations that would be unavailable with the standard unranked invariant mass combinations.

B. Mass variables of semi-invisible collections of particles

In this section we discuss invariant mass-type variables whose definition takes advantage of the knowledge of the missing transverse momentum $\vec{p}_T$ in the event. They usually target parent particles, whose decay products may include invisible particles.

1. One invisible daughter particle

The first kinematic variable that we introduce is the transverse mass M_T, which applies to the case of a parent particle of mass m_P that decays to one visible and one invisible particle. An important physics example is the case of $W \to \ell\nu$ discussed in Appendix B.1. More complicated examples with several visible particles are given in Figs. 7(a) and 7(c). We notate the momentum of the visible daughter as $p^\mu = (E_{\rm vis}, \vec{p}_{{\rm vis},T}, p_{{\rm vis},z})$ and the momentum of the invisible daughter as $q^\mu = (E_{\rm inv}, \vec{p}_{{\rm inv},T}, q_{{\rm inv},z})$. The momentum of the decaying parent particle is therefore $p^\mu + q^\mu$, and the reconstructed parent invariant mass M_P is

$$M_P^2 = (p+q)^2 = m_{\rm vis}^2 + m_{\rm inv}^2 + 2[E_{{\rm vis},T}E_{{\rm inv},T}\cosh(\Delta\eta) - \vec{p}_{{\rm vis},T}\cdot\vec{q}_{{\rm inv},T}], \tag{51}$$

where the invariant mass $m_{\rm vis}$ of the visible sector is defined as $m_{\rm vis}^2 = p_\mu p^\mu$, the mass $m_{\rm inv}$ of the invisible daughter is given by $m_{\rm inv}^2 = q_\mu q^\mu$, and $\Delta\eta = \eta_{\rm vis} - \eta_{\rm inv}$ is the pseudorapidity difference between p^μ and q^μ. The corresponding transverse energies are given by

$$E_{{\rm vis},T} = \sqrt{m_{\rm vis}^2 + \vec{p}_{{\rm vis},T}^{\,2}}, \tag{52}$$

$$E_{{\rm inv},T} = \sqrt{m_{\rm inv}^2 + \vec{p}_{{\rm inv},T}^{\,2}}. \tag{53}$$

If both p^μ and q^μ were observable, a particle of mass m_P would appear as a resonance peak at $M_P = m_P$ in the invariant mass distribution dN/dM_P; see Eq. (37). However, if the daughter particle with momentum q escapes the detector, one can only infer $\vec{q}_{{\rm inv},T}$ from the momentum conservation on the transverse plane as

$$\vec{q}_{{\rm inv},T} = \vec{p}_T. \tag{54}$$

The longitudinal component $q_{{\rm inv},z}$ remains unknown and most of the discussion in the literature on kinematic variables has centered around the question as to how to deal with such missing information not just in this simple example, but in more general cases as well (Barr and Lester, 2010; Barr, Khoo *et al.*, 2011).

One general approach is to obtain a variable which provides an eventwise lower bound on the parent mass m_P (Barr, Khoo *et al.*, 2011). For this purpose, one considers all possible values of the unknown invisible momentum components (in this simple case $q_{{\rm inv},z}$) and picks the smallest resulting value of the reconstructed parent mass [Eq. (51)]. By minimizing Eq. (51) over $q_{{\rm inv},z}$ [or simply by noticing that $\cosh(\Delta\eta) \geq 1$], one obtains the so-called transverse mass

$$M_{TP}^2(\vec{q}_{{\rm inv},T}, m_{\rm inv}) = m_{\rm vis}^2 + m_{\rm inv}^2 + 2(E_{{\rm vis},T}E_{{\rm inv},T} - \vec{p}_{{\rm vis},T}\cdot\vec{q}_{{\rm inv},T}), \tag{55}$$

where $\vec{q}_{{\rm inv},T}$ is given by Eq. (54). By construction (since the minimization over $q_{{\rm inv},z}$ would inevitably include its true value in the event), the transverse mass satisfies the inequality

$$M_{TP} \leq m_P. \tag{56}$$

The equality (56) holds for events with $\Delta\eta = 0$. The most well-known example for the use of the transverse mass is the

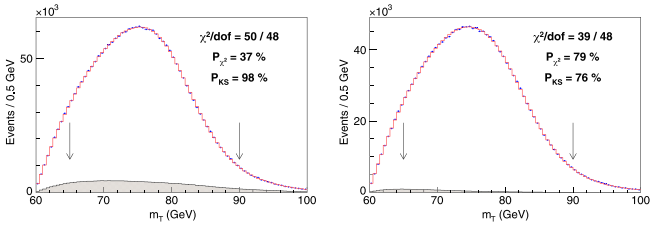

FIG. 10. Distribution of M_T for W boson to $\mu\nu_\mu$ (left panel) and $e\nu_e$ (right panel) final states for $m_{\rm inv} = 0$. Simulation and data points are shown as histogram and data points, respectively. From Aaltonen *et al.*, 2022.

discovery of the W boson (Arnison *et al.*, 1983a; Banner *et al.*, 1983). A recent measurement of the W mass done by the CDF Collaboration (see Fig. 10), which shows some tension with the SM and with previous measurements, was also based on the transverse mass (Aaltonen *et al.*, 2022) since M_{TP} is less sensitive to the modeling of the $W - p_T$ spectrum. The distributions in Fig. 10 exhibit an upper kinematic end point that, however, is smeared beyond the naive theoretical prediction [Eq. (56)] due to the finite W width and the detector resolution. We note that such a use of the transverse mass relies on the assumption that there is only one missing particle in each event, so Eq. (54) can be used to find its transverse momentum $\vec{q}_{{\rm inv},T}$. Next we discuss the case of multiple invisible particles in the same event.

2. Two invisible daughter particles

A well-motivated class of new-physics models that generically predict a $\not{E}_T$ signature includes models with dark-matter candidates. In such models, the lifetime of the dark-matter particle is typically protected by an exact discrete symmetry, which implies that the collider signals will involve not one but two decay chains, each terminating in a dark-matter particle invisible in the detector. A few simple examples of such event topologies are shown in Fig. 11.

We start with the simplest case of a single two-body decay on each side of the event as in Fig. 11(a), which was the inspiration for the invention of the well-known Cambridge M_{T2} variable (Lester and Summers, 1999; Barr, Lester, and Stephens, 2003). Now we can form two transverse parent masses: $M_{TP_1}(\vec{q}_{1T}, m_{a_0})$ for the first parent particle $P_1 = A_1$, which depends on the transverse momentum $\vec{q}_{1T}$ and the mass m_{a_0} of the invisible particle a_0, and $M_{TP_2}(\vec{q}_{2T}, m_{b_0})$ for the second parent particle $P_2 = B_1$, which depends on the transverse momentum $\vec{q}_{2T}$ and the mass m_{b_0} of the invisible particle

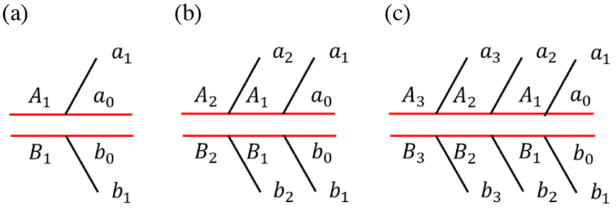

FIG. 11. Event topologies of pair-produced heavy resonances, each of which undergoes (a) a one-step, two-body decay, (b) a two-step, two-body decay, and (c) a three-step, two-body decay.

b_0. For simplicity, in what follows we assume symmetric event topologies, in which the parents A_1 and B_1 as well as the daughters a_0 and b_0 are the same [this assumption can be easily avoided; see Barr, Gripaios, and Lester (2009) and Konar *et al.* (2010a)]. In that case, the kinematics is governed by a single parent mass $m_P = m_{A_1} = m_{B_1}$ and a single daughter mass $m_0 = m_{a_0} = m_{b_0}$. If $\vec{q}_{1T}$ and $\vec{q}_{2T}$ are separately known, we would be assured that

$$\max[M_{TP_1}(\vec{q}_{1T}, m_0), M_{TP_2}(\vec{q}_{2T}, m_0)] \le m_P. \tag{57}$$

However, $\vec{q}_{1T}$ and $\vec{q}_{2T}$ are not uniquely fixed by the $\vec{\not{p}}_T$ constraint, as they are related by

$$\vec{q}_{1T} + \vec{q}_{2T} = \vec{\not{p}}_T, \tag{58}$$

and the best that we can do is to perform a minimization over all possible partitions of the $\vec{\not{p}}_T$ into $\vec{q}_{1T}$ and $\vec{q}_{2T}$. This leads to the following definition of the Cambridge M_{T2} variable (Lester and Summers, 1999; Barr, Lester, and Stephens, 2003):

$$M_{T2}(\tilde{m}) \equiv \min_{\vec{q}_{1T},\vec{q}_{2T}} \{\max[M_{TP_1}(\vec{q}_{1T}, \tilde{m}), M_{TP_2}(\vec{q}_{2T}, \tilde{m})]\},$$
$$\vec{\not{p}}_T = \vec{q}_{1T} + \vec{q}_{2T}, \tag{59}$$

where the *a priori* unknown daughter mass m_0 has been replaced by a test mass parameter $\tilde{m}$. This construction guarantees on an event-by-event basis that

$$m_0 \le M_{T2}(\tilde{m} = m_0) \le m_P. \tag{60}$$

This fact can be used to construct the M_{T2} distribution, read off its upper kinematic end point $M_{T2}^{\max}$, and interpret it as

$$M_{T2}^{\max}(\tilde{m} = m_0) = m_P. \tag{61}$$

The M_{T2} concept can be readily applied to the more complex event topologies in Figs. 11(b) and 11(c), where one has several choices of designating parent and daughter particles, leading to a collection of different subsystem M_{T2} variables (Kawagoe, Nojiri, and Polesello, 2005; Burns *et al.*, 2009). In general the minimization in Eq. (59) has to be done numerically with one of several available public codes; see Table V in Appendix C. However, analytical solutions have been derived for certain special cases (Barr, Lester, and Stephens, 2003; Lester and Barr, 2007; Cho *et al.*, 2008a, 2008b; Lester, 2011; Lally and Lester, 2012). For example, when the minimization results in the case of $M_{TP_1} = M_{TP_2}$, which is known as the balanced solution M_{T2}^B, the analytic expression for the symmetric M_{T2} variable is given by (Lester and Barr, 2007; Cho *et al.*, 2008a)

$$[M_{T2}^B(\tilde{m})]^2 = \tilde{m}^2 + A_T + \sqrt{\left(1 + \frac{4\tilde{m}^2}{2A_T - m_1^2 - m_2^2}\right)(A_T^2 - m_1^2 m_2^2)}, \tag{62}$$

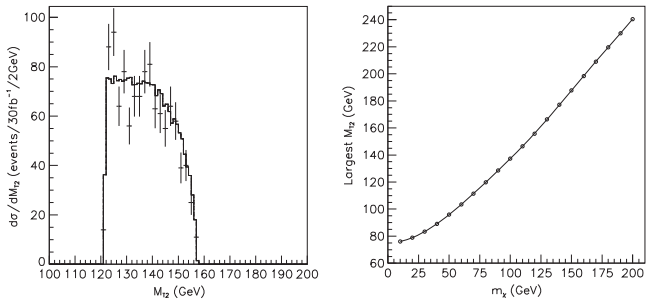

FIG. 12. Left panel: M_{T2} distribution for slepton production $pp \to \tilde{\ell}\tilde{\ell}^* \to \ell^+\ell^- + \vec{\not{p}}_T$ at the LHC, assuming the actual value for the test mass $\tilde{m}$. The slepton and neutralino masses are set at $m_{\tilde{\ell}} = 157.1$ GeV and $m_{\tilde{\chi}_1^0} = 121.5$ GeV, respectively. Right panel: values of $m_{\tilde{\ell}}$ as a function of test mass. From Lester and Summers, 1999.

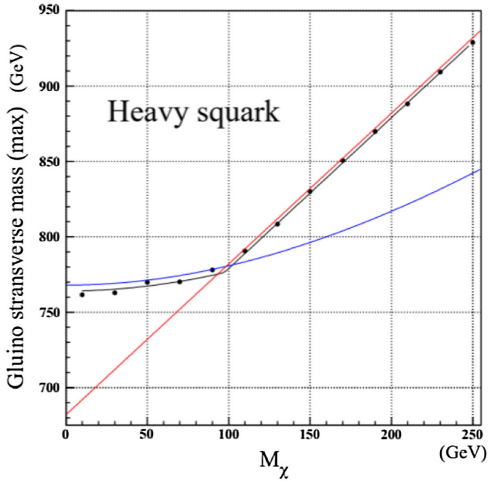

FIG. 13. $M_{T2}^{\max}$ as a function of the test mass for gluino pair production at the LHC $pp \to \tilde{g}\tilde{g} \to jjjj + \vec{\not{p}}_T$. In this example, the squarks are assumed to be heavy, so the gluino decay is three body: $\tilde{g} \to q\bar{q}\tilde{\chi}_1^0$. From Cho *et al.*, 2008a.

where m_i, $\vec{p}_{iT}$, and E_{iT} are, respectively, the mass, the transverse momentum, and the transverse energy of the visible particles in the ith decay chain ($i = 1, 2$) and A_T is the following shorthand notation introduced by Cho *et al.* (2008b):

$$A_T = E_{1T}E_{2T} + \vec{p}_{1T} \cdot \vec{p}_{2T}. \tag{63}$$

A sample distribution of M_{T2} (Lester and Summers, 1999) for slepton production $pp \to \tilde{\ell}\tilde{\ell}^* \to \ell^+\ell^- + \vec{\not{p}}_T$ at the LHC is shown in the left panel of Fig. 12 for a slepton mass $m_{\tilde{\ell}} = 157.1$ GeV and a neutralino mass $m_{\tilde{\chi}_1^0} = 121.5$ GeV. The test mass $\tilde{m}$ is taken to be equal to the true mass of the missing particle $\tilde{m} = m_{\tilde{\chi}_1^0}$. The distribution shows the expected end point [Eq. (61)] at $M_{T2}^{\max} = m_{\tilde{\ell}} = 157.1$ GeV. The right panel of Fig. 12 shows the measured values of $M_{T2}^{\max}$ as a function of the test mass $\tilde{m}$. The expected analytical relationship for this simplest event topology is given by (Cho *et al.*, 2008a, 2008b; Burns *et al.*, 2009; Barr, Khoo *et al.*, 2011)

$$M_{T2}^{\max} = \mu + \sqrt{\mu^2 + \tilde{m}^2}, \tag{64}$$

where the parameter μ is a combination of the parent and daughter physical masses

$$\mu \equiv \frac{m_{\tilde{\ell}}^2 - m_{\tilde{\chi}_1^0}^2}{2m_{\tilde{\ell}}}. \tag{65}$$

When the end point ($M_{T2}^{\max}$) of M_{T2} is interpreted as the mass of the decaying particle according to Eq. (61), Fig. 12 reduces the two-dimensional mass-parameter space ($m_{\tilde{\chi}_1^0}$, $m_{\tilde{\ell}}$) to one dimension. One additional independent measurement would then be able to fix the masses of both the parent and daughter particles. In fact, M_{T2} itself could provide such a measurement via a kink structure, which appears because the solution to the minimization in the defining equation (59) for M_{T2} flips from one momentum configuration of $\vec{q}_{1T}$ and $\vec{q}_{2T}$ to another. Such a flip may arise in a number of physics circumstances, for instance, due to nontrivial invariant mass in the visible sector (Cho *et al.*, 2008a, 2008b), due to initial-state radiation (Barr, Gripaios, and Lester, 2008; Gripaios, 2008), or due to upstream momentum from decays further up the chain (Burns *et al.*, 2009). Figure 13 shows an example of such a kink structure that appears in the gluino pair production at the LHC $pp \to \tilde{g}\tilde{g} \to jjjj + \vec{\not{p}}_T$ (Cho *et al.*, 2008a). The black dots are data points generated via simulation and the blue curve and the red straight line represent the best fits for $\tilde{m} < m_{\tilde{\chi}_1^0}$ and $\tilde{m} > m_{\tilde{\chi}_1^0}$, respectively. Their intersection corresponds to the true mass input $(m_{\tilde{\chi}_1^0}, m_{\tilde{\ell}}) = (780.3, 97.9)$ GeV. Another example of an M_{T2} kink structure is discussed in Fig. 22.

An interesting observation is that the result from the minimization involved in the M_{T2} definition provides an ansatz $\tilde{\mathbf{q}}_{iT}$ for the transverse momentum of each missing particle (Cho *et al.*, 2009). The accuracy of this approximation improves in the vicinity of the upper kinematic end point [Eq. (61)] of the M_{T2} distribution, i.e., when $M_{T2} \approx m_P$. Armed with the ansatz for the transverse invisible momenta, one can use on-shell conditions to reconstruct the longitudinal momenta of the missing particles. In other words, fixing $\vec{q}_{iT} = \tilde{\mathbf{q}}_{iT}$, the longitudinal momenta of the missing particles can be determined as

$$\tilde{q}_{iL}^{\pm}(\tilde{m}) = \frac{1}{(E_{iT})^2}\left[p_{iL}A_i \pm \sqrt{p_{iL}^2 + (E_{iT})^2}\sqrt{A_i^2 - (E_{iT}E_{iT}^{\chi})^2}\right], \tag{66}$$

where $E_{iT} = \sqrt{m_i^2 + |\mathbf{p}_{iT}|^2}$, $E_{iT}^{\chi} = \sqrt{\tilde{m}^2 + |\tilde{\mathbf{q}}_{iT}|^2}$, and $A_i = (1/2)\{[M_{T2}^{\max}(\tilde{m})]^2 - \tilde{m}^2 - m_i^2\} + \vec{p}_{iT} \cdot \tilde{\mathbf{q}}_{iT}$ for $\vec{q}_{iT} = \tilde{\mathbf{q}}_{iT}$. This method of finding the momenta of missing particles is known as M_{T2}-assisted on-shell (MAOS) reconstruction (Cho *et al.*, 2009). Figure 14 illustrates the accuracy of the MAOS reconstruction for gluino pair production at the LHC $pp \to \tilde{g}\tilde{g} \to (jj\tilde{\chi}_1^0)(jj\tilde{\chi}_1^0)$, with $m_{\tilde{\chi}_1^0} = 122$ GeV and $m_{\tilde{g}} = 779$ TeV. The MAOS reconstruction has been used for many collider studies, including Higgs boson searches

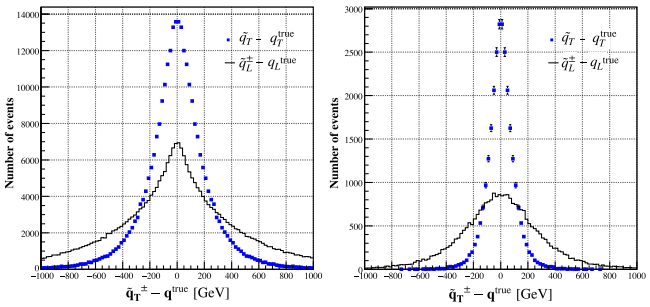

FIG. 14. The distributions of $\tilde{q}^{\pm} - q^{\text{true}}$ for the full event set (left panel), and for the top 10% events closest to the M_{T2} end point [Eq. (61)] (right panel). Here the MAOS momenta were constructed with $\tilde{m} = 0$. From Cho *et al.*, 2009.

(Choi *et al.*, 2009; Choi, Lee, and Park, 2010; Barr, French *et al.*, 2011), heavy resonance searches (Park, 2011), and spin measurement (Guadagnoli and Park, 2014).

In the presence of upstream (ISR) transverse momentum $\vec{P}_T$ and for arbitrary configurations of the visible transverse momenta $\vec{p}_{1T}$ and $\vec{p}_{2T}$, a general analytical formula for the calculation of M_{T2} is still lacking. Konar *et al.* (2010b) and Matchev and Park (2011) discussed an interesting way of removing the effect of the ISR and retrieving an analytic solution. The basic idea is to decompose the transverse momenta $\vec{p}_{1T}$ and $\vec{p}_{2T}$ further onto the direction ($T_\parallel$) defined by the $\vec{P}_T$ vector and the direction ($T_\perp$) orthogonal to it,

$$\vec{p}_{iT_\parallel} \equiv \frac{1}{P_T^2}(\vec{p}_{iT} \cdot \vec{P}_T)\vec{P}_T, \tag{67}$$

$$\vec{p}_{iT_\perp} \equiv \vec{p}_{iT} - \vec{p}_{iT_\parallel} = \frac{1}{P_T^2}\vec{P}_T \times (\vec{p}_{iT} \times \vec{P}_T), \tag{68}$$

and a similar approach is followed for the transverse momenta $\vec{q}_{1T}$ and $\vec{q}_{2T}$ of the daughters and for $\vec{\not{p}}_T$. Now consider the corresponding one-dimensional (1D) decompositions of the transverse parent masses

$$M^2_{T_\parallel P_i} \equiv m_i^2 + \tilde{m}^2 + 2(E_{iT_\parallel}E^{\chi}_{iT_\parallel} - \vec{p}_{iT_\parallel} \cdot \vec{q}_{iT_\parallel}),$$
$$M^2_{T_\perp P_i} \equiv m_i^2 + \tilde{m}^2 + 2(E_{iT_\perp}E^{\chi}_{iT_\perp} - \vec{p}_{iT_\perp} \cdot \vec{q}_{iT_\perp})$$

in terms of the 1D projected analogs of the transverse energy

$$E_{iT_\parallel} \equiv \sqrt{m_i^2 + |\vec{p}_{iT_\parallel}|^2}, \qquad E_{iT_\perp} \equiv \sqrt{m_i^2 + |\vec{p}_{iT_\perp}|^2},$$
$$E^{\chi}_{iT_\parallel} \equiv \sqrt{\tilde{m}^2 + |\vec{q}_{iT_\parallel}|^2}, \qquad E^{\chi}_{iT_\perp} \equiv \sqrt{\tilde{m}^2 + |\vec{q}_{iT_\perp}|^2}.$$

Now we define 1D M_{T2} decompositions in complete analogy with the standard M_{T2} definition (59) as

$$M_{T2_\parallel} \equiv \min_{\vec{q}_{1T_\parallel} + \vec{q}_{2T_\parallel} = \vec{\not{P}}_{T_\parallel}} \{\max[M_{T_\parallel P_1}, M_{T_\parallel P_2}]\}, \tag{69}$$

$$M_{T2_\perp} \equiv \min_{\vec{q}_{1T_\perp} + \vec{q}_{2T_\perp} = \vec{\not{P}}_{T_\perp}} \{\max[M_{T_\perp P_1}, M_{T_\perp P_2}]\}. \tag{70}$$

By construction, $M_{T2\perp}$ does not suffer from ISR effects, since it concerns the direction orthogonal to the ISR. Therefore one can use the existing formula (62) to compute $M_{T2_\perp}$ analytically. Some examples of the doubly projected variables are shown in Fig. 15 by taking dilepton top quark production as an example. See Barr, Khoo *et al.* (2011) for more details on the different types of projections (mass-preserving "⊥," speed-preserving "∨," and massless "°" projections) and the order of projection and agglomeration of visible particles.

M_{T2} has various applications in collider physics and has been further developed for more complicated topologies. Examples include $M_{T\text{Gen}}$ (avoiding the combinatorics problem by iterating over all possible partitions of the visible set of final-state particles) (Barr, Lester, and Stephens, 2003; Lester and Barr, 2007), asymmetric M_{T2} (associated production and nonidentical pair decays) (Barr, Gripaios, and Lester, 2009; Konar *et al.*, 2010a; Agashe *et al.*, 2011), generalizations to the case with multiple invisible particles (Mahbubani, Matchev, and Park, 2013), applications to dark-matter stabilization symmetries (Agashe *et al.*, 2011; Kim, 2016), CDF top quark mass measurements using M_{T2} (Aaltonen *et al.*, 2010), CMS top quark mass measurements using $M_{b\ell}$, M_{T2}, and $M_{T2,\perp}$/MAOS (CMS Collaboration, 2012, 2016), and ISR tagging (Alwall *et al.*, 2009; Kim and Kong, 2015). Since the analytical expression for the general case is unknown, one must use a code to compute M_{T2} numerically (Cho, Gainer *et al.*, 2016; Park, 2021b). Special algorithms have been suggested for faster and more accurate calculations (Cheng and Han, 2008; Lester and Nachman, 2015). Some of these codes are summarized in Table V.

Another mass-constraining variable is the M_2 variable (Barr, Khoo *et al.*, 2011; Cho, Gainer *et al.*, 2014, 2016; Cho *et al.*, 2015), which is the $(3+1)$-dimensional version of Eq. (59),

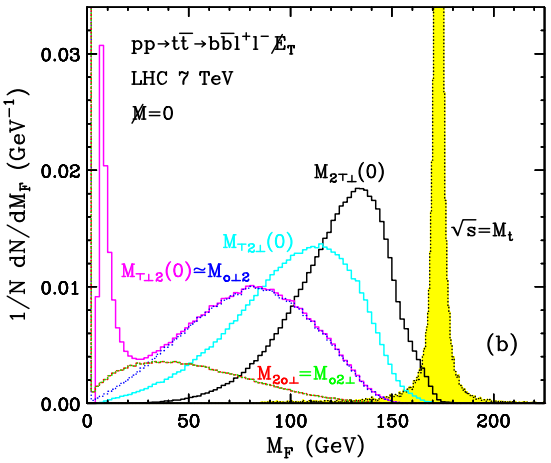

FIG. 15. Distributions of various doubly projected variables in the case of dilepton top quark production: $M_{2T\perp}$ (black curve), $M_{T2\perp}$ (cyan curve), $M_{T\perp 2}$ (magenta curve), $M_{2^\circ\perp}$ (red curve), $M_{\hat{2}\perp}$ (green curve), and $M_{\hat{\perp}2}$ (blue curve). The yellow-shaded distribution gives the average top quark mass in the event. The different types of projections (mass-preserving ⊥, speed-preserving ∨, and massless °) were defined by Barr, Khoo *et al.* (2011). From Barr, Khoo *et al.*, 2011.

$$M_2(\tilde{m}) \equiv \min_{\vec{q}_1,\vec{q}_2}\{\max\left[M_{P_1}(\vec{q}_1,\tilde{m}), M_{P_2}(\vec{q}_2,\tilde{m})\right]\},$$
$$\vec{q}_{1T} + \vec{q}_{2T} = \vec{\not{p}}_T, \tag{71}$$

where we use the actual parent masses M_{P_i} from Eq. (51) instead of their transverse masses M_{TP_i} from Eq. (55). The computation of M_{P_i} involves the three-dimensional momenta of the visible and invisible particles in the event. Therefore, the minimization is now performed over the three-component momentum vectors $\vec{q}_1$ and $\vec{q}_2$ (Barr, Khoo *et al.*, 2011; Cho, Gainer *et al.*, 2014, 2016; Cho *et al.*, 2015). Note that at hadron colliders the longitudinal invisible momenta q_{iz} are unconstrained since the longitudinal momentum of the initial state is *a priori* unknown.

At this point the two definitions (59) and (71) are equivalent, in the sense that the resulting two variables M_{T2} and M_2 will have the same numerical value (Ross and Serna, 2008; Barr, Khoo *et al.*, 2011; Cho, Gainer *et al.*, 2014). However, M_2 begins to differ from M_{T2} when applying additional kinematic constraints beyond the missing transverse momentum condition $\vec{q}_{1T} + \vec{q}_{2T} = \vec{\not{p}}_T$. The M_2 variable can then be further refined, and one can obtain the following nontrivial variants (Cho, Gainer *et al.*, 2014):

$$M_{2CX}(\tilde{m}) \equiv \min_{\vec{q}_1,\vec{q}_2}\{\max\left[M_{P_1}(\vec{q}_1,\tilde{m}), M_{P_2}(\vec{q}_2,\tilde{m})\right]\},$$
$$\vec{q}_{1T} + \vec{q}_{2T} = \vec{\not{p}}_T,$$
$$M_{P_1} = M_{P_2}, \tag{72}$$

$$M_{2XC}(\tilde{m}) \equiv \min_{\vec{q}_1,\vec{q}_2}\{\max\left[M_{P_1}(\vec{q}_1,\tilde{m}), M_{P_2}(\vec{q}_2,\tilde{m})\right]\},$$
$$\vec{q}_{1T} + \vec{q}_{2T} = \vec{\not{p}}_T,$$
$$M^2_{R_1} = M^2_{R_2}, \tag{73}$$

$$M_{2CC}(\tilde{m}) \equiv \min_{\vec{q}_1,\vec{q}_2}\{\max\left[M_{P_1}(\vec{q}_1,\tilde{m}), M_{P_2}(\vec{q}_2,\tilde{m})\right]\},.$$
$$\vec{q}_{1T} + \vec{q}_{2T} = \vec{\not{p}}_T,$$
$$M_{P_1} = M_{P_2},$$
$$M^2_{R_1} = M^2_{R_2}. \tag{74}$$

In Eqs. (72)–(74) M_{P_i} (M_{R_i}) is the mass of the parent (relative) particle in the ith decay chain and the subscript C indicates that an equal mass constraint is applied for the two parents (when C is in the first position) or for the relatives (when C is in the second position). The subscript X simply means that no such constraint is applied. In any given subsystem, these variables are related as follows (Cho, Gainer *et al.*, 2014):

$$M_{T2} = M_{2CX} \le M_{2XC} \le M_{2CC}. \tag{75}$$

Besides constraints enforcing mass equality between two different particles, we can also enforce the measured values of some masses. For example, consider the dilepton $t\bar{t}$ event topology, where each top quark decays leptonically as $t \to bW^+ \to b\ell^+\nu$. We could use the experimentally measured W-boson mass m_W and introduce the following further constrained variable:

$$M^{(b\ell)}_{2CW}(\tilde{m}=0) \equiv \min_{\vec{q}_1,\vec{q}_2}\{\max\left[M_{t_1}(\vec{q}_1,\tilde{m}), M_{t_2}(\vec{q}_2,\tilde{m})\right]\},$$
$$\vec{q}_{1T} + \vec{q}_{2T} = \vec{\not{p}}_T,$$
$$M_{t_1} = M_{t_2},$$
$$M_{W_1} = M_{W_2} = m_W. \tag{76}$$

Similarly, using the measured mass m_t of the top quark, we can define a new variable in the (ℓ) subsystem,

$$M^{(\ell)}_{2Ct}(\tilde{m}=0) \equiv \min_{\vec{q}_1,\vec{q}_2}\{\max\left[M_{W_1}(\vec{q}_1,\tilde{m}), M_{W_2}(\vec{q}_2,\tilde{m})\right]\},$$
$$\vec{q}_{1T} + \vec{q}_{2T} = \vec{\not{p}}_T,$$
$$M_{W_1} = M_{W_2},$$
$$M_{t_1} = M_{t_2} = m_t. \tag{77}$$

Just like the minimization in the M_{T2} calculation allowed for the MAOS reconstruction of invisible momenta, the minimization in the M_2 computation provides a flexible and convenient reconstruction of the full missing momenta (M_2-assisted on-shell reconstruction). Figure 16 compares the reconstructed top mass using a variety of MAOS and M_2 reconstruction schemes. In general the momentum ansatz obtained from M_2 allows a sharper distribution with a shorter tail. This is due to better precision in the missing momentum reconstruction, as illustrated in Fig. 17. In addition to invisible momentum reconstruction (Kim *et al.*, 2017), M_2 has been used in various collider analyses, including applications to Higgs mass measurements (Konar and Swain, 2016b), new particle mass measurements (Lim, 2016; Baer *et al.*, 2017; Kim *et al.*, 2017), distinguishing symmetric and asymmetric events (Lim, 2016), resolving combinatorial ambiguities (Debnath, Kim *et al.*, 2017; Alhazmi *et al.*, 2022), measurements of the top-Higgs Yukawa *CP* structures (Gonçalves,

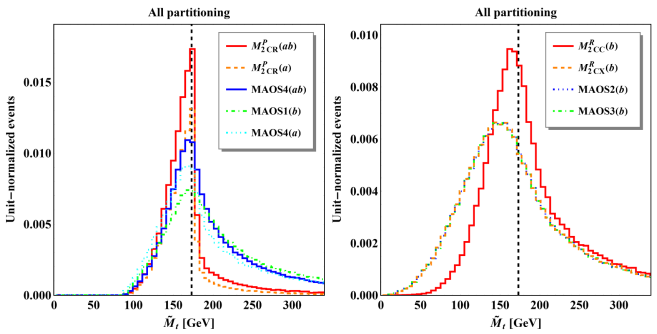

FIG. 16. Comparison of the MAOS and M_2-assisted methods for top mass reconstruction. Left panel: distributions of the reconstructed top mass $\tilde{M}_t$ with methods that use two mass inputs (the W-boson mass and the neutrino mass): the three MAOS methods MAOS4(ab) (blue solid line), MAOS1(b) (green dot-dashed line), and MAOS4(a) (cyan dotted line) and the two M_2-based methods, $M_{2CR}(ab)$ (red solid line) and $M_{2CR}(a)$ (orange dashed line). Right panel: distributions of the reconstructed top mass $\tilde{M}_t$ with methods that use a single mass input (the neutrino mass): MAOS2(b) (blue dotted line) and MAOS3(b) (green dot-dashed line), as well as $M_{2CX}(b)$ (orange dashed line) and $M_{2CC}(b)$ (red solid line). From Kim *et al.*, 2017.

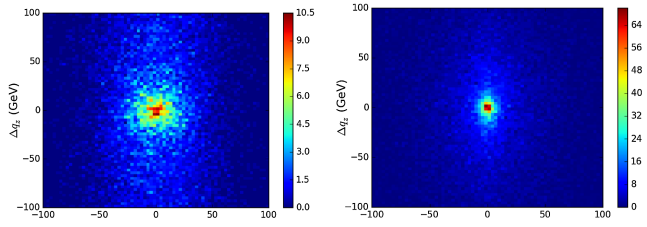

FIG. 17. Correlations between Δq_z and Δq_x for MAOS1$(b\ell; m_t)$ (left panel) and $M_{2Ct}^{(\ell)}$ (right panel). From Debnath, Kim *et al.*, 2017.

Kong, and Kim, 2018; Gonçalves *et al.*, 2022), applications to compressed top searches (Cho *et al.*, 2015), Z' searches (Kim, Lee, and Park, 2015), applications in the antler topology (Konar and Swain, 2016a), etc. (Konar and Swain, 2016a,2016b, 2017; Swain and Konar, 2015).

There are a few other variants of the transverse mass. The cotransverse mass M_C and the contransverse mass M_{CT} are defined as (Tovey, 2008)

$$M_C^2 = (E_1 + E_2)^2 - (\vec{p}_1 - \vec{p}_2)^2 = m_1^2 + m_2^2 + 2(E_1E_2 + \vec{p}_1 \cdot \vec{p}_2), \tag{78}$$

$$M_{CT}^2 = (E_{1T} + E_{2T})^2 - (\vec{p}_{1T} - \vec{p}_{2T})^2 = m_1^2 + m_2^2 + 2(E_{1T}E_{2T} + \vec{p}_{1T} \cdot \vec{p}_{2T}), \tag{79}$$

where E_i and $\vec{p}_i$ are the visible energy and three-momentum in the ith branch and E_{iT} and $\vec{p}_{iT}$ are the corresponding transverse energy and transverse momentum. They satisfy $M_C \geq M_{CT}$, just like $M \geq M_T$. An interesting property of the M_C variable is that it is invariant under the back-to-back boost of the two visible systems.

Analogous to the stransverse mass M_{T2}, the constransverse mass variable M_{CT2} is defined as (Cho, Kim, and Kim, 2010; Barr, Gwenlan *et al.*, 2011; Cho, Klemm, and Nojiri, 2011)

$$M_{CT2} = \min_{\vec{q}_{1T}+\vec{q}_{2T}=\not{\vec{p}}_T} [\max\{M_{CT}^{(1)}, M_{CT}^{(2)}\}], \tag{80}$$

where each $M_{CT}^{(i)}$ $(i = 1, 2)$ is applied to the semi-invisible decay of the parent particle P_i.

Another mass variable M_{2C} is defined as the minimum four-dimensional mass

$$M_{2C}^2 = \min_{q_1, q_2} (p_1 + q_1)^2 \tag{81}$$

under the following constraints:

$$(p_1 + q_1)^2 = (p_2 + q_2)^2, \tag{82}$$

$$q_1^2 = q_2^2, \tag{83}$$

$$\vec{q}_{1T} + \vec{q}_{2T} = \not{\vec{p}}_T, \tag{84}$$

$$\sqrt{(p_1 + q_1)^2} - \sqrt{(q_1)^2} = m_P - m_0, \tag{85}$$

where the parent-daughter mass difference in the last constraint is assumed to be known from a preliminary measurement of an invariant mass end point [Eq. (43)] (Ross and Serna, 2008). The M_{2C} mass variable is bounded by the parent mass ($M_{2C} \leq m_P$).

Another set of kinematic variables extensively used by the CMS Collaboration in its searches for supersymmetry is the razor kinematic variables (Chatrchyan *et al.*, 2014; Khachatryan *et al.*, 2015b; Sirunyan *et al.*, 2019a). They are known to be sensitive to large mass differences between the parent particle and the invisible particles at the end of a decay chain. The razor variables are defined as (Rogan, 2010)

$$M_R^2 = (E_1 + E_2)^2 - (p_{1z} + p_{2z})^2, \tag{86}$$

$$(M_T^R)^2 = \tfrac{1}{2}[\not{E}_T(p_{1T} + p_{2T}) - \not{\vec{p}}_T \cdot (\vec{p}_{1T} + \vec{p}_{2T})], \tag{87}$$

$$R^2 = \left(\frac{M_T^R}{M_R}\right)^2. \tag{88}$$

For QCD multijet background events, the distributions in both M_R and R^2 fall exponentially, while for signal events they peak at finite values. Note that M_R is precisely the first term in the definition (34) of the $\sqrt{\hat{s}}_{\min}^{(\mathrm{sub})}$ variable. This is not by accident, since both variables are targeting the mass scale of the parent particle production.

C. Singularity variables

The geometrical features of the high-dimensional phase space available to a given event topology are largely washed out when projecting to a single one-dimensional event observable. The so-called singularity variables (De Rujula and Galindo, 2012; Matchev and Shyamsundar, 2020; Rujula and Galindo, 2011), however, provide an intuitive way to retain high-dimensional features as singularities in the corresponding one-dimensional kinematic distributions. The origin of such singularities is well understood—similar to the phenomenon of caustics in optics, they are formed at points where the projection of the allowed phase space onto the observable space gets folded; see Fig. 18 for an illustration.

As previously discussed, such projections are inevitable in the presence of invisible momenta in the event $\{q\}$ since event observables must be constructed out of visible momenta $\{p\}$ only. The geometrical structure in the allowed higher-dimensional phase space is imposed by a certain set of kinematic conditions (constraints)

$$f_\alpha(\{p\}, \{q\}) = 0, \qquad \alpha = 1, 2, \ldots \tag{89}$$

that arise in the assumed event topology. Mathematically the singularity condition is then expressed as the reduction in the rank of the Jacobian matrix of the coordinate transformation from the relevant set of kinematic constraints f_α to $\{q\}$, which is why such singularities are sometimes known as Jacobian peaks. Explicitly,

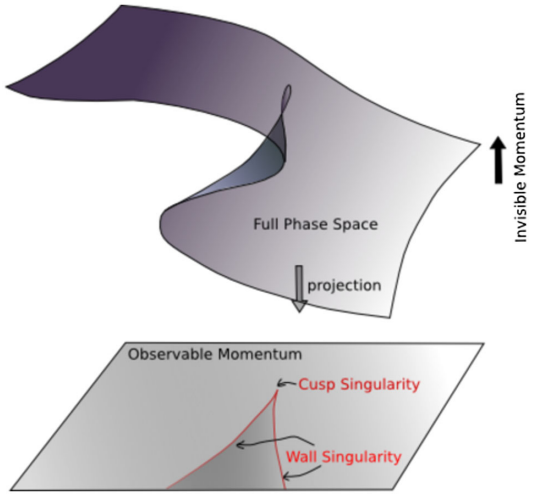

FIG. 18. Schematic depiction of the projection of the full phase space onto the space of observable momenta illustrating how folds in the allowed full phase space result in wall singularities in the observable space. From Kim, 2010.

$$\det\left(\frac{\partial f_\alpha}{\partial q^\mu}\right) = 0. \tag{90}$$

Given an event topology, the general procedure for deriving the singularity coordinate from Eq. (90) was discussed and illustrated by Matchev and Shyamsundar (2020) for the case of square Jacobian matrices and by Kim (2010) for the general case. Among the set of singularity variables, one finds well-known examples like the transverse invariant mass M_T discussed in Sec. V.B (Rujula and Galindo, 2011; De Rujula and Galindo, 2012; Matchev and Shyamsundar, 2020), the invariant mass $M_{a_2a_1}$ of the visible decay products in the two-step, two-body cascade decay of Fig. 7(a) in three (Kim, 2010) or two spatial dimensions (Matchev and Shyamsundar, 2020), and the Cambridge M_{T2} variable from Sec. V.B (Park, 2021a). However, there are also more recently discovered singularity variables like the Δ_4 variable (Agrawal *et al.*, 2014; Debnath *et al.*, 2019), which is applicable to the three-step, two-body decay chain in Fig. 7(c), the Δ_{antler} variable (Matchev and Shyamsundar, 2020; Park, 2020) relevant to the event topology of Fig. 7(b), and the $\Delta_{t\bar{t}}$ variable (Kim, Matchev, and Shyamsundar, 2019; Matchev and Shyamsundar, 2020) relevant to the $t\bar{t}$ dilepton topology of Fig. 11(b). The singularity variables are excellent analysis tools and can serve a dual purpose: in the age of discovery they can be used to target signal-rich regions of phase space, and postdiscovery they form the basis for the focus-point method for mass measurements discussed in Sec. VIII.B.

VI. EXCLUSIVE EVENT VARIABLES: ENERGY, TIME, AND DISTANCE

In this section, we discuss a few basic quantities that are directly available in experiments and their nontrivial utilization. We begin with the energy variable followed by the timing and distance variables.

A. Energy peak

While energy is not a Lorentz-invariant quantity, the peak position in the energy distribution of a visible particle coming from a two-body decay of the heavier resonance or parent particle carries a boost-distribution-invariant property. Suppose that particle A_1 is a scalar or is produced in an unpolarized way and decays into a massless visible particle a_1 and another particle a_0 that may be visible or invisible. In the rest frame of A_1, the energy $E^*_{a_1}$ of a_1 is simply given by [recall Eq. (41) and the ensuing discussion in Sec. V.A]

$$E^*_{a_1} = \frac{m^2_{A_1} - m^2_{a_0}}{2m_{A_1}}. \tag{91}$$

In the laboratory frame, one should perform a Lorentz transformation to find the laboratory-frame energy of a_1 (E_{a_1}),

$$E_{a_1} = \gamma_{A_1} E^*_{a_1}(1 + \beta_{A_1}\cos\theta^*_{a_1}), \tag{92}$$

where $\gamma_{A_1} = (1-\beta^2_{A_1})^{-1/2}$ is the boost factor of A_1 in the laboratory frame and θ_{a_1} is the emission angle of a_1 in the A_1 rest frame with respect to $\vec{\beta}_{A_1}$. For any γ_{A_1}, $E^*_{a_1}$ is the only commonly included value in the distribution of E_{a_1}. Since A_1 is assumed to be unpolarized or scalar, $\cos\theta^*_{a_1}$ is a flat variable, and so is E_{a_1}. Therefore, whatever distribution of γ_{A_1} is given, the final E_{a_1} distribution shows a peak at $E^*_{a_1}$ (Agashe, Franceschini, and Kim, 2013). This observation was made in the context of the cosmic π^0 decay (Carlson, Hooper, and King, 1950) and then extended and generalized to the two-body decay of an unpolarized resonance at colliders (Agashe, Franceschini, and Kim, 2013; Kawabata *et al.*, 2013).

This energy-peak feature can be viewed in the logarithmic energy space. In Eq. (92), the maximum and minimum laboratory-frame energy values $E^\pm_{a_1}$ arise at $\cos\theta^*_{a_1} = \pm 1$, resulting in

$$E^\pm_{a_1} = \gamma_{A_1} E^*_{a_1}(1 \pm \beta_{A_1}), \tag{93}$$

from which one can see that the rest-frame energy $E^*_{a_1}$ is the geometric mean of the maximum and minimum laboratory-frame energies $E^\pm_{a_1}$ for any boost factor γ_{A_1},

$$(E^*_{a_1})^2 = E^+_{a_1} E^-_{a_1}. \tag{94}$$

Equation (94) further implies that $\ln E^*_{a_1}$ is the mean of $\ln E^+_{a_1}$ and $\ln E^-_{a_1}$ and the rectangular distribution in E_a for a given γ_{A_1} is log symmetric with respect to $\ln E^*_{a_1}$. Once such log-symmetric rectangular distributions (which are weighted by the γ_{A_1} distribution) are stacked up, the final E_{a_1} distribution is automatically log symmetric with respect to $\ln E^*_{a_1}$.

As suggested by Eq. (91), the extraction of $E^*_{a_1}$ implies the measurement of a mass relation between A_1 and a_0. This kinematic feature is particularly useful in a hadron collider environment where the longitudinal boosts of individual events are *a priori* unknown; i.e., the γ_{A_1} profile is unknown. In addition, since the method involves no combinatorial ambiguity, its applicability is nearly unaffected by high

particle multiplicity. If the a_0 mass is known through independent measurements and if the peak in the a_1 energy distribution is extracted, the mass of A_1 can be readily determined using Eq. (91). A well-motivated and practical physics application is the top quark mass measurement in the top quark decay $t \to bW$ through the b-jet energy-peak method of Eq. (91) (Agashe, Franceschini, and Kim, 2013) and the weight function method of Eq. (B6) (Kawabata *et al.*, 2015). The CMS Collaboration measured the top quark mass by extracting the peak in the b-jet energy distribution in the $e\mu$ channel (CMS Collaboration, 2015), as shown in Fig. 19, where the aforementioned log-symmetric feature is evident. Another SM example is the W mass determination, which uses the lepton energy spectrum in the case of associate production of leptonic W along with other particles, i.e., $pp \to WX, W \to \ell\nu_\ell$ (Bianchini and Rolandi, 2019). The method is not restricted only to SM processes but rather is applicable to new particles mass measurements; examples include mass measurements of new resonances in models of supersymmetry (Low, 2013; Agashe, Franceschini, and Kim, 2014; Agashe , Franceschini, Hong, and Kim, 2016; Agashe, Franceschini, Kim, and Wardlow, 2016; Bianchini and Rolandi, 2019) and in the context of potential cosmic γ-ray excesses (Kim and Park, 2015, 2016; Boddy *et al.*, 2016, 2017, 2018).

The crucial assumptions to retain the boost-invariant feature of the energy peak are that the visible decay product is massless and it comes from a two-body decay of an unpolarized (or scalar) heavy resonance. As some of them loosen, the validity of the method would gradually be degraded and a certain extent of prescriptions would be needed.

First, if the visible decay product has a nonzero mass, Eq. (92) is modified to

$$E_{a_1} = \gamma_{A_1}(E^*_{a_1} + p^*_{a_1}\beta_{A_1}\cos\theta^*_{a_1}), \tag{95}$$

where $p^*_{a_1}$ is the magnitude of the a_1 momentum measured in the A_1 rest frame. Unlike the massless case, $E^*_{a_1}$ is no longer contained in the E_{a_1} distribution for any boost γ_{A_1}. If $\gamma_{A_1} > \gamma^{\rm cr}_{A_1} \equiv 2\gamma^*_{a_1} - 1$, with $\gamma^*_{a_1}$ the boost factor of a_1 in the A_1 rest frame, the minimum E_{a_1} occurring with $\cos\theta^*_{a_1} = -1$ becomes larger than $E^*_{a_1}$ (Agashe, Franceschini, and Kim, 2013). Therefore, for the γ_{A_1} profile extending beyond $\gamma^{\rm cr}_{A_1}$, the peak in the overall E_{a_1} distribution may be larger than $E^*_{a_1}$. In the case of top quark decay, $\gamma^*_b \approx 15$ and hence $\gamma^{\rm cr}_t \approx 450$. At the LHC, such a large boost factor of the top quark is kinematically inaccessible, so the energy-peak method can safely go through. However, if m_{a_1} is too large with respect to $m_{A_1} - m_{a_0}$, the shift of the energy peak is unavoidable. Nevertheless, one can still extract $E^*_{a_1}$, modeling the energy distribution by appropriately accommodating the shift. See Agashe, Franceschini, Hong, and Kim (2016) for a more detailed discussion.

Second, once the decay of interest is accompanied by additional decay products, $\cos\theta^*_{a_1}$ is no longer a flat variable and hence the argument breaks down. It was analytically demonstrated that the resulting peak position is always less than the $E^*_{a_1}$ value predicted in the associated multibody decay process of A_1 (Agashe *et al.*, 2013). In the top quark decay, the b quark often comes with a hard gluon emission in the final state that is not captured as part of the b jet. Thus, the contamination from such $t \to bWg$ events inevitably induces a systematic error in the E^*_b extraction.[6] The systematics was assessed in the top quark decay at next-to-leading order by Agashe, Franceschini, Kim, and Schulze (2016), who claimed that a $\lesssim 0.5\%$ level of the associated systematic error would be achievable for a 1% jet energy scaling uncertainty. Another approach to treating the multibody decays involving an invisible decay product is to interpret the A_1 decay as an effective two-body decay to a_0 and a composite visible system. Assuming that the visible particles are all massless, their invariant mass $M_{\rm vis}$ spans from 0 to $m_{A_1} - m_{a_0}$. One can then divide $M_{\rm vis}$ space into pieces, and for each such phase-space slice the method for the massive visible particle that was discussed earlier can be applied (Agashe, Franceschini, Kim, and Wardlow, 2016).

Finally, polarized production of nonscalar A_1 induces a nontrivial angular dependence of a_1; i.e., $\cos\theta^*_{a_1}$ is nonflat. Therefore, the peak position in the overall E_{a_1} distribution can be either larger or smaller than $E^*_{a_1}$, depending on the underlying decay dynamics (Agashe, Franceschini, and Kim, 2013). At the LHC, the top quarks are predominantly produced via QCD; hence, they are unpolarized. However, if a certain new-physics dynamics produces polarized top quarks, an appreciable deviation from the b-jet energy peak can be interpreted as a sign of new physics. This further implies that the energy variable can be utilized as a cut to isolate the signal from SM backgrounds. This aspect of the energy peak was investigated by Low (2013) in the context of supersymmetric top quark decays.

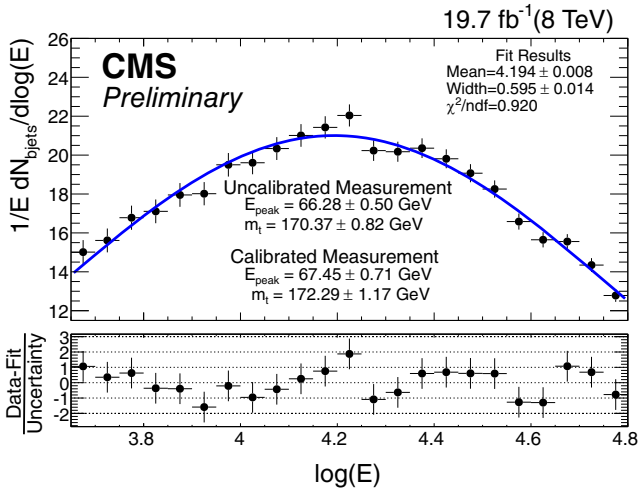

FIG. 19. CMS top quark mass measurement using the energy-peak method in the energy distribution of b jets from the top quark decay $t \to bW$. The distribution is log symmetric with respect to $\ln E^*_b$, and the fit was performed with a Gaussian template. From CMS Collaboration, 2015.

[6]By contrast, initial-state radiation from either incoming partons or the top quark itself simply reshuffles the γ_t profile, and hence it does not ruin the boost-invariant feature (Agashe, Franceschini, and Kim, 2013).

Energy peaks can also be applied in lepton colliders, where the predominance of electroweak interactions can potentially bring in more effects related to polarization. As one of the main top quark sources in e^+e^- programs is the production close to threshold, where particular care is needed to account for the production of bound state and slowly moving top quarks. Bach *et al.* (2018) studied threshold effects on the energy spectrum of a b quark at a 380 GeV e^+e^- collider. As the production of top quarks at threshold strengthens the validity of the arguments behind the invariance of the energy peak, the corrections to the energy distribution are found to be localized compared to the corrections to the transverse momentum.

The utility of the energy peak is not limited to particle mass measurements and cutting for signal versus background discrimination. A representative example is to distinguish the two-body decay topology from the ≥ 3-body ones. Imagine two scenarios where each of the pair-produced A_1's follows either $A_1 \to a_1 a_0$ (i.e., two-body topology) or $A_1 \to a_1 a_0 a_0'$ (i.e., ≥ 3-body topology), with a_0' representing one or more additional invisible particles. It was demonstrated that the μ parameter extracted from the M_{T2} distribution via Eq. (65) is the same as (greater than) the peak position $E_{a_1}^{\text{peak}}$ for the two-body (three-body) decay scenario (Agashe *et al.*, 2013),

$$\mu = \frac{m_{A_1}^2 - m_{a_0}^2}{2m_{A_1}} \begin{cases} = E_{a_1}^{\text{peak}} & \text{for two-body decay,} \\ > E_{a_1}^{\text{peak}} & \text{for three-body decay.} \end{cases} \tag{96}$$

B. Timing

The variables in Secs. IV–VI.A involve quantities in energy-momentum space. Likewise, one may utilize the information in time-position space. Sections VI.B and VI.C are devoted to discussing variables designed with time and position information.

In principle, the timing information is useful for situations including (i) the case where the signals of interest differ from the unwanted signals (or backgrounds) by the timing at which they hit the detector system and (ii) the case where the subprocesses of the signal process come along in a time-ordered manner (for instance, sequential decays of heavy resonances). In practice, timing information becomes useful when the resolution in the timing measurement is sufficiently good and the uncertainty stemming from the particle-beam pulse spread is small enough. In many of the collider experiments (more generally, accelerator-based experiments) including the LHC, beam parameters are well under control and sufficiently narrow beam pulses can be generated. When it comes to the timing resolution, it is a few hundred pico-seconds as of run II of the LHC. Thus, its utilization is somewhat limited, especially for the physics or new-physics processes where all relevant hard interactions take place instantly.

The use of timing information is currently receiving increasing attention, however, as higher-resolution timing information allows for pileup mitigation (ATLAS Collaboration, 2018b; Butler and Tabarelli de Fatis, 2019) and improved jet tagging (Klimek, 2022), and it provides a unique handle in the search for long-lived particles (LLPs) (Liu, Liu, and Wang, 2019; Flowers *et al.*, 2020; Dienes *et al.*, 2022) that were marginally targeted in the earlier LHC operation, as its detector (for instance, ATLAS, CMS, or LHCb) was designed to be optimal for prompt processes. Therefore, for run IV the ATLAS (ATLAS Collaboration, 2018b), CMS (Butler and Tabarelli de Fatis, 2019), and LHCb Collaborations (Perazzini, Ferrari, and Vagnoni, 2022) are planning to install dedicated timing modules with timing resolution as low as 30 ps and develop appropriate trigger algorithms.

Indeed, it has been pointed out that the timing variable allows for a powerful separation between delayed new-physics signal events and SM background events, given projected upgrades and implementations of high-capability timing modules and dedicated triggers at the LHC detectors (Liu, Liu, and Wang, 2019; Flowers *et al.*, 2020; Dienes *et al.*, 2022). For example, massive enough LLPs at the LHC can travel for a finite amount of time such that their decay products arrive at detectors with time delays around nanosecond scale, unlike the light SM particles. Strategies for utilizing this time delay feature can be applied in the search for LLPs, using the initial-state radiation as a way of setting a reference timing and requiring at least one LLP to decay within the detector (Liu, Liu, and Wang, 2019). It has been demonstrated that the strategies can improve the sensitivity to the lifetime of the LLPs by 2 orders of magnitude or more (Liu, Liu, and Wang, 2019), in comparison to conventional search strategies for LLPs (Aad *et al.*, 2015b; Khachatryan *et al.*, 2015a; Coccaro *et al.*, 2016), for instance, displaced vertex searches. Examples of sensitivity reaches for the scenario where the SM Higgs decays to a pair of LLPs X are shown in Fig. 20 in terms of limits on the branching fraction of $h \to XX$ as a function of the proper decay length of X (Liu, Liu, and Wang, 2019).

The timing information is useful not only for the discovery opportunities of LLPs but also for the resonance mass reconstruction of the new particles involved in the associated decay process. Flowers *et al.* (2020) investigated the case in which LLPs are pair produced and each of them decays to an invisible particle and visible particle(s). They showed that the

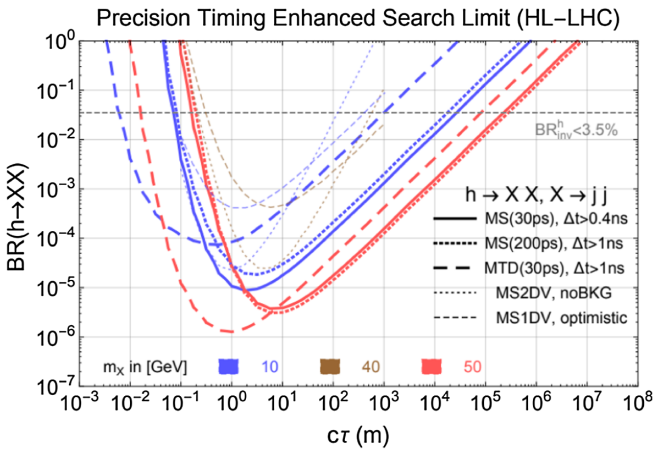

FIG. 20. 95% C.L. limits on $\text{BR}(h \to XX)$ for signal process $pp \to jh$ followed by subsequent decays $h \to XX$ and $X \to jj$, with X a new particle. From Liu, Liu, and Wang, 2019.

particle mass spectrum can be completely determined event by event, using the missing transverse momentum condition and the timing information, even in the case where the pair-produced LLPs are not identical. Another possibility that allows for the event-by-event mass measurement is the so-called tumbler scenario where a LLP decays to lighter LLPs sequentially. Dienes *et al.* (2022) studied the simplest tumbler process $A_2 \to a_2 A_1$ followed by $A_1 \to a_1 a_0$, with A_2 and A_1 LLPs, a_2 and a_1 visible particle systems, and a_0 a collider-stable particle or dark-matter candidate. They demonstrated that the masses of A_2, A_1, and a_0 can be determined with the aid of timing information, but without recourse to the missing transverse momentum measurement.

Timing is also considered to be a discriminating variable at muon colliders to suppress the beam-induced backgrounds due to muon decays (Di Benedetto *et al.*, 2018; Bartosik *et al.*, 2019, 2022; Ally *et al.*, 2022). Since muons decay as they circulate in a synchrotron, muons headed to the detector from upstream decay to electrons (and neutrinos) that convert to energetic secondary particles as they pass through the material surrounding the detector. The secondary particles that reach the detectors can be discriminated using timing information, namely, that they arrive continuously, while interesting particles from hard collisions emerge only during beam crossings.

C. Distance variables

Mass measurements are inherently energy scale measurements. However, excellent measurements of masses can in principle be conducted by accurately measuring the distances traveled by particles. The key relation is

$$\langle d \rangle = c\beta\gamma\tau_0 = \frac{\sqrt{E^2 - m^2}}{m} c\tau_0, \tag{97}$$

where $\langle d \rangle$ is the average distance traveled before decaying, τ_0 is the proper lifetime of the particle at hand, and $\gamma = E/m = (1-\beta^2)^{-1/2}$ is the usual Lorentz boost factor that governs the time dilation and length contraction. In essence, a mass measurement can be carried out from a sample of particles, all of which have identical boost factors (or, equivalently, identical energies) by measuring the average decay length of the sample and measuring elsewhere (or using theory predictions for) the proper lifetime τ_0.

A practical difficulty while pursuing this method is that in general it is difficult to find a sample of particles that are perfectly monochromatic in energy. A nonmonochromatic particle sample can be used to carry out a mass measurement if the energy distribution of these particles is sufficiently well known. The case of particles produced by parton collisions in pp or $p\bar{p}$ colliders shows how measurements of this sort require accurate knowledge of the source [i.e., parton distribution functions (PDFs) in this case].

This idea can be exploited even for particles whose lifetime is short enough to make it impossible to measure $\langle d \rangle$. If the promptly decaying particle produces an unstable long-lived particle as a decay product, it can be viewed as the source of a new sample of particles, as it inherits a certain extent of relevant information of the decaying particle. The average decay length of the unstable decay product can now be measured and turned into a mass measurement, provided that the proper lifetime and the energy distribution of the measurable decay product are sufficiently well known.

Measurements of this sort have been proposed for SM particles such as the top quark (Hill, Incandela, and Lamb, 2005). Concrete results for this strategy appeared from the CDF (Abulencia *et al.*, 2007) and CMS experiments (CMS Collaboration, 2013a). A great deal of work in these measurements is devoted to understanding the source of the unstable particles whose decay length is measured and a number of issues having something to do with the formation of hadrons and other aspects of QCD that impact the kinematics of top quark decay products.

In fact, in the case of the top quark mass measurement the accessible unstable states are B-flavored hadrons (B^+, $B_s^0, B^0, \Lambda_b^0, \ldots$) whose $c\tau_0$'s are in the range of 100 μm and hence can be measured in modern detectors, especially when they possess a typical Lorentz boost factor of $\mathcal{O}(10)$, as expected for top quark decays. Relating the top quark mass to the observed decay lengths of the B hadrons has significant complications with respect to the simple one-step monochromatic case sketched at the beginning of this section. Indeed, one has to deal with multiple species of B hadrons, each of which has a different mass and a different proper lifetime. As a consequence, the actual yield of each type of B hadrons does affect a measurement that is blind to the identification of each species. For this reason, the analyses of CDF (Abulencia *et al.*, 2007) and CMS (CMS Collaboration, 2013a) are filled with details on the treatment of hadronization effects, which become of primary interest when a subpercent measurement is attempted to be competitive with other top quark mass determinations. We refer to the previously mentioned studies for further discussion of these effects.

Concerning the use of kinematic variables, we remark that thus far the CDF (Abulencia *et al.*, 2007) and CMS Collaborations (CMS Collaboration, 2013a) have managed to relate the top quark mass and the length distribution of the B hadrons only by producing templates of the length distribution with a full chain of Monte Carlo (MC) simulations. However, the insights on the peak of the energy distribution can be translated into properties of the length distribution, as entailed by the relation among energy, mass, and decay length, as in Eq. (97). Work is under way to formulate new mass measurement strategies exploiting this insight (Agashe, 2020, 2022).

In addition to mass measurements, distance variables are useful discriminators for the identification of heavy flavor quarks and leptons. Particles with a measurably long proper lifetime such as B hadrons result in a measurable impact parameter, defined as the transverse distance of the closest approach of a track to the primary interaction vertex. This quantity can be shown (Barger and Phillips, 1987) to be largely unaffected by the boost of the decaying particle, as time dilation contributes to further displace the decay point in the laboratory frame, but at the same time length contraction makes the direction of the decay product tend to align with the decaying particle momentum. As a consequence, the characteristic decay times of particles are translated to the characteristic impact parameters, which are useful for particle identification.

Modern experiments use impact parameter information, among many other inputs, to give a likelihood for particle identification. For an explanation of the role played by the impact parameter in heavy flavor tagging, see Rizzi, Palla, and Segneri (2006). A modern incarnation that leverages the impact parameter in a neural network classifier was described by ATLAS Collaboration (2020).

A major difficulty in analyzing collider events is the necessity to disentangle the useful particles potentially bearing information on interesting phenomena from the particles stemming from ordinary collisions not carrying any useful information. Especially at hadron colliders, the collision rate is so high that a number collisions can happen for each bunch crossing. A basic tool to discriminate particles from the collisions recorded at once is the position from which these particles' momenta originate if extrapolated to the beam axis (Wells, 2014; Aaboud *et al.*, 2017b). This simple observable remains a basic ingredient for current and future experiments and is used in conjunction with the most theoretically sophisticated tools (Soyez, 2019) to remove pileup effects.

New-physics models have provided many examples of signatures involving LLPs and other exotic states (Hewett *et al.*, 2004; Meade, Reece, and Shih, 2010; Bomark *et al.*, 2014; Schwaller, Stolarski, and Weiler, 2015; Barnard *et al.*, 2016; Evans and Shelton, 2016; Lee *et al.*, 2019; Alimena *et al.*, 2020; Linthorne and Stolarski, 2021; Dienes *et al.*, 2022) that can be analyzed with observables referring to length measurements. The most basic measurements involve the Euclidean distance between the primary interaction point and the displaced vertex within the detector where the exotic particle decays. For long-lived particles, this idea can be taken to the extreme by building a dedicated detector located a significant distance away from the interaction point (Pinfold *et al.*, 2009; Feng *et al.*, 2018, 2023; Curtin *et al.*, 2019; Aielli *et al.*, 2020; Ball *et al.*, 2021; Franzosi *et al.*, 2022). A summary of the power of this approach to search for exotic states was given by Liu and Tweedie (2015) together with a comparison of the coverage of new-physics models parameter space of the equivalent "prompt" searches not exploiting length measurements. The typical prompt search quickly becomes ineffective when one considers distances greater than 100 μm − 1 cm for the lifetime of the exotic state, or the equivalent parameter that controls the appearance of displaced vertices in more complicated models. The threshold for the beginning of degradation of the prompt searches is process dependent, but the general message that the displaced vertex searches can fully fill in this gap is robust. As a matter of fact, when the experiments have looked for these exotic signals (Aaboud *et al.*, 2018c; Aad *et al.*, 2019b; Sirunyan *et al.*, 2019b, 2021b; Tumasyan *et al.*, 2021a), the bounds from displaced vertices have been stronger than the prompt counterparts.

VII. OTHER EXCLUSIVE EVENT VARIABLES

A. Dimensionless variables

The variables in Secs. IV–VI are dimensionful; hence, they allow the scale information of the underlying physics processes to be inferred. By contrast, dimensionless variables make it possible to extract scale-independent information. Here we review a few dimensionless exclusive event variables, most of which are developed for particular processes and/or event topologies.

The first example is the α_T variable (Randall and Tucker-Smith, 2008), which is introduced to efficiently reduce multijet events without a significant missing transverse momentum $\vec{\not{p}}_T$. For dijet events, it can be defined as (Chatrchyan *et al.*, 2013b)

$$\alpha_T = \frac{E_T^{j_2}}{m_T}, \tag{98}$$

where $E_T^{j_2}$ is the transverse energy of the second hardest jet and $m_T = \sqrt{(E_T^{j_1} + E_T^{j_2})^2 - (\vec{p}_T^{\,j_1} + \vec{p}_T^{\,j_2})^2}$ is the transverse mass of the dijet system. For a perfect dijet system where the two jets are back to back, $E_T^{j_1} = E_T^{j_2}$ and $\vec{p}_T^{\,j_1} = -\vec{p}_T^{\,j_2}$, which leads to $m_T = 2E_T^{j_2}$ and $\alpha_T = 0.5$. α_T is significantly larger than 0.5 when the two jets are not back to back, recoiling against $\vec{\not{p}}_T$.

In the case of events with three or more jets, one can form an equivalent dijet system by combining the jets in the event into two pseudojets. One chooses the combination such that the E_T difference (ΔH_T) between the two pseudojets is minimized. This simple clustering criterion provides good separation between QCD multijet events and events with true $\vec{\not{p}}_T$. In this case, α_T is generalized as

$$\alpha_T = \frac{1}{2}\frac{H_T - \Delta H_T}{\sqrt{H_T^2 - \not{H}_T^2}} \tag{99}$$

$$= \frac{1}{2}\frac{1 - \Delta H_T/H_T}{\sqrt{1 - (\not{H}_T/H_T)^2}}, \tag{100}$$

where $H_T = \sum_{j=1}^{N_{\text{jets}}} E_T^j$ and $\not{H}_T = |\sum_{j=1}^{N_{\text{jets}}} \vec{p}_T^{\,j}|$. Here N_{jets} is the number of jets with E_T greater than a certain threshold, typically chosen to be 50 GeV (Chatrchyan *et al.*, 2011b).

The second example is topness and Higgs-ness, for which the main idea is to use the value of χ^2 as a cut. This method becomes more powerful, especially when one can define two or more independent χ^2 values. Topness was introduced to reduce the $t\bar{t}$ background in the search for supersymmetric top quarks (Graesser and Shelton, 2013) and later further fine-tuned in the search for double Higgs production (Kim, Kim *et al.*, 2019; Kim, Kong *et al.*, 2019; Huang *et al.*, 2022). Topness basically aims to check the consistency of a given event with $t\bar{t}$ production. It is a minimized χ-squared value constructed using four on-shell constraints m_t, $m_{\bar{t}}$, m_{W^+}, and m_{W^-} and six unknowns (the three-momenta of the two neutrinos $\vec{p}_\nu$ and $\vec{p}_{\bar{\nu}}$),

$$\chi_{ij}^2 \equiv \min_{\vec{\not{p}}_T = \vec{p}_{\nu T} + \vec{p}_{\bar{\nu} T}} \left[\frac{(m_{b_i \ell^+ \nu}^2 - m_t^2)^2}{\sigma_t^4} + \frac{(m_{\ell^+ \nu}^2 - m_W^2)^2}{\sigma_W^4} + \frac{(m_{b_j \ell^- \bar{\nu}}^2 - m_t^2)^2}{\sigma_t^4} + \frac{(m_{\ell^- \bar{\nu}}^2 - m_W^2)^2}{\sigma_W^4} \right], \tag{101}$$

subject to the constraint $\vec{\not{p}}_T = \vec{p}_{\nu T} + \vec{p}_{\bar{\nu} T}$. In Eq.(101) σ_t and σ_W determine the relative weight of the on-shell conditions

and should not be less than typical resolutions. Owing to the twofold ambiguity in paring a b jet (out of b_1 and b_2) and a lepton (out of ℓ^+ and ℓ^-), we define topness as the smaller of the two possible χ-squared values χ^2_{12} and χ^2_{21}:

$$T \equiv \min(\chi^2_{12}, \chi^2_{21}). \tag{102}$$

Similarly, Higgs-ness aims to probe the consistency of a given event with double Higgs production. The challenge here is to find the sufficient number of constraints, as there are four unknowns, while there are only two intermediate on-shell particles.[7] The Higgs-ness is defined by

$$\begin{aligned} H \equiv \min\Bigg[& \frac{(m^2_{\ell^+\ell^-\nu\bar{\nu}} - m_h^2)^2}{\sigma^4_{h_\ell}} + \frac{(m^2_{\nu\bar{\nu}} - m^2_{\nu\bar{\nu},\mathrm{peak}})^2}{\sigma^4_\nu} \\ & + \min\left(\frac{(m^2_{\ell^+\nu} - m_W^2)^2}{\sigma^4_W} + \frac{(m^2_{\ell^-\bar{\nu}} - m^2_{W^*,\mathrm{peak}})^2}{\sigma^4_{W_*}}, \right. \\ & \left. \times \frac{(m^2_{\ell^-\bar{\nu}} - m_W^2)^2}{\sigma^4_W} + \frac{(m^2_{\ell^+\nu} - m^2_{W^*,\mathrm{peak}})^2}{\sigma^4_{W_*}} \right) \Bigg], \end{aligned} \tag{103}$$

where m_{W^*} is bounded from above, $m_{W^*} \le m_h - m_W$, and its location of the peak can be estimated as

$$\begin{aligned} m^{\mathrm{peak}}_{W^*} &= \frac{1}{\sqrt{3}} \sqrt{2(m_h^2 + m_W^2) - \sqrt{m_h^4 + 14 m_h^2 m_W^2 + m_W^4}} \\ &\approx 40\ \mathrm{GeV}. \end{aligned} \tag{104}$$

The $m^{\mathrm{peak}}_{\nu\bar{\nu}} = m^{\mathrm{peak}}_{\ell\ell} \approx 30$ GeV is the location of the peak in the invariant mass distribution of two neutrinos $d\sigma/dm_{\nu\bar{\nu}}$ [or $d\sigma/dm_{\ell\ell}$], which is bounded from above by $m^{\mathrm{max}}_{\nu\bar{\nu}} = m^{\mathrm{max}}_{\ell\ell} = \sqrt{m_h^2 - m_W^2}$. The phase-space distribution of $d\sigma/dm_{\nu\bar{\nu}}$ is given by

$$\frac{d\sigma}{dm_{\nu\bar{\nu}}} \propto \int dm^2_{W^*} \lambda^{1/2}(m_h^2, m_W^2, m^2_{W^*}) f(m_{\nu\bar{\nu}}), \tag{105}$$

where $\lambda(x,y,z) = x^2 + y^2 + z^2 - 2xy - 2yz - 2zx$ is the kinematic triangular function and $f(m_{\nu\bar{\nu}})$ is the invariant mass distribution of the antler topology (see also Sec. V.A) with $h \to WW^* \to \ell^+\ell^-\nu\bar{\nu}$,

$$f(m_{\nu\bar{\nu}}) \sim \begin{cases} \eta m_{\nu\bar{\nu}}, & 0 \le m_{\nu\bar{\nu}} \le e^{-\eta} E, \\ m_{\nu\bar{\nu}} \ln(E/m_{\nu\bar{\nu}}), & e^{-\eta} E \le m_{\nu\bar{\nu}} \le E, \end{cases} \tag{106}$$

where the end-point energy E and the parameter η are defined in terms of the particle masses as (Cho, Kim *et al.*, 2014)

$$E = \sqrt{m_W m_{W^*} e^\eta}, \tag{107}$$

$$\cosh\eta = \left(\frac{m_h^2 - m_W^2 - m^2_{W^*}}{2 m_W m_{W^*}} \right). \tag{108}$$

[7]See Alves and Yamaguchi (2022) for the heavy Higgs decaying to two on-shell W bosons.

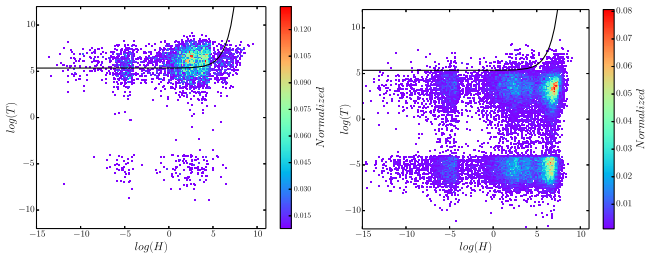

FIG. 21. Scatterplot distribution of $(\ln H, \ln T)$ for (left panel) double Higgs production (hh) and (right panel) the SM backgrounds ($t\bar{t}$, $t\bar{t}h$, $t\bar{t}V$, $\ell\ell bj$, and $\tau\tau bb$) after loose baseline selection cuts. The solid black curves in both panels are the same and represent the optimized cuts. From Kim, Kong *et al.*, 2019.

The actual peak of 30 GeV is slightly less than the result for pure phase space due to the helicity suppression in the W-ℓ-ν vertex.

The definitions of topness and Higgs-ness involve σ hyperparameters that represent experimental uncertainties and particle widths. However, in principle they can be taken as free parameters. The precise values of these parameters are not crucial, as results are not sensitive to their numerical values.

As mentioned, the χ^2 method becomes more useful when applied in more than one dimension. For example, Fig. 21 shows a scatterplot distribution of $(\ln H, \ln T)$ for double Higgs production (left panel) and the main backgrounds (right panel). The different islands observed in the figure are due to different physics processes, as well as different solutions for the neutrino momenta. The solid black curves in both panels are the same and represent the optimized cut.

The third example is ratios of energy and transverse momenta, which were recognized as useful kinematic variables early on, especially for problems in which part of the information on the kinematics is not accessible due to the production of invisible particles. The ratio of energies and p_T from cascade decays $A_2 \to A_1 a_2 \to a_1 a_0$ can provide extra information (Nojiri, Toya, and Kobayashi, 2000) on top of the "classic" invariant mass $M_{a_1 a_2}$ of the visible decay products. Indeed, by properly combining information from the transverse energy ratio $\ln E_{1,T}/E_{2,T}$ and the invariant mass $M_{a_1 a_2}$, it is possible to reconstruct the complete information on the three masses involved in the cascade decay (Cheng and Gu, 2011).

Another interesting application is for the case where the numbers of final-state invisible particles differ in the decays of pair-produced heavy resonances. For example, dark-matter "partners" charged under a Z_2 symmetry decay to a single dark-matter candidate, for instance, $A_1 \to a_1 a_0$ with A_1, a_1, and a_0 the dark-matter partner, visible particle(s), and dark-matter candidate, respectively. By contrast, those charged under a Z_3 symmetry can decay with one or two dark-matter candidates, namely, $A_1 \to a_1 a_0 a_0$ or $A_1 \to a_1 a_0$. This implies that if Z_3-charged A_1's are pair produced, each of their decays terminates with different numbers of a_0. The ratios of energy or p_T of a_1 in the two decay sides are likely to be unbalanced, whereas they are more likely to be balanced in the Z_2 case. Agashe *et al.* (2011) defined the ratio R_{p_T} as

$$R_{p_T} = \frac{\max\left(p_{T,a_1}^{(1)}, p_{T,a_1}^{(2)}\right)}{\min\left(p_{T,a_1}^{(1)}, p_{T,a_1}^{(2)}\right)}, \tag{109}$$

where $p_{T,a_1}^{(i)}$ denotes the p_T value of the visible particle in the ith decay side ($i = 1, 2$). Therefore, if the underlying physics is Z_3 (Z_2), the ratios are typically larger than (close to) 1, and thus these models can be distinguished (Agashe *et al.*, 2011).

Finally, likelihood approaches such as the maximum empirical likelihood estimator method and other matrix-element based techniques can be categorized as dimensionless variables. Although fitting the definition of dimensionless variables suitable for this section, they are separately discussed in Sec. VIII.D.

B. ISR methods

At hadron colliders, collisions of colored partons are often accompanied by mostly forward gluon jets from ISR. In this section, we discuss kinematic effects due to the presence of ISR.

We begin with a method that attempts to identify ISR. At hadron colliders, the production of heavy new particles is often accompanied by additional ISR jets with a significant transverse momentum. These extra jets make the combinatorial problem worse and complicate the reconstruction of new particle masses, especially in multijet channels like the $4j + \not{p}_T$ example used in Fig. 13 (gluino pair production followed by three-body decays). Alwall *et al.* (2009) proposed a novel technique to reduce the combinatorial background and to reconstruct a clear kinematical end point in the M_{T2} distribution. To isolate the ISR jet, they introduced $M_{T2}^{\min} = \min_{i=1,\ldots,5} M_{T2}(i)$, where $M_{T2}(i)$ is calculated from the five highest p_T jets, excluding the ith highest p_T jet. The $i_{\min}$th jet that satisfies $M_{T2}(i_{\min}) = M_{T2}^{\min}$ is tagged as the ISR jet. After all this, a strong correlation was found between the reconstructed ISR jet and the true ISR jet.

Occasionally the ISR helps in the measurement of particle masses. Gripaios (2008) considered the two-body decay of a particle at a hadron collider into a visible and an invisible particle, generalizing $W \to \ell\nu_\ell$, where the masses of the decaying particle and the invisible daughter particle are unknown. He analytically proved that the transverse mass, when maximized over all possible kinematic configurations, can be used to determine both of the unknown masses. Barr, Gripaios, and Lester (2008) generalized the idea for more complex decays of a singly produced mother particle and for pair-produced particles. On the other hand, in the absence of ISR one can in principle consider the upstream transverse momentum (UTM) playing the role of ISR, placing the system of interest under different momentum configurations (Burns *et al.*, 2009). In all cases, the mass variables (M_T, M_{T2}, and the total invariant mass) optimized over all possible momentum configurations, which are given by either ISR or UTM, exhibit a kink structure at the true values of the mother and daughter particle masses, as illustrated in Fig. 22. An application of these ISR and kink methods was illustrated by Matchev *et al.* (2010) to determine the masses of the supersymmetric chargino and sneutrino in an inclusive manner, i.e., using the two well-measured lepton momenta, while treating all other upstream objects in the event as a single entity of total transverse momentum $\not{p}_T$. This method takes full advantage of the large production rates of colored superpartners but does not rely on the poorly measured hadronic jets and avoids any jet combinatorics problems.

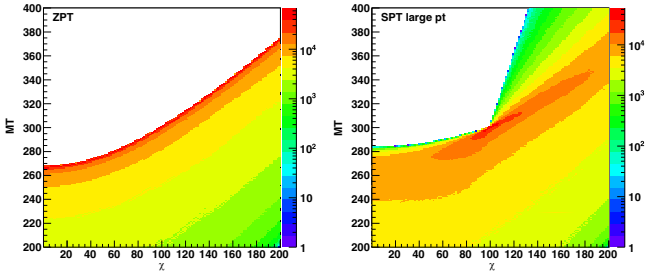

FIG. 22. The transverse mass of the mother particle decaying semi-invisibly as a function of the daughter particle mass for the phase-space Monte Carlo calculation in which the mother has been constrained to be at rest in the laboratory frame with vanishing p_T (left panel) and for the phase-space Monte Carlo calculation in which the mother can have large transverse momentum in the laboratory frame (right panel). From Barr, Gripaios, and Lester, 2008.

ISR plays a crucial role in studying dark-matter production at colliders as well. Under the hypothesis of classical weakly interacting massive particles (WIMPs), one can consider pair annihilation of dark matter (χ) into a pair of SM particles $\chi + \chi \to X_i + \bar{X}_i$, with $X_i = \ell, q, g, \ldots$. The detailed balancing equation (Low, 1958; Birkedal, Matchev, and Perelstein, 2004) relates the pair-annihilation cross section to its inverse,

$$\frac{\sigma(\chi + \chi \to X_i + \bar{X}_i)}{\sigma(X_i + \bar{X}_i \to \chi + \chi)} = 2\frac{v_X^2(2S_X + 1)^2}{v_\chi^2(2S_\chi + 1)^2}, \tag{110}$$

where v_i and S_i denote the velocity of initial-state species i and the spin number of species i, respectively, and where the cross sections are averaged over spins but not other quantum numbers such as color. The WIMP production rate can then be obtained as

$$\sigma(X_i\bar{X}_i \to 2\chi) = 2^{2(J_0-1)}\kappa_i\sigma_{\text{ann}}\frac{(2S_\chi + 1)^2}{(2S_X + 1)^2}\left(1 - \frac{4m_\chi^2}{s}\right)^{1/2+J_0}, \tag{111}$$

where the initial-state particles are assumed to be relativistic ($m_X \ll m_\chi$). Equation (111) is written in terms of a small number of parameters with a clear physical meaning: the mass m_χ and the spin S_χ of the WIMP, the value of J_0 (either 0 or 1, depending on whether the dark-matter annihilation is s-wave or p-wave annihilation), and the annihilation fraction κ_i for the given initial state. The overall scale for this prediction, the total annihilation cross section σ_{ann} is approximately given by the measured value of the cosmic dark-matter relic density. This formula is valid only at center-of-mass energies slightly above the 2χ threshold ($v = 2v_\chi = 2\sqrt{1 - 4m_\chi^2/s} \ll 1$) and receives corrections of the order of v^2. Taking $X_i = q$ or g (or

even W or Z) for a hadron collider or $X_i = e$ for an electron-positron machine, Eq. (111) provides a prediction for the WIMP production rate.

This dark-matter production process is not directly observable at colliders. At least one detectable particle is required for the event to pass the triggers and be recorded on tape. Therefore, it is desirable to consider the production of two WIMPs in association with a photon or a gluon radiated from the known initial state. We consider a simple example given by Birkedal, Matchev, and Perelstein (2004): $e^+e^- \to 2\chi + \gamma$. If the emitted photon is either soft or collinear with the incoming electron or positron, soft or collinear factorization theorems provide a model-independent relation. The emission of collinear photons is given by

$$\frac{d\sigma(e^+e^- \to 2\chi + \gamma)}{dx\, d\cos\theta} \approx \mathcal{F}(x, \cos\theta)\hat{\sigma}(e^+e^- \to 2\chi), \quad (112)$$

where $x = 2E_\gamma/\sqrt{s}$ (E_γ is the photon energy), θ is the angle between the photon direction and the direction of the incoming electron beam, $\mathcal{F}$ denotes the collinear factor

$$\mathcal{F}(x, \cos\theta) = \frac{\alpha}{\pi}\frac{1 + (1-x)^2}{x}\frac{1}{\sin^2\theta}, \quad (113)$$

and $\hat{\sigma}$ is the WIMP pair-production cross section evaluated at the reduced center-of-mass energy $\hat{s} = (1-x)s$. Note that upon integration over θ, Eq. (113) reproduces the familiar Weizsäcker-Williams distribution function. The factor $\mathcal{F}$ is universal: it does not depend on the nature of the electrically neutral particles produced in association with the photon. Combining Eqs. (111) and (112), one can easily obtain the expression for $d\sigma(e^+e^- \to 2\chi + \gamma)/dx\, d\cos\theta$. The left panel in Fig. 23 shows the comparison between the photon spectra from the process $e^+e^- \to \not{E}_T + \gamma$ in the explicit supersymmetric models (red line) and the spectra predicted by the previously mentioned procedure (Birkedal, Matchev, and Perelstein, 2004). At hadron colliders, the corresponding distributions show different shapes, as illustrated in the right panel of Fig. 23,

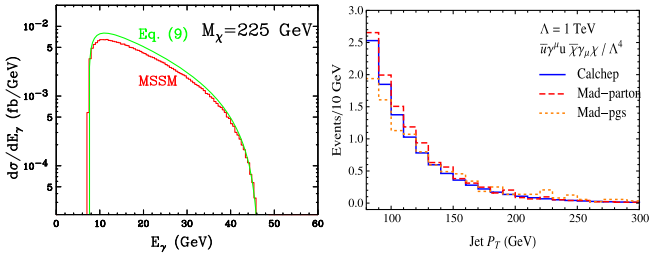

FIG. 23. Left panel: comparison between the photon spectra from the process $e^+e^- \to \not{E}_T + \gamma$ in the explicit supersymmetric models [lower (red) line] and the spectra predicted by Eq. (112) [Eq. (9) of Birkedal, Matchev, and Perelstein (2004); i.e., the upper (green) line] for a p annihilator of the corresponding mass. From Birkedal, Matchev, and Perelstein, 2004. Right panel: comparisons of simulated signal events for the $p\bar{p} \to \not{E}_T + j$ process at the Tevatron from two different Monte Carlo tools at the parton level (solid lines) and after detector simulation (dashed line). From Bai, Fox, and Harnik, 2010.

which shows the jet p_T distribution for an effective field theory leading to a monojet plus $\not{p}_T$ at the Tevatron (Bai, Fox, and Harnik, 2010).

As with the case of $\gamma + \not{E}_T$ at the LHC, one can consider dark-matter production at hadron colliders. Dark-matter particles could lead to events with the large missing transverse momentum if another visible object (such as an energetic jet) is produced at the same time. Such a monojet process has been widely studied at the Tevatron, the LHC, and future colliders (Hubisz *et al.*, 2008; Bai, Fox, and Harnik, 2010; Goodman *et al.*, 2010; Bae, Jung, and Park, 2017). The same idea has been extended to other standard model particles (such as W/Z, b/t, and h and a new particle such as Z') being produced together with dark-matter candidates. These searches are often called mono-X searches (Abercrombie *et al.*, 2020) and are one of the primary methods to look for dark-matter particles at the LHC. Figure 24 [from Tumasyan *et al.* (2021b)] shows the missing transverse momentum comparison between the data and the background prediction in the monojet (left panel) and mono-V (right panel) signal regions before and after the simultaneous fit. A similar result was given by Aad *et al.* (2021c); see Abulaiti (2022) for a summary of recent results.

ISR plays an important role in the search for new-physics models, where the mass spectrum is generate [i.e., see Martin (2007) and LeCompte and Martin (2011) for compressed supersymmetry and Cheng, Matchev, and Schmaltz (2002a, 2002b) and Freitas, Kong, and Wiegand (2018) for universal extra dimensions]. For example, when the squark ($\tilde{q}$) and the lightest neutralino ($\tilde{\chi}_1^0$) are degenerate, the pair-produced squark leads to soft decay products with little missing transverse momentum, which will be completely hidden under the QCD backgrounds. By requiring a hard ISR, one can boost the squark system with substantial p_T and improve the signal sensitivity, especially in the region of $m_{\tilde{\chi}_1^0} \approx m_{\tilde{q}}$.

Another situation where the ISR is crucial is the low-mass dijet resonance searches. The low-mass dijet resonance is completely hidden under QCD backgrounds. As with SUSY searches in the degenerate mass spectrum, one requires a hard radiation (γ, Z, j, etc.) from the initial state, which boosts the resonance to a high transverse momentum. This boosted

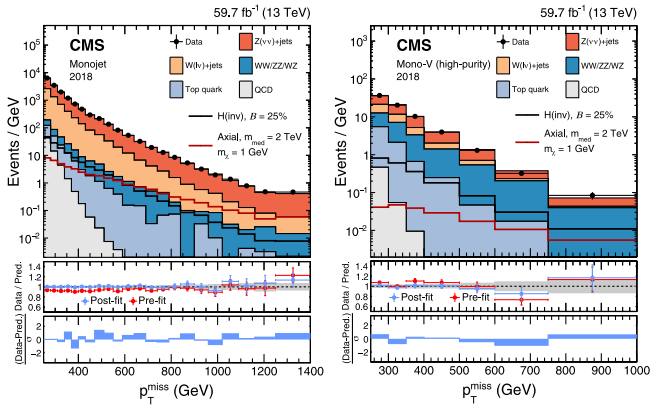

FIG. 24. Comparison between the data and the background prediction in the monojet (left panel) and mono-V (right panel) signal regions before and after the simultaneous fit. From Tumasyan *et al.*, 2021b.

resonance will appear as an unresolved fat jet. The appropriate tagging algorithm and the hard radiation can overcome the large QCD background (An, Huo, and Wang, 2013; Shimmin and Whiteson, 2016). Monojet searches can therefore be interpreted in several different ways: as dark-matter production in association with a jet, squark production in SUSY with a degenerate spectrum, or Z' production with invisible decay.

Finally, initial-state radiation is also useful in the measurement of particle properties such as top quark mass measurements at the LHC (Alioli *et al.*, 2013; Fuster *et al.*, 2017) and the International Linear Collider (Boronat *et al.*, 2020).

VIII. VARIABLES AND METHODS USING ENSEMBLES OF EVENTS

Thus far we have considered kinematic variables that can be calculated on an event-by-event basis. In this section, we introduce a variety of different types of kinematic methods that use ensembles of events. For concreteness, we consider the generic event topology in a collider analysis displayed in Fig. 25. The particles $X_i, 1 \le i \le n$ are BSM particles that appear to be promptly decaying, on-shell intermediate resonances. The particles x_i are the corresponding SM decay products, which are all visible in the detector. We begin with the so-called polynomial method (Cheng *et al.*, 2007, 2008; Cheng and Han, 2008).

A. Polynomial method

We use the experimentally measured four-momenta p_i^μ (of all SM particles) as well as the missing transverse momentum $\vec{p}_T$ in the event. We then impose the mass-shell constraints for the intermediate BSM particles X_i and attempt to solve the resulting system of equations for the eight unknown components of the four-momenta q_0^μ of the two missing particles X_0.

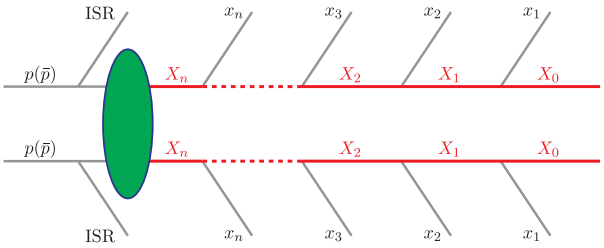

FIG. 25. The generic event topology under consideration in Sec. VIII. The particles $X_i, 1 \le i \le n$, are BSM particles that appear to be promptly decaying, on-shell intermediate resonances. The particles x_i are the corresponding SM decay products, which are all visible in the detector; i.e., we assume that there are no neutrinos among them. ISR stands for generic initial-state radiation with total transverse momentum $\vec{p}_T$. X_0 is a BSM particle that is invisible in the detector. The integer n counts the total number of intermediate BSM particles in each chain, so the total number of BSM particles in each chain is $n+1$. For simplicity, in this review we consider only symmetric events, in which the two decay chains are identical. The generalization of the methods discussed here to asymmetric decay chains is straightforward (Barr, Gripaios, and Lester, 2009; Konar *et al.*, 2010a). From Burns *et al.*, 2009.

With the $n+1$ unknown BSM masses m_i for X_i, the number of unknown parameters N_p is given by

$$N_p = 8 + (n+1) = n + 9. \tag{114}$$

The number of measurements (constraints) N_m includes the two components of the missing transverse momentum condition and $2(n+1)$ mass-shell conditions (for each BSM particle X_i belonging to one of the two decay chains shown in Fig. 25),

$$N_m = 2(n+1) + 2 = 2n + 4. \tag{115}$$

The number of undetermined parameters for any given event is then readily obtained from Eqs. (114) and (115) as

$$N_p - N_m = 5 - n. \tag{116}$$

Therefore, if $n \ge 5$, one can in principle solve for the momenta of the invisible particles and reconstruct the entire final state (up to the combinatorial issue mentioned in Sec. II.B).

However, one might do better than this by combining the information from two or more events (Nojiri, Polesello, and Tovey, 2003; Kawagoe, Nojiri, and Polesello, 2005; Cheng *et al.*, 2008, 2009). For example, consider another event of the same type. Since the $n+1$ unknown masses were already counted in Eq. (114), the second event introduces only eight new parameters (the four-momenta of the two X_0 particles in the second event), bringing the total number of unknowns in the two events to

$$N_p = 8 + 8 + (n+1) = n + 17. \tag{117}$$

At the same time, all the constraints are still valid for the second event, which results in $2n+4$ additional constraints. This brings the total number of constraints to

$$N_m = (2n+4) + (2n+4) = 4n + 8. \tag{118}$$

Subtracting Eq. (117) from Eq. (118), we get

$$N_p - N_m = 9 - 3n. \tag{119}$$

Comparing the previous result [Eq. (116)] with Eq. (119), we see that the latter decreases much faster with n. Therefore, when using the polynomial method, combining information from two different events is beneficial for large n (in this example, for $n \ge 3$).

Following the same logic, one can generalize this parameter counting to the case where the polynomial method is applied for a group of N_{eve} different events of the same type at a time. The number of unknown parameters is

$$N_p = n + 1 + 8N_{\text{eve}}, \tag{120}$$

the number of constraints is

$$N_m = (2n+4)N_{\text{eve}}, \tag{121}$$

and therefore the number of undetermined parameters is given by

$$N_p - N_m = n + 1 - 2(n-2)N_{\text{eve}}. \tag{122}$$

For $N_{\text{eve}} = 1$ and 2 Eq. (122) reduces to Eqs. (116) and (119), respectively. What is the optimal number of events N_{eve} for the polynomial method? The answer can be readily obtained from Eq. (122), where N_{eve} enters the last term on the right-hand side. If this term is negative, increasing N_{eve} would decrease the number of undetermined parameters, and therefore it would be beneficial to combine information from more and more different events. From Eq. (122) we see that this would be the case if the decay chain is sufficiently long, i.e., $n \geq 3$. On the other hand, when $n = 1$, considering more than one event at a time is actually detrimental: we are adding more unknowns than constraints. In the case of $n = 2$, the number of undetermined parameters $N_p - N_m$ is actually independent of N_{eve}, and one might as well consider the simplest case of $N_{\text{eve}} = 1$.

Figure 26 summarizes the dependence of the number of undetermined parameters $N_p - N_m$ as a function of the number n of intermediate heavy resonances in the decay chains of Fig. 25 for various mass determination approaches: the M_{T2} method (green open squares), the end-point method (red open circles), the polynomial method for $N_{\text{eve}} = 2$ (blue, multiplication signs), and a hybrid method that combines the last two methods (magenta circled multiplication signs) (Burns *et al.*, 2009). Within the yellow-shaded region the number of unknowns N_p does not exceed the number of measurements N_m for the corresponding method, and the mass spectrum can be completely determined. Readers

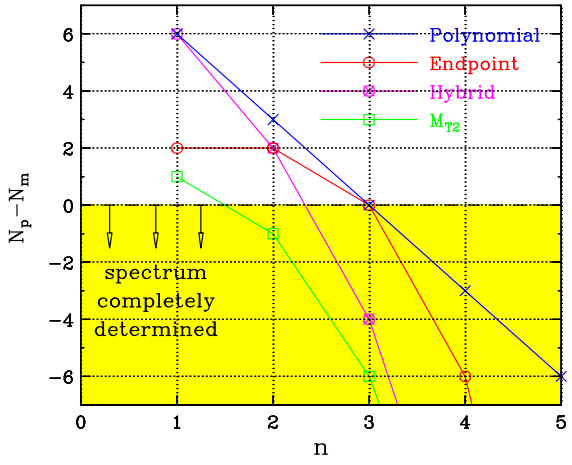

FIG. 26. Dependence of the number of undetermined parameters $N_p - N_m$ as a function of the number n of intermediate heavy resonances in the decay chains of Fig. 25 for various mass determination approaches: the M_{T2} method (green open squares), the end-point method (red open circles), the polynomial method for $N_{\text{eve}} = 2$ (blue multiplication signs), and a hybrid method that combines the last two methods (magenta circled multiplication signs). Within the yellow-shaded region the number of unknowns N_p does not exceed the number of measurements N_m for the corresponding method and the mass spectrum can be completely determined. From Burns *et al.*, 2009.

interested in counting the number of undetermined parameters of various methods can refer to Burns *et al.* (2009) for more details, including a hybrid method combining the techniques of the polynomial and end-point methods (Nojiri, Polesello, and Tovey, 2008). A similar idea regarding the mass determination in sequential particle decay chains was discussed by Webber (2009).

The polynomial method described in this section relies on the presence of a sufficient number of kinematic constraints such that the event kinematics becomes exactly solvable for the components of the invisible momenta. This typically requires complex event topologies, with several successive decays in each decay chain. Therefore, the method cannot be applied to simpler event topologies with fewer kinematics constraints, and new ideas are needed. Some of those alternative techniques are described in Secs. VIII.B–VIII.F.

B. Focus-point method

The focus-point method for mass measurement proposed by Kim, Matchev, and Shyamsundar (2019) and Matchev and Shyamsundar (2020) can be applied to certain event topologies with underconstrained kinematics. The method relies on the fact that the projection onto the visible space will result in a relatively large number of events in the vicinity of a singularity, as illustrated in Fig. 18. Turning the argument around, one could ask, for any given event, which choice of the unknown mass parameters would place a singularity at that point. This condition delineates a hypersurface in mass-parameter space, and we have one such "extreme" surface for each event in the data. As shown by Kim, Matchev, and Shyamsundar (2019), the extreme surfaces for many of the events in the dataset pass close to the true values of the unknown masses. This leads to a technique for estimating the unknown masses simply as the focus point of the extreme surfaces in the mass-parameter space. This is illustrated in Fig. 27 for the $t\bar{t}$-like topology of Fig. 11(b) (two-step two-body decays $A_2 \to a_2 A_1$ and $A_1 \to a_1 a_0$). The masses are chosen as $m_{A_2} = 1000$ GeV, $m_{A_1} = 800$ GeV, and $m_{a_0} = 700$ GeV. The left panel in Fig. 27 shows the kinematic boundaries of 100 events in the trial mass-parameter space $(\tilde{m}_{A_1}, \tilde{m}_{A_2})$, with $\tilde{m}_{a_0}$ fixed to its true value $m_{a_0} = 700$ GeV. Notice that the kinematic boundaries tend to focus on the true values of the masses of the parent particles A_2 and A_1 in this example. The right panel in Fig. 27 shows a heat map of the density of extreme surfaces (curves in this case) per 10×10 GeV bin. The bright spot in the figure marks the true values of the masses. This technique can be readily generalized from $t\bar{t}$ events to more general event topologies in SUSY and beyond (Kim, Matchev, and Shyamsundar, 2019).

C. Kinematic end-point methods

As discussed, the distributions of kinematic variables often allow us to infer the mass values of the new particles involved in the physics process of interest. For example, the end points of invariant mass, transverse mass, M_{T2}, and M_2 variables and energy peaks are determined purely by kinematics, regardless of detailed dynamics; see also Sec. V. Therefore, those observables have received much attention and a host of ideas have been proposed, especially in the context of mass

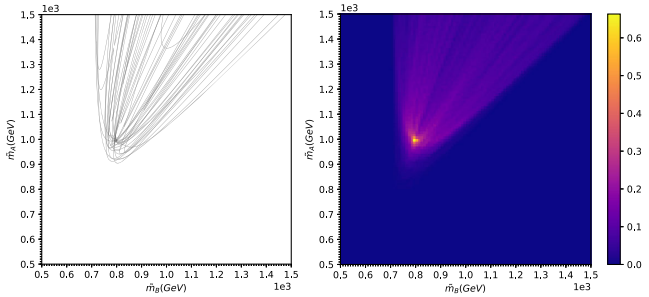

FIG. 27. Left panel: plot of 20 extreme curves in the $(\tilde{m}_{A_1}, \tilde{m}_{A_2})$ plane for a fixed $\tilde{m}_{a_0} = m_{a_0} = 700$ GeV for the $t\bar{t}$-like topology of Fig. 11. Right panel: the fractional density of extreme curves, i.e., the fraction of events whose extreme curves pass through a given 10×10 GeV pixel. From Kim, Matchev, and Shyamsundar, 2019.

measurements of new particles since they do not require any prior knowledge about the exact details of the associated new physics.

The classic supersymmetric "$q\ell\ell$ chain" introduced in Sec. V.A is one of the most extensively studied benchmark processes in this area (Allanach *et al.*, 2000; Lester, 2001; Gjelsten, Miller, and Osland, 2004, 2005b; Miller, Osland, and Raklev, 2006; Burns, Matchev, and Park, 2009; Costanzo and Tovey, 2009; Matchev *et al.*, 2009; Kim, Matchev, and Park, 2016; Matchev, Moortgat, and Pape, 2019). There are up to four unknown mass parameters, namely, $m_{\tilde{q}}$, $m_{\tilde{\chi}_2^0}$, $m_{\tilde{\ell}}$, and $m_{\tilde{\chi}_1^0}$, and four kinematic end points are readily available, for instance, $M_{q\ell_n}^{\max}$, $M_{q\ell_f}^{\max}$, $M_{\ell\ell}^{\max}$, and $M_{q\ell\ell}^{\max}$. To avoid the combinatorial ambiguity between ℓ_n and ℓ_f, one instead uses the set $M_{q\ell}^{<,\max}$, $M_{q\ell}^{>,\max}$, $M_{\ell\ell}^{\max}$, and $M_{q\ell\ell}^{\max}$; see Sec. V.A. Therefore, in principle all of the unknown mass parameters can be completely determined by inverting the four end-point measurements. However, this mass determination can sometimes be ambiguous or underconstrained, and several degenerate solutions for the masses may arise (Gjelsten, Miller, and Osland, 2004, 2005a; Arkani-Hamed *et al.*, 2006; Gjelsten *et al.*, 2006; Costanzo and Tovey, 2009).

There are several reasons for these challenges in the mass determination. First, depending on the underlying mass spectrum, the four observables may not be completely independent; in certain regions of parameter space, the following relation holds (Gjelsten, Miller, and Osland, 2004):

$$(M_{q\ell\ell}^{\max})^2 = (M_{q\ell}^{>,\max})^2 + (M_{\ell\ell}^{\max})^2. \tag{123}$$

In this case another independent measurement is needed, and one such example is the lower kinematic end point $M_{q\ell\ell,\text{const}}^{\min}$ (Allanach *et al.*, 2000). Here the constrained variable $M_{q\ell\ell,\text{const}}$ is the usual $M_{q\ell\ell}$ subject to the condition $M_{\ell\ell}^{\max}/\sqrt{2} < M_{\ell\ell} < M_{\ell\ell}^{\max}$, which forces one to choose events where the opening angle between the two leptons is greater than $\pi/2$ in the rest frame of $\tilde{\ell}$. Second, the finite detector resolution smears each of the measured end-point values away from the theoretically predicted ones, resulting in multiple and/or unphysical solutions (Gjelsten, Miller, and Osland, 2004; Gjelsten, Miller, and Osland, 2005a, 2005b). Similarly, if an end point is identified as the long tail of the associated distribution, its measurement is highly sensitive to the data statistics and "false" solutions can emerge. However, even in the ideal case of a perfect experiment, it is possible that different mass spectra can result in the same set of end points such that an application of relevant inversion formulas [see Burns, Matchev, and Park (2009) for the full sets of formulas] would yield "fake" solutions. A possible way to resolve this ambiguity would be to study the shapes of the boundaries of the bivariate distributions in $\{M_{q\ell}^{<}, M_{q\ell}^{>}\}$ and $\{M_{\ell\ell}, M_{q\ell\ell}\}$ (Burns, Matchev, and Park, 2009).

The previous discussion requires one sufficiently long decay chain to determine the full mass spectrum. However, for the event topologies involving pair-produced heavy resonances, the mass determination can often be done in combination with transverse variables such as M_{T2}. A well-studied prototypical example is the fully leptonic SM $t\bar{t}$ production. The $b\ell$ invariant mass end point encodes the mass relation

$$M_{b\ell}^{\max} = \frac{1}{m_W}\sqrt{(m_t^2 - m_W^2)(m_W^2 - m_\nu^2)} \tag{124}$$

and the two combinatorics-free subsystems, leptonic and bottom, respectively, when applied to M_{T2} or $M_{T2,\perp}$, allow one to extract two independent mass relations $\mu^{(\ell\ell)}$ and $\mu^{(bb)}$, respectively [see Eq. (65)], as

$$\mu^{(\ell\ell)} = \frac{m_W}{2}\left(1 - \frac{m_\nu^2}{m_W^2}\right), \tag{125}$$

$$\mu^{(bb)} = \frac{m_t}{2}\left(1 - \frac{m_W^2}{m_t^2}\right). \tag{126}$$

The CMS Collaboration performed the top quark mass measurement using this idea at $\sqrt{s} = 7$ (CMS Collaboration, 2012; Chatrchyan *et al.*, 2013a) and 8 TeV (CMS Collaboration, 2016) and achieved an ∼2-GeV-level and a $\lesssim$1-GeV-level systematics in the respective measurements by constraining the W and ν masses from other independent measurements.

In a similar fashion, the three mass parameters appearing in the two-step, two-body cascade decay topology shown in Fig. 7(a) can be determined in combination with the peak values in the a_2 and a_1 energy distributions if both A_2 and A_1 are either scalar or unpolarized. Again the kinematic end point in the $M_{a_2a_1}$ distribution is

$$M_{a_2a_1}^{\max} = \frac{1}{m_{A_1}}\sqrt{(m_{A_2}^2 - m_{A_1}^2)(m_{A_1}^2 - m_{a_0}^2)}, \tag{127}$$

and the two energy-peak values are given by

$$E_{a_2}^{\text{peak}} = \frac{m_{A_2}^2 - m_{A_1}^2}{2m_{A_2}}, \tag{128}$$

$$E_{a_1}^{\text{peak}} = \frac{m_{A_1}^2 - m_{a_0}^2}{2m_{A_1}}. \tag{129}$$

The last three mass relations are completely independent, allowing one to determine the three mass parameters. The generic idea was first proposed by Agashe, Franceschini, and Kim (2014) and applied to a supersymmetric gluino decay process $\tilde{g} \to b\tilde{b}, \tilde{b} \to b\tilde{\chi}_1^0$, with combinatorial ambiguity in the b-jet energy distribution appropriately prescribed.

Finally, we close this section by mentioning an alternative method for identifying kinematic end points in the data whereby one inspects the momentum configurations of the visible particles in each event in order to tag the events that give the kinematic end point. Consider the decay of a heavy resonance directly to $N \geq 2$ massless visible particles and possibly a set of invisible particles. Owing to Lorentz symmetry, invariant mass variables can be studied in any convenient frame, for instance, the parent rest frame. The upper kinematic end points of the ranked (i.e., ordered) two-body invariant masses are obtained for certain special momentum configurations of the visible particles; see Fig. 28 for a few representative examples. If a resonance decays to its final-state particles via on-shell intermediary states, it is often convenient to find extreme configurations in the rest frame of the intermediary states, as described in Sec. V.A. See Kim, Matchev, and Park (2016) for a more systematic discussion about the kinematic end points of invariant mass variables, including ordered invariant masses.

For transverse mass variables including M_{T2}, it is convenient to find the kinematic end point again in the rest frame of the resonance(s). For a pair of identical resonances, in the absence of ISR the back-to-back boost invariance in the transverse plane allows one to move to the frame where both resonances are produced at rest (Cho *et al.*, 2008b). Thus, the typical extreme geometric configurations are those where the final-state particles move only on the transverse plane (Cho *et al.*, 2008a, 2008b; Matchev *et al.*, 2010; Matchev, Moortgat, and Pape, 2019). In the presence of ISR, the existence of a special direction in the transverse plane leads to several competing momentum configurations, which is the physics origin of the kink in the M_{T2} end-point function (Matchev *et al.*, 2010).

D. Matrix-element and likelihood methods

The matrix-element method (MEM) is one of the likelihood methods that utilizes the quantum amplitude of a process. The probability of observing visible particles $\{p_i^{\text{vis}}\}, i = 1, \ldots, N_{\text{vis}}$, under the assumed process and parameters $\{\alpha\}$ for a single event is given by

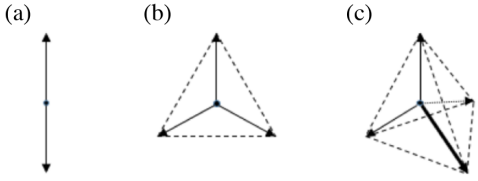

FIG. 28. Examples of extreme momentum configurations of the visible decay products of a resonance: (a) pencil-like, (b) equilateral trianglelike, and (c) pyramidlike.

$$\begin{aligned}\mathcal{P}(\{p_i^{\text{vis}}\}|\alpha) &= \frac{1}{\sigma_\alpha}\left[\prod_{i=1}^{N_{\text{vis}}}\int\frac{d^3p_i}{(2\pi)^3 2E_i}\right]W(\{p_i^{\text{vis}}\},\{p_i\}) \\ &\times\left[\prod_{j=1}^{N_{\text{inv}}}\int\frac{d^3q_j}{(2\pi)^3 2E_j}\right]\sum_{a,b}\frac{f_a(x_1)f_b(x_2)}{2sx_1x_2}|\mathcal{M}_\alpha(\{p_i\},\{q_j\})|^2 \\ &\times(2\pi)^4\delta^4\left[p_a+p_b-\left(\sum_i p_i+\sum_j q_j^{\text{inv}}\right)\right],\end{aligned} \tag{130}$$

where $\{p_a, p_b\}$ are the four-momenta of the initial-state partons a and b and $\{f_a, f_b\}$ are their corresponding PDFs. Here one integrates out the unknown momenta $\{q_j\}$ of invisible particles $j = 1, \ldots, N_{\text{inv}}$ and considers various nonpartonic effects, including detector response and QCD activity with a transfer function $W(\{p_i^{\text{vis}}\},\{p_i\})$ between the parton-level momentum $\{p_i\}$ and the reconstructed momentum $\{p_i^{\text{vis}}\}$. Integrating the transfer functions often takes up most of the computing resources for a MEM analysis. In the case where the visible particles consist only of light leptons (electron and muon), we can neglect the transfer functions, which leads to an important simplification for purely leptonic channels like Higgs decays to four leptons (Gao *et al.*, 2010; Bolognesi *et al.*, 2012; Avery *et al.*, 2013). We can construct the likelihood specific to $\{\alpha\}$ and $\mathcal{L}_\alpha$ for a set of N events with individual likelihoods for each event n as

$$\mathcal{L}_\alpha \equiv \prod_n^N \mathcal{P}(\{p_i^{\text{vis}}\}_n|\alpha). \tag{131}$$

Thus, one can expect to find the model parameters $\{\alpha\}$ by maximizing $\mathcal{L}_\alpha$. By constructing a likelihood function, one can measure not only particle properties such as the mass and width of new particles but also coupling structures in the interaction vertices, as demonstrated by Betancur *et al.* (2019). One can also use the matrix element to define eventwise kinematic variables, which can be particularly useful in precision studies to probe interference contributions where new physics is most likely to be first seen (Gainer *et al.*, 2018; Gritsan *et al.*, 2020).

E. Edge detection

The identification of kinematic end points in a certain one-dimensional distribution is often indicative of boundaries in the high-dimensional phase space that is being projected onto the one-dimensional subspace; see Fig. 18. At the same time, such kinematic end points can also be formed through signal events piling up on top of a smooth background distribution, and thus can be used for discovery (Debnath, Gainer, Kim, and Matchev, 2016).

The traditional end-point techniques [usually in the context of supersymmetry; see Matchev, Moortgat, and Pape (2019) for a review] were typically applied to one-dimensional histograms, but that does not necessarily have to be the case; while dimensional reduction increases the statistics near the kinematic end point, it may also result in the loss of useful information. This is why some work advocated for edge detection in a two-dimensional space of observables

(Huang, Kersting, and Yang, 2008; Karapostoli, 2008; Burns, Matchev, and Park, 2009; Costanzo and Tovey, 2009) or even for a surface boundary detection in three or more dimensions (Agrawal *et al.*, 2014; Altunkaynak, Kilic, and Klimek, 2017; Debnath, Gainer *et al.*, 2017). Such approaches better utilize the higher-dimensional information contained in the full phase-space distribution of events; see Fig. 18.

The traditional approach to edge detection is to bin the data in a lower-dimensional observable space and identify a kinematic edge by comparing the counts in adjacent bins, looking for a significant variation (Agashe *et al.*, 2011; Curtin, 2012). Conventional edge-detection algorithms for machine vision have been developed mostly for two-dimensional image data and are not necessarily aligned with the goals of particle physics analyses, which need to account for smearing of the edges due to detector resolution, particle widths, etc.

When it comes to detecting kinematic features in the data, an alternative approach to binning is offered by the *tessellation* of the data, where we can treat the full set of collider events as a point pattern in the observable multidimensional kinematic space. There exist different tessellation methods. For example, Debnath, Gainer, Kim, and Matchev (2016) proposed a phase-space edge-detection method based on the *Voronoi* tessellation, which divides the original space into nonoverlapping regions (Voronoi cells) such that the points within each region are closest to one of the original data points (Okabe, Boots, and Sugihara, 1992). It was shown that the value of the scaled standard deviation

$$\frac{\sigma_a}{\bar{a}} = \frac{1}{\bar{a}} \sqrt{\sum_{n \in N_i} \frac{(a_n - \bar{a})^2}{|N_i| - 1}}, \tag{132}$$

where N_i is the set of neighbors of the ith Voronoi cell and $\bar{a}(N_i)$ is their mean area, is indicative of whether the ith cell is close to a boundary. This result can be easily understood intuitively by noting that for boundary cells the neighbors on the dense side have small areas, while the neighbors on the sparse side have large areas. Therefore, edge cells are expected to show relatively large scaled standard deviations. The method was subsequently tested on the classic supersymmetric $q\ell\ell$ chain, $\tilde{q} \to \tilde{\chi}_2^0 j, \tilde{\chi}_2^0 \to \tilde{\ell}^{\pm} \ell^{\mp}$, and $\tilde{\ell}^{\pm} \to \tilde{\chi}_1^0 \ell^{\pm}$: Debnath, Gainer, Kim, and Matchev (2016) considered edge detection in the two-dimensional space $\{m^2_{\ell\ell}, (m^2_{j\ell\ell} - m^2_{\ell\ell})/6\}$, while Debnath, Gainer, Kilic *et al.* (2016) demonstrated a surface boundary detection in the three-dimensional space $\{m^2_{j\ell_n}, m^2_{\ell\ell}, m^2_{j\ell_f}\}$. The method can also be adapted to mass measurements of new particles (Debnath, Gainer *et al.*, 2017), and for enhancing the discovery opportunities in combination with the Δ_4 variable (Debnath *et al.*, 2019).

The Delaunay triangulation is a tessellation that is the dual graph of a Voronoi tessellation. Therefore, Matchev, Roman, and Shyamsundar (2020) proposed an alternative edge-detection method that utilizes the Delaunay tessellation of the data instead. Since edge detection necessarily involves computing the gradient of the phase-space density, the Delaunay cells, as they are formed of several neighboring data points, are the natural objects for computing local gradients.

F. Interference effects

When high precision is required in measurements of masses or other kinematic properties, subtle quantum effects can modify the theoretical predictions in ways that can be hard to predict or to interpret without a full theoretical understanding of kinematic variables.

Even relatively simple observables like the invariant mass can be affected by subtle effects that may give apparently inconsistent results between measurements of the mass of a particle in two different channels. This is the case for the Higgs boson, whose most precise mass measurements are in the $\gamma\gamma$ and 4ℓ channels. The key difference between these two channels is that the 4ℓ channel is essentially free from background, whereas the $\gamma\gamma$ channel has substantial background from QED + QCD production of two photons. The presence of large background opens the possibility of having nonresonant features to redefine the expected signal shape even for perfect detectors. Dixon and Stewart Siu (2003), Martin (2012, 2013), de Florian *et al.* (2013), Coradeschi *et al.* (2015), and Cieri *et al.* (2017) pointed out that the $\gamma\gamma$ peak in the $M_{\gamma\gamma}$ distribution is expected to be shifted and broadened by the interference between $gg \to \gamma\gamma$ and $gg \to h \to \gamma\gamma$. Therefore, the mass measured as the peak of the $M_{\gamma\gamma}$ distribution will differ from that measured in background-free channels such as 4ℓ. The subtraction of the peak from 4ℓ events into the extraction of the peak in the $M_{\gamma\gamma}$ distribution may help to highlight this effect in a model-independent way. As the effect has to do with the Higgs boson width, it has also been pointed out that the mass shift can be used to constrain the Higgs boson width (Dixon and Li, 2013; Campbell *et al.*, 2017).

The shift also depends on experimental conditions such as the diphoton mass resolution. Depending on how the measurement in the $\gamma\gamma$ channel is performed, the shift may range from a fraction of 100 MeV to a fraction of 1 GeV, which would be sufficiently large to be observed (Martin, 2012). The ATLAS Collaboration has evaluated the impact of this theoretical effect on a realistic mass measurement and has found a nonvanishing effect around 35 MeV for the specific procedure used to extract the Higgs boson mass in the $\gamma\gamma$ channel (ATLAS Collaboration, 2016).

The present Higgs boson mass appearing in the up-to-date Particle Data Group report is 125.25 ± 0.17 (Zyla *et al.*, 2020), stemming from slightly disagreeing measurements from CMS (Sirunyan *et al.*, 2020a) $m_h^{\gamma\gamma} = 125.78 \pm 0.26$ GeV, $m_h^{4\ell} = 125.46 \pm 0.16$ GeV, and ATLAS (Aaboud *et al.*, 2018d) $m_h^{4\ell} = 124.79 \pm 0.37$ GeV, $m_h^{\gamma\gamma} = 124.93 \pm 0.40$ GeV. Future HL-LHC measurements, exploiting a dataset about 2 orders of magnitude larger, could reach a measurement with a much smaller uncertainty than the present one. Systematic uncertainties will be relevant for such a large dataset, but a purely statistical rescaling of the present measurement would hint at the necessity of taking into account these subtle effects from interference. For example, Cepeda *et al.* (2019) foresaw a precision on m_h in the $\gamma\gamma$

channel of around 10–20 MeV (CMS Collaboration, 2022a, 2022b), thus calling for a careful evaluation of the interference effects.

IX. KINEMATIC VARIABLES IN THE MACHINE-LEARNING ERA

Recently there has been an explosion of studies employing ML for various tasks in the analysis of high-energy data. A collection of references is maintained at HEPML Living Review (Feickert and Nachman, 2021). Thus far we have discussed traditional (i.e., non-ML) analysis techniques using kinematic variables [Fig. 29(a)]. Here we discuss the multifaceted synergy between ML and kinematic variables in particle physics.

A. Feature engineering

Feature engineering for ML.—Kinematic variables are often used as input event features in ML approaches. While in principle one can train machines using only raw or low-level data as inputs [Fig. 29(b)], the dimensionality of such feature vectors will typically be large. When we feed low-level data, the machine could expend a lot of resources trying to extract useful information from it. Furthermore, inaccuracies in the simulation models could lead to unknown and unquantified errors in the high-dimensional low-level simulated data, which could lead to unquantified errors in the subsequent ML-based analysis. Both these issues can be ameliorated using reconstructed objects and/or human-engineered high-level variables as inputs in ML applications [Fig. 29(c)]. Optionally, one can also pass the low-level information to the machine, in addition to the high-level features. Carefully chosen high-level input features can efficiently retain the information from low-level data that is relevant to the task at hand and can facilitate efficient training of ML approaches. Furthermore, reducing the dimensionality of the input allows for easier and more meaningful validation of the simulation models (in the low-dimensional input space) for the purposes of the analysis at hand.

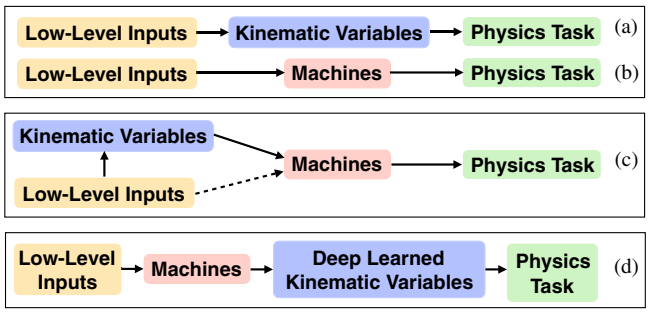

FIG. 29. Various possible analysis chains for some physics-motivated task. (a) The traditional (non-ML) analysis technique using kinematic variables. (b) ML-based analysis using only raw or low-level data as inputs. (c) ML-based analysis using in addition reconstructed objects and/or human-engineered high-level variables as inputs. (d) Construction of sensitive analysis variables using machine-learning techniques.

Feature engineering with ML.—An interesting development in the last few years is the construction of sensitive analysis variables using machine-learning techniques [Fig. 29(d)]. Any ML approach, in which a machine (such as a neural network or boosted decision tree) takes individual events as input and returns an output, can be thought of as constructing an analysis variable or observable. However, discussing all such applications of machine learning, including classifiers (Guest, Cranmer, and Whiteson, 2018) and likelihood ratio estimators (Cranmer, Pavez, and Louppe, 2015), is beyond the scope of this review. Instead, we focus on ML approaches for constructing event observables, which are functionally similar to more traditional event observables.

At an abstract level, many ML approaches for constructing collider observables share the following basic procedure. (1) Construct a trainable, machine-learning-based function that maps a high-dimensional event description to a low-dimensional observable. (2) Construct an evaluation metric to quantify the performance of the ML-based observable for a task at hand. (3) Train the ML-based observable by optimizing the evaluation metric. Several novel ML-based observables have been proposed in recent years, with all of them differing in the implementation details of the previously listed steps (Datta, Larkoski, and Nachman, 2019; Kim *et al.*, 2023).

For example, Datta, Larkoski, and Nachman (2019) constructed jet observables as products of powers of N-subjettiness variables with unknown (trainable) exponents. The performance of the observable for distinguishing between different signatures ($H \to bb$ vs $g \to bb$; Z' vs quarks and gluons) is used as the performance metric to be minimized in order to choose the exponents in the observable.

Kim *et al.* (2023) constructed kinematic variables for different event topologies as neural-network-based functions of reconstructed parton-level data. The variables are trained by maximizing the sensitivity of their distributions to the value of underlying parameters in the corresponding event topologies, as captured by the mutual information between the parameters and the variable. Variables trained using such an approach are sensitive over a range of unknown theory parameter values and can subsequently be used for signal discovery or parameter measurement analyses involving the concerned topology.

B. Domain-inspired machine learning

Several neural network architectures inspired by high-energy physics (HEP) have been invented for use in ML for HEP. For example, energy flow networks and particle flow networks (Komiske, Metodiev, and Thaler, 2019), which are based on deep sets (Zaheer *et al.*, 2017) and energy flow polynomials (Komiske, Metodiev, and Thaler, 2018), are neural network architectures designed for learning from collider events represented as unordered, variable-length sets of particles. As another example, Lorentz boost networks (LBN) (Erdmann *et al.*, 2019; Idaszek, 2019; Jung, 2019) allow for the construction of composite particles and rest frames (both represented by combinations of particles) within the trainable layers of the network, using four-momenta of the final-state particles as input. The LBNs also Lorentz boost the composite particles into the constructed rest frames. The features thus constructed within the layers of the network can

then be used to perform relevant physics tasks like classification or regression. Such domain-specific network architectures have been observed to outperform other domain-unspecific neural network architectures for collider event classification tasks (Erdmann *et al.*, 2019). Furthermore, they also allow for interpretation of the intermediate layers of the trained neural network.

C. Interpretability and explainability

Most machine-learning approaches, including neural networks and boosted decision trees, act as black-box systems with varying degrees of "black-box-ness," depending on their architecture. This poses a challenge to the trustworthiness of ML-based analyses. This problem can be approached from three directions. The first approach is to interpret and explain the ML black box. The second approach is to try and make the machine less of a black box. The third approach is to design ML-based analyses techniques that are robust despite the black-box nature of the machine. Kinematic variables can play a role in each of these approaches. For example, one can use kinematic variables to interpret and explain the decisions made by the machine-learning algorithms (Chang, Cohen, and Ostdiek, 2018; Agarwal *et al.*, 2021; Faucett, Thaler, and Whiteson, 2021; Grojean, Paul, and Qian, 2021). Using kinematic-variable-inspired neural network architectures like energy flow and particle flow networks (Komiske, Metodiev, and Thaler, 2019) and Lorentz boost networks (Erdmann *et al.*, 2019; Idaszek, 2019; Jung, 2019) can reduce the black-box nature of neural networks. Finally, using machine learning to construct *low-dimensional event* observables that are not tuned to specific study points (i.e., are sensitive to the underlying physics over a range of unknown model parameters) (Kim *et al.*, 2023), akin to kinematic variables, allows for meaningful control-region validation of the simulations, which in turn leads to robust analysis techniques.

D. Advantage of quantum computation for identifying event topologies

To date most kinematic analyses have been based on an assumed event topology that makes it possible to optimize a kinematic variable in each case. Owing to the complicated structure of phase space and the limited information from invisible particles, various machine-learning algorithms become useful, but their training data are also generated only for particular event topologies.

Given the lack of any clear signal of new physics so far at the LHC, we need to ask how one can perform an optimized analysis without any assumptions on the new-physics model.

TABLE II. The number of inequivalent event topologies as a function of $1 \leq N_v \leq 4$ and $1 \leq N_\chi \leq 5$. From Cho, Kim *et al.*, 2014.

	N_χ				
N_v	1	2	3	4	5
1	1	2	4	8	16
2	2	7	20	55	142
3	4	20	78	270	860
4	8	55	270	1138	4294

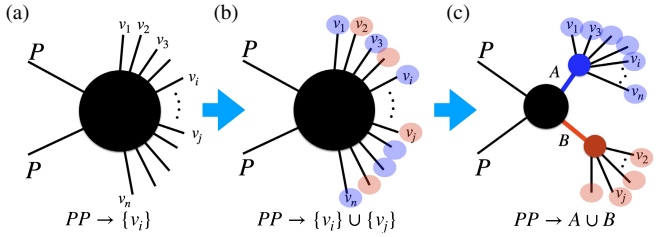

FIG. 30. (a) n-observed particles. (b) Divsion of n particles into two groups for a $2 \to 2$ process. (c) Identified event topology with A and B. From Kim *et al.*, 2021.

This question is related to identifying the event topology of the signal from data alone. Checking all possible event topologies can be a time-consuming task. For example, the number of possible event topologies with $N_v = 5$ visible particles and $1 \leq N_\chi \leq 4$ assumed invisible particles is $\mathcal{O}(5000)$, as shown in Table II (Cho, Kim *et al.*, 2014). As the number of visible and invisible particles increases, the number of possible event topologies grows exponentially, making the problem of identifying the event topology at least as hard as any nondeterministic polynomial time problem. Since it is in the category of combinatorial optimization problems, where various quantum algorithms have been introduced (Farhi, Goldstone, and Gutmann, 2014; Djidjev *et al.*, 2018) and shown to be successful, this suggests that quantum computers be used for this task.

When the produced particles are boosted, their decay products are organized into groups exhibiting characteristic structures and substructures. One can then utilize a shape variable used in clustering a jet with either a gate-type quantum computer or a quantum annealer (Wei *et al.*, 2020; Pires *et al.*, 2021; Delgado and Thaler, 2022; Pires, Omar, and Seixas, 2023). Unlike QCD jet activity, the phase space of a hard process can exhibit a more complicated structure, in which case one can try to minimize some basic kinematic quantity, such as the total invariant mass or sum or difference of invariant masses of the clusters. If one restricts to a $2 \to 2$ process, one can directly use a quadratic unconstrained binary optimization with an Ising model to partition the reconstructed objects as in Fig. 30, showing improved performance with respect to the standard hemisphere algorithm (Kim *et al.*, 2021). Once we identify the event topology, we can proceed to optimize the analysis to measure the masses and spins of the new particles as usual.

X. KINEMATIC VARIABLES IN DIFFERENT EXPERIMENTS

While most of the recent developments in kinematic variables have been motivated by the phenomenology in collider experiments, especially hadron colliders, they are readily applicable to other experiments, including accelerator-based experiments (such as fixed-target-type or beam-dump-type neutrino experiments), reactor-based neutrino experiments, dark-matter (in)direct detection experiments, and cosmic-particle telescopes. Here we review the existing usage of kinematic variables in noncollider experiments, and discuss

future prospects of applications of kinematic variables to upcoming experiments.

One of the crucial differences in noncollider experiments from collider-based experiments is that the transverse plane for a given event is usually ill defined. In typical collider experiments, the initial-state particles have their momenta aligned with the beam axis such that the transverse plane is literally transverse to the beam direction and most of the transverse variables are defined with respect to this plane. By contrast, this is not always the case for noncollider experiments. For example, in beam-focused neutrino experiments, source particles of neutrinos (such as charged pions, kaons, and muons) are focused and aligned to the particle-beam axis by the magnets in the horn system and then decay to neutrinos. Although the source particles are highly boosted in the forward direction, the neutrinos come with a nonzero angular spread with respect to the beam axis, and as a consequence we do not know the "neutrino beam" direction event by event. Likewise, in dark-matter or cosmic-ray detection experiments the incoming direction of dark-matter or cosmic particles is not known *a priori*. In these experiments, therefore, any variables defined on the beam-transverse plane do not allow for robust physical interpretations unless they are redefined with appropriate prescriptions. Instead, basic quantities (energy, timing, etc.), invariant quantities (such as invariant mass), or their combinations are more straightforwardly applicable.

Energy.—Energy is one of the most widely used variables in particle physics experiments, as it is a basic physics quantity to measure at detectors. Examples of a few uses follow.

(a) In conventional dark-matter direct detection experiments targeting WIMP dark-matter candidates, the shape of the nuclear recoil energy spectrum carries information about the dark-matter properties. One can estimate the mass scale of dark matter (Jungman, Kamionkowski, and Griest, 1996) or test to determine whether the observed events are caused by inelastic dark matter (Tucker-Smith and Weiner, 2001).

(b) In stopped-pion neutrino experiments [such as COHERENT (Akimov *et al.*, 2017, 2018, 2020) and CCM (Aguilar-Arevalo *et al.*, 2022a)], the energy is used to eliminate the pion-induced muon neutrino events in the search for low-mass dark matter. Since the beam energy of these experiments is small, π^+ produced in the beam target material loses its kinetic energy and stops before decaying to a μ^+ and a ν_μ. The energy of ν_μ is single valued at ∼30 MeV so that the recoil energy of ν_μ scattering events is bounded from above. By contrast, vector-portal dark matter coming from the π^0 decay through a dark photon is typically more energetic and hence deposits more energy into the detector. An energy cut rejects ν_μ-induced events, leading to a dark-matter signal-rich region (deNiverville, Pospelov, and Ritz, 2015; Dutta *et al.*, 2020, 2022; Aguilar-Arevalo *et al.*, 2022a, 2022b).

(c) The energy peak is useful in the energy distribution of cosmic photons from neutral pion decays. In a cosmic shower, π^0's are produced with various boost factors. Since π^0 is a scalar and its decay is a two-body process, the peak position is identified as half of the π^0 mass (Carlson, Hooper, and King, 1950), as discussed in Sec. VI.A in a more general context.

(d) The energy of the emitted electrons is the primary observable in a number of neutrino experiments attempting to detect neutrinoless double-beta decay, which is a smoking gun for the Majorana nature of the neutrinos. For recent reviews on the status and prospects of neutrinoless double-beta decay, see Dolinski, Poon, and Rodejohann (2019), Cirigliano *et al.* (2022), and Giunti *et al.* (2022).

Timing.—Timing is also a readily accessible quantity in many of the aforementioned experiments. As discussed in Sec. VI.B, it is important to set the reference time (i.e., t_0) in order to render the timing values meaningful. This is deeply connected to the event triggering. In fixed-target-type experiments, the beam-on time is often set at t_0. Three application examples follow.

(a) In the previously mentioned stopped-pion neutrino experiments whose proton beam energy is ∼1 GeV, beam-related neutrons would give rise to an enormous amount of background. However, owing to the scale of the beam energy, most of the produced neutrons are slowly moving, so their arrival timing at the detector is delayed compared to the pion-induced neutrino events. Therefore, restricting to the prompt region, one can efficiently reject beam-related neutrons; see Aguilar-Arevalo *et al.* (2022a, 2022b)].

(b) In a similar manner, neutrinos from muon decays can be vetoed using a timing cut in the stopped-pion neutrino experiments. Since a muon is much longer lived than a charged pion, muon-induced neutrinos typically arrive at the detector much later than pion-induced neutrinos. In other words, muon-induced neutrino events usually fall in delayed timing bins. The previously mentioned low-mass dark matter is also prompt, as it comes from the rare π^0 decay. Therefore, a timing cut can significantly reduce not only beam-related neutron backgrounds but also muon-induced "delayed" neutrino events while retaining as many dark-matter events as possible (Dutta *et al.*, 2020, 2022).

(c) An inverted timing cut can be utilized in the beam-focused neutrino experiments. The MiniBooNE Collaboration set the limit for WIMP dark-matter candidates based on the fact that no significant number of events were observed in their delayed timing bins (Dharmapalan *et al.*, 2012; Aguilar-Arevalo *et al.*, 2018). If a WIMP candidate with a sub-GeV or greater mass were produced in the MiniBooNE target, it would travel slowly because the beam energy is as small as ∼8 GeV.

Angle or directionality.—The angle variable is useful if the source point is well known, momenta of the visible particles can be measured, and the angular resolution is good enough. In typical accelerator-based experiments, the angle is usually

defined with respect to the beam axis, visible particles are energetic enough to measure their three-momentum, and detectors (calorimeters, liquid argon time projection chamber detectors, etc.) are capable of measuring angles precisely.

An angle can also be defined in the search for cosmogenic signals. For example, a class of boosted dark-matter models built upon a nonminimal dark-sector framework (Belanger and Park, 2012) predict that a certain dark-matter component can be produced with a significant boost factor in the Universe by the pair annihilation of the halo dark-matter component (Agashe *et al.*, 2014). Therefore, visible particles (such as recoil electrons) induced by the scattering of boosted dark matter can be not only energetic enough to allow for the measurement of their three-momenta but also forward directed enough to be aligned with the momentum of the incoming boosted dark matter. The dominant fraction of the flux of this so-called boosted dark matter comes from regions where halo dark matter is densely populated, for instance , the Galactic Center (Agashe *et al.*, 2014; Kim, 2016; Alhazmi *et al.*, 2017), dwarf galaxies (Necib *et al.*, 2017), and the Sun (Berger, Cui, and Zhao, 2015; Kong, Mohlabeng, and Park, 2015; Alhazmi *et al.*, 2017) in the solar-captured boosted dark-matter scenarios. Therefore, the line extended between these source points and the detector location can be taken as a reference axis. If a detector features a good angular resolution, one may define a signal-rich region by selecting the events in which the angles of visible particles with respect to the reference axis are within a certain range. The Super-Kamiokande Collaboration used angle cuts to perform a search for Galactic boosted dark matter and solar-captured boosted dark matter that is interacting with electrons and set the first limits for models of two-component boosted dark matter (Kachulis *et al.*, 2018).

Complex variables.—Beyond the basic quantities that have been discussed thus far, complex kinematic variables constructed with basic quantities are being used in a wide range of noncollider experiments, as they are equipped with high-capability detectors with good angular, spatial, and/or energy-momentum resolutions. A couple of examples follow.

(a) A wide range of dark-sector scenarios predict the production of low-mass dark matter (say, χ) in various beam-induced neutrino experiments. An extensively investigated detection channel is the elastic scattering of dark matter off an electron inside the detector material: $\chi + e^- \to \chi + e^-$. One of the major backgrounds to this signal is the charged-current quasielastic (CCQE) scattering of electron neutrinos, i.e., $\nu_e + n \to e^- + p$ or $\bar{\nu}_e + p \to e^+ + n$, where the final-state nucleon is not energetic enough to be detected. It was demonstrated that this type of signal-faking event can be significantly rejected with an application of the $E_e\theta_e^2$ cut, with E_e and θ_e the energy and the angle of the final-state electron. For example, an $E_e\theta_e^2 < 5$ MeV rad^2 cut can eliminate about 99% of the CCQE events at the NOνA near detector (deNiverville and Frugiuele, 2019), and an $E_e\theta_e^2 < 2$ MeV rad^2 cut can suppress the number of CCQE events by ∼99.9% at the DUNE near detector (De Romeri, Kelly, and Machado, 2019).

(b) A class of well-motivated new-physics models that can be tested at neutrino experiments predicts upscattering of the incoming particles, for example, upscattering of a SM neutrino to a heavier sterile neutrino (say, N_R) through mixing (Bertuzzo *et al.*, 2018) and upscattering of dark matter to a heavier dark-sector state (say, χ') (Tucker-Smith and Weiner, 2001; Izaguirre *et al.*, 2014; Kim, Park, and Shin, 2017). These upscattered states may decay into a set of visible particles in addition to the recoiling particle emerging from the primary scattering of the incoming neutrino or dark matter. Thus, there can be multiple visible particles in the final state, thereby allowing for constructing complex variables such as invariant masses (Kim, Park, and Shin, 2017).

XI. CONCLUSIONS AND OUTLOOK

In general, the outcome of any particle physics experiment (whether studying scattering or decay processes) is a measured probability distribution in the relevant phase space of the final state. In typical situations, the phase space is high dimensional and the observed features are difficult to visualize. Furthermore, for many interesting signals some information, such as that related to the kinematics of invisible particles like neutrinos or dark-matter candidates, may be missing. In that case it makes sense to perform dimensional reduction to the lower-dimensional observable slice of the phase space. In doing so, a major goal is to use proper kinematic variables that retain as much information as possible about the underlying physics, features, etc.

The higher-level variables that are derived from the measured particle kinematic information are generically referred to as kinematic variables. Depending on the type of experimental signature and/or the goal of the analysis, many different kinematic variables have been introduced and discussed over the years in the particle phenomenology literature. The main purpose of this review was to collect and summarize all those recent developments in one place. We also provided the motivation for introducing each variable and its applicability and limitations, together with a guide to the relevant references. Note that in practice one often encounters several variations of the same kinematic variable, depending on the analysis, experimental conditions, etc. In that sense, this review is an attempt at some standardization of the definitions of kinematic variables. Nevertheless, those definitions should not be taken as written in stone and should instead be open to reinterpretations and modifications whenever such a need arises.

Many of the traditional questions and approaches in particle kinematics are now being reevaluated using machine learning. The ability of ML to better capture the high-dimensional correlations in data may lead to superior performance, at the expense of introducing unphysical hyperparameters and perhaps less transparency and interpretability. At the same time, kinematic variables can be incorporated into the ML approaches, thus boosting their performance and interpretability. The general methods that have guided particle phenomenologists in deriving these kinematic variables can be

used in other fields of science and are therefore of interest outside the domain of particle physics.

ACKNOWLEDGMENTS

This review was written at the request of the Theory Frontier Collider Phenomenology group (TF07) of the Snowmass 2021–22 Particle Physics Community Planning Exercise (Maltoni *et al.*, 2022). Much of the work reviewed here was inspired by (or done in collaboration with) the late Luc Pape, who was a great mentor and role model to us and many others. We thank Roberto Di Nardo, Lance Dixon, Roy Forestano, Stephen Martin, Federico Meloni, and Eyup Unlu for the discussions and comments on the manuscript. K. K., K. T. M., and P. S. thank the Aspen Center for Physics for its hospitality during the completion of this work, which was supported in part by National Science Foundation Grant No. PHY-1607611. D. K. is supported by DOE Grant No. DE-SC0010813. K. K. is supported in part by U.S. DOE Grant NO. DE-SC0021447. K. T. M. is supported in part by DOE Grant No. DE-SC0022148. M. P. is supported by National Research Foundation of Korea Grant No. NRF-2021R1A2C4002551. P. S. is partially supported by the U.S. Department of Energy, Office of Science, Office of High Energy Physics QuantISED program under the grants "HEP Machine Learning and Optimization Go Quantum" (Award No. 0000240323) and "DOE QuantiSED Consortium QCCFP-QMLQCF" (Award No. DE-SC0019219). This manuscript has been authored by employees of Fermi Research Alliance, LLC, under Contract No. DEAC02-07CH11359 with the U.S. Department of Energy, Office of Science, Office of High Energy Physics.

APPENDIX A: REAL-WORLD CHALLENGES

1. Experimental uncertainties

Realistic measurements of kinematic variables are affected by various experimental uncertainties. To begin, low-level measurements are subject to intrinsic uncertainties, for instance, missing tracker hits, calorimeter activity below the detectable threshold, and instrumental noise. In addition, when high-level objects (such as a jet of particles) are reconstructed, the measurements are further affected by uncertainties arising from the definition of the high-level object.

Popular packages for fast detector simulation of multipurpose detectors include DELPHES (de Favereau *et al.*, 2014), `AtlFast3` (Aad *et al.*, 2022a), `AcerDET` (Richter-Was, 2002; Mikos and Richter-Was, 2015), and PGS (Conway, 1998). They use Gaussian smearing to parametrize the energy resolution ΔE of a calorimeter by noise (N), stochastic (S), and constant (C) terms,

$$\frac{\Delta E}{E} = \sqrt{\left(\frac{N}{E}\right)^2 + \left(\frac{S}{\sqrt{E}}\right)^2 + C^2}, \tag{A1}$$

where the constants N, S, and C are specific to a given experiment and calorimeter type (Han, 2005; de Favereau *et al.*, 2014). The momentum resolution Δp_T based on a curvature measurement can be generically expressed as (Han, 2005; de Favereau *et al.*, 2014)

$$\frac{\Delta p_T}{p_T} = a p_T \oplus b, \tag{A2}$$

where a and b are resolution parameters specific to the detector of interest.

The experimental environment brings additional challenges in the measurements of kinematic quantities. For example, when the average number of interactions per bunch crossing significantly exceeds 1, a number of soft (minimum bias) events accompany the hard scattering event, thereby confusing its interpretation and biasing the kinematic measurements. Such pileup effects may be mitigated by installing new precision timing detectors (CMS Collaboration, 2017) or by analysis techniques using substructure (Aad *et al.*, 2012a; Bertolini *et al.*, 2014; Kogler *et al.*, 2019; Soyez, 2019) or machine learning (Komiske *et al.*, 2017; Arjona Martínez *et al.*, 2019).

These effects can be controlled and improved upon by exploiting the data themselves. Extensive review of the progress in understanding the experimental systematics is beyond the scope of this review. For our purposes, the effect of the detector resolution is to smear the sharp kinematic features that are expected in the ideal case with perfect resolution. For example, the extraction of kinematic end points will have to be done by modeling the shape of the distribution in the vicinity of the end point while taking the detector resolution into account. This highlights the importance of designing the right kinematic variables, namely, those that are as robust as possible to all of these experimental effects.

2. Theoretical uncertainties

Establishing the usefulness of a kinematic variable, for instance, in measuring a parameter of the fundamental Lagrangian, requires extensive calculations of (i) the theoretical predictions for the observable under study, (ii) the sensitivity of the designed kinematic variable to the quantity that we want to extract, and (iii) a number of auxiliary quantities that need to be controlled in experiments. It is crucial to control all of the details, and especially approximations, that characterize these theoretical computations.

Higher orders in perturbation theory.—The vast majority of calculations, especially automated ones, are done at a fixed order in perturbation theory. The first category of uncertainties arises due to missing next-to-leading-order (NLO) contributions. Corrections of this sort can arise from QCD or electroweak interactions or both. The impact of missing higher orders is typically evaluated by variations of scales and other possible unphysical parameters that are introduced for strictly computational purposes and should have zero impact on an all-order calculation.

Fragmentation and hadronization modeling.—Theoretical computations in perturbation theory are done at the parton level and describe processes limited to a small total number of particles that depends on the perturbation theory order. The hadronization of colored partons is described by

phenomenological models, which introduce another category of theoretical uncertainties. They can be estimated by (i) comparing the results from different event generators, (ii) varying the underlying model parameters within acceptable ranges, etc. Additional complications stem from the different possible definitions of the reconstructed jets (Cacciari, Salam, and Soyez, 2012) and the need for a matching scheme between the corresponding jet and parton configurations (Hoeche *et al.*, 2005).

Parton distribution functions.—At hadron colliders, parton-level calculations need to be convoluted with PDFs that contain a lot of uncertain parameters. To propagate the PDF uncertainty to some kinematic variable, the latter must be evaluated for each member of the PDF set (Butterworth *et al.*, 2016).

Narrow-width approximation.—Another commonly used approximation relies on the fact that, in the limit of a narrow particle width, the Breit-Wigner distribution approaches a Dirac δ function. This narrow-width approximation simplifies the treatment of multiparticle final states by iteratively factorizing the computation into the production of parent particles and their subsequent decay. In this approximation the parent particles are exactly on their mass shell and their quantum numbers, including polarization, are in well-defined quantum mechanical pure states. In reality, owing to the unstable nature of the parent particles, their momenta should be smeared over a region close to their mass shell and, furthermore, their polarization should be treated as a density matrix with fully quantum mechanical interference properly taken into account. Depending on the kinematic variable under consideration, the off-shell-ness or polarization effects may play an important role.

Finite Monte Carlo statistics.—Yet another source of theoretical uncertainty is due to the finiteness of the simulated MC samples for the relevant theoretic models under consideration. It is important to keep this MC statistical uncertainty under control so that it does not bottleneck the overall sensitivity of the experiment. The MC statistical uncertainty can be made arbitrarily small by increasing the simulation statistics. However, there are often limitations to the amount of computational resources available, which in turn limits the number of events that can be produced. In this context, keeping in mind the increased computational demands at future colliders, it is important to (i) speed up the MC production pipelines and (ii) achieve a better return in terms of sensitivity reached per event simulated. The latter can be accomplished by preferentially producing events with high utility to the experiment (with appropriate biasing techniques) (Amoroso *et al.*, 2021; Matchev and Shyamsundar, 2021).

APPENDIX B: REAL-WORLD EXAMPLES: *W* AND TOP PHYSICS

To put much of our previous rather abstract discussion in context, in this appendix we focus on the physics of the W boson and the top quark, which provide useful laboratories to illustrate the design of kinematic variables and test various ideas motivated by BSM searches and measurements.

Testing kinematic variables in different final states.—The W boson (and as a result the top quark) has several possible decay modes, leading to a large variety of possible final-state signatures. Some of the signatures involve hadronic jets and have the largest rate but also suffer from larger experimental uncertainties due to the mismeasurement of jet properties. This requires a careful design of kinematic variables that takes into account the typical QCD environment. The alternative decay modes contain well-measured charged leptons, but at the same time have reduced statistics. W decays to charged leptons inevitably bring along neutrinos, which cannot be measured and are thus associated with missing transverse momentum. This rich variety of final states allows one to test different kinematic observables that are designed with specific experimental signatures in mind.

The evolution from discovery to precision measurements.—The history of W and top physics illustrates the evolution from the early era of discovery with just a handful of events to the later stages of precision measurements with large datasets. Correspondingly, the experimental analyses transition from being statistically limited to being limited by experimental systematics and theoretical uncertainties. For example, it is noteworthy to look at the evolution of the top quark mass measurement, which was done with one putative $t\bar{t}$ event at Tevatron run I (Dalitz and Goldstein, 1992) and heavily relied on the predicted properties of the top quark in the SM. Modern m_W and m_t measurements instead tend to rely on theoretical inputs as little as possible and try to minimize the modeling uncertainties. For example, LHC measurements aim at uncertainties of the order of Λ_{QCD}, where a number of theoretical issues start to emerge. Future measurements at the HL-LHC will face similar theoretical issues.

A large amount of theoretical and experimental effort has been devoted in recent years to getting these uncertainties under control. In fact, current and future accumulated data at the LHC, in principle, allow for the extraction of these masses at an extraordinary precision level (CMS Collaboration, 2013c), but we are currently unable to exploit this large dataset because of systematic uncertainties in measurements and theoretical uncertainties in the computations needed to even define properly the observables used in the analysis. The target for these measurements is to attain the 10^{-4} level through observables and kinematic quantities that are as robust as attainable to possible mismodeling of detector effects, insufficiently accurate theoretical calculations, and other sources of systematic errors.

Test bed for new-physics methods.—Since no new physics has yet emerged at the LHC, concrete experience has been accumulated only about the measurements of SM particle masses. In this context, the measurement of the masses of the W boson and the top quark has served as a playground for new ideas to be applied in future new-physics measurements. For example, some new-physics models predict signatures of boosted resonances that can be understood (both theoretically and experimentally) by studying boosted top quarks and W bosons in the existing data (Aaboud *et al.*, 2018f; Sirunyan *et al.*, 2020b; Nachman *et al.*, 2022).

In Appendixes B.1 and B.2 we review the challenges posed by the measurements of m_W and m_t. We also review the kinematic variables used in these measurements, with mentions of the sections where the kinematic variables were

introduced and explained in more detail. We first discuss the m_W measurement in Appendix B.1 as the W decays are topologically simpler, followed by the m_t measurement in Appendix B.2.

1. W-boson mass (m_W)

The measurement of the W-boson mass is the simplest example, yet a nontrivial one, and showcases the importance of employing clever kinematic variables. It is also a good demonstration of the role of theory in performing precise measurements and scrutinizing possible sources of uncertainties. The W-boson mass has been measured thus far at e^+e^- (Schael *et al.*, 2013), ep (Chekanov *et al.*, 2002), and hadron colliders (Aaltonen *et al.*, 2013; Andari, 2017; Aaboud *et al.*, 2018e; Pili, 2019). Future prospects for LHC and circular e^+e^- colliders were discussed by the ATLAS Collaboration (2018a) and Azzurri (2021). As the W-boson mass is one of the possible input parameters of the SM, this measurement has foundational importance for precision tests of the SM.

The current target is to reach a total uncertainty of the order of 10 MeV (about 10^{-4} relative accuracy), which would allow one to obtain a precision comparable to the indirect determinations of m_W from the SM electroweak fit (Baak *et al.*, 2014). Given this ambitious target, a large part of the discussion has focused on the reduction and modeling of both experimental and theoretical systematic uncertainties. Kinematic variables have historically played an important role in devising measurements robust to these uncertainties. A summary of the W mass measurement techniques is presented in Table III.

Presently employed methods use the spectrum of transverse momentum of the charged leptons $p_{T,\ell}$ (Aaboud *et al.*, 2018e) and the transverse mass m_T (Smith, van Neerven, and Vermaseren, 1983) in leptonic W decays. These two simple variables illustrate how the evolving performances of the experiments and the depth of the theoretical interpretation of the measurement forces a continuous evolution of the kinematic variables best suited for the job. For example, the transverse mass (discussed in Sec. V.B) played an important role in the W discovery (Arnison *et al.*, 1983a; Banner *et al.*, 1983) and the early m_W determinations thanks to its robustness against PDF uncertainties at hadron colliders. In recent years, as the precision target has shifted toward ever smaller uncertainties, the transverse mass hit a bottleneck arising from the necessity of using missing transverse momentum. Hence, in modern measurements of m_W it needs to be complemented by other observables. A number of alternative approaches have thus been proposed, starting with strategies utilizing the joint m_T and lepton p_T distribution (Aaboud *et al.*, 2018e). The additional complementary information in each of those two variables, as well as recent improvements in the determination of the proton PDF, has lessened the impact of the m_W bottleneck.

TABLE III. Summary of methods proposed for the measurement of the W-boson mass.

Method	Reference
$p_{T,\ell}$	Aaboud *et al.* (2018e)
m_T	Smith, van Neerven, and Vermaseren (1983)
Singularity variables	Rujula and Galindo (2011)
Derivatives of the energy distribution	Bianchini and Rolandi (2019)

In addition to targeted kinematic variables design, a great amount of further theory inputs has increased the robustness of this mass measurement in recent years. At the desired precisions for this mass measurement, one needs to keep not only the effect of PDF uncertainties but also their related correlations well under control (Bozzi, Rojo, and Vicini, 2011; Bozzi, Citelli, and Vicini, 2015; Bozzi *et al.*, 2015; Bagnaschi and Vicini, 2021), as well as high-order QCD and electroweak corrections [see Behring *et al.* (2021) and references therein], which can bias the measurement.

The utility of singularity conditions and singularity variables was recently explored in the context of the W mass measurement by Rujula and Galindo (2011); see also Sec. V.C. The underlying idea is to formulate a kinematic variable that minimizes the amount of information lost when projecting onto the phase space of visible particles. We are not aware of experimental studies using these types of variables, nor of theory studies seeking to quantify their robustness beyond the leading-order (LO) picture on which the variables are built.

A different approach focusing on only the observable momentum of the charged lepton has been proposed. Using the fact that at LO in perturbation theory the decay of a spin-1 mother into a pair of spin-half particles can contain only a few spherical harmonics, Bianchini and Rolandi (2019) proposed using the energy distribution of the leptons from the W-boson decay in an approach similar to those of Agashe, Franceschini, and Kim (2013) and Agashe, Franceschini, Kim, and Schulze (2016); see Sec. VI.A. It identified several possible features in the first and second derivatives of the energy distribution, which can provide further information on the mass of the W boson, even in cases where the peak of the energy distribution does not have the properties exploited by Agashe, Franceschini, and Kim (2013).

2. Top quark mass (m_t)

Top quark physics has been a major cornerstone of the physics programs at both the Tevatron and the LHC (Beneke *et al.*, 2000; Chakraborty, Konigsberg, and Rainwater, 2003; Kehoe, Narain, and Kumar, 2008; Husemann, 2017). Here we focus on the measurement of the top quark mass (Corcella, 2019; Hoang, 2020) in $t\bar{t}$ pair production, highlighting the diversity of efforts put in place to attack this important problem.

The simplest kinematic idea is to measure the invariant mass of the decay products of a given top quark. This method is conceptually straightforward and lies at the heart of the most precise results currently available. The concrete implementation of the idea depends on the specific channel resulting from the hadronic (j) or leptonic decays (ℓ) of the two W bosons: all hadronic (jj), semileptonic (ℓj), or dilepton ($\ell\ell$); see Table IV for a summary. At the same time, the method faces several challenges that are reviewed in the following.

TABLE IV. A summary of top quark mass measurements in different channels and the corresponding kinematic variables.

Channel	Kinematic variables	Reference(s)
$\ell j \oplus jj$	M_{bjj} [Eq. (B1)]	Aaboud *et al.* (2017f)
$\ell\ell \oplus \ell j$	$M_{b\ell}$ [Eq. (B2)]	CMS Collaboration (2014)
$\ell\ell$ $(e\mu)$	Leptonic observables [Eq. (B3)]	Frixione and Mitov (2014), Aaboud *et al.* (2017a), and Czakon, Mitov, and Poncelet (2021)
ℓj	$I(\hat{m})$ [Eq. (B6)]	Kawabata *et al.* (2015)
ℓj	$M_{\ell\mu}$ [Eq. (B7)], $M_{3\ell}$ [Eq. (B8)]	Kharchilava (2000) and Czakon *et al.* (2021)
$e\mu$	E_b (Sec. VI.A)	Agashe, Franceschini, and Kim (2013) and CMS Collaboration (2015)
$\ell\ell \oplus \ell j$	L_{xy} [Eq. (B9)]	Hill, Incandela, and Lamb (2005) and Khachatryan *et al.* (2016)
ℓj	$s_{\bar{t}tj}$ [Eq. (B10)]	Alioli *et al.* (2013) and Aad *et al.* (2019a)

The most straightforward channel would be the fully hadronic (jj) one (Aaboud *et al.*, 2017f), in which all top decay products can be fully reconstructed [subject to combinatorial ambiguities (Lee *et al.*, 2020; Badea *et al.*, 2022; Shmakov *et al.*, 2022)]. In that case, the top quark mass emerges as a peak in the invariant mass distribution of the b jet and the two jets j_1 and j_2 from the hadronic decay of the associated W boson:

$$M_{bjj} = \sqrt{(p_b + p_{j_1} + p_{j_2})^2}. \tag{B1}$$

The measurement of hadrons, however, is imprecise due to the large QCD backgrounds, the relatively poor hadronic calorimeter resolution, and the difficulty in associating the streams of observed hadrons with the underlying parton objects in QCD (Cacciari, Salam, and Soyez, 2012; Czakon *et al.*, 2021; Kogler *et al.*, 2019). Top quark mass measurements in the fully hadronic channel (jj) are not competitive, and the best measurements are presently obtained from the semileptonic channel (ℓj). Here the challenge lies in indirectly reconstructing the momentum of the missing neutrino. Note that its transverse component can be obtained from the missing transverse momentum measurement [Eq. (8)] (which uses all visible particles in the event and is therefore also subject to the large hadronic resolution), while the longitudinal neutrino momentum component is derived from the W-boson mass constraint, which typically gives two solutions.

In addition to these experimental issues, the definition of the top quark mass as the peak of a reconstructed invariant mass has proven to be difficult to interpret on theoretical grounds (Hoang, 2014; Beneke *et al.*, 2017). In fact, the top quark, as it is colored, cannot exist as a long-distance object. It has to turn into a color-singlet object either by forming hadrons of its own flavor or via the hadronization of its decay products. The theoretical definition of a mass for the top quark that can be used beyond the LO of perturbation theory (a necessary requirement when we aim for 1 GeV or less uncertainty for this measurement) has required a critical reevaluation of the entire strategy to measure this quantity; for a cogent discussion of this issue, see Hoang (2014). Indeed, the extraction of the top quark mass from templates of theoretical predictions based on detailed event simulation from fixed-order (often leading-order) approximations, possibly supplemented by leading logarithm parton showers, has been put into question when a precision of around 1 GeV is claimed. Efforts are in place to obtain more precise theoretical templates for this type of method; see Ježo *et al.* (2016), Ferrario Ravasio *et al.* (2018), and Ferrario Ravasio (2019).

For all of these reasons, there is an impetus to try out new top quark mass measurement methods that are less sensitive to these theoretical uncertainties and/or are affected by different types of experimental uncertainties. One such method relies on the strict inequality for the invariant mass of a subsystem of the decay products. In particular, considering the bottom jet (b) and the charged lepton ($\ell \in \{e, \mu\}$) in the semileptonic top decay, one can exploit the relation

$$M_{b\ell} \leq m_t. \tag{B2}$$

The measurement of the end point, or the shape around the end point, of the bottom-lepton invariant mass distribution has led to new determinations of the top quark mass (CMS Collaboration, 2012; Sirunyan *et al.*, 2017a) that probe the jet energy uncertainty differently than other methods since the involved jets are b jets. In addition, since Eq. (B2) assumes perfectly on-shell top quarks, this method is sensitive to off-shell effects and can be used to diagnose their importance for the measurement.

As prompt leptons from the top quark decay are arising from a color-singlet W boson, it has been proposed to use kinematic variables based solely on leptons to measure the top quark mass, Frixione and Mitov (2014) explored the set

$$\{p_{T\ell}, p_{T\ell^+\ell^-}, p_{T\ell^+} + p_{T\ell^-}, E_{\ell^+} + E_{\ell^-}, m_{\ell^+\ell^-}\}, \tag{B3}$$

where

$$p_{T\ell^+\ell^-} = |\vec{p}_{T\ell^+} + \vec{p}_{T\ell^-}| \tag{B4}$$

and

$$m_{\ell^+\ell^-} = \sqrt{(p_{\ell^+} + p_{\ell^-})^2} \tag{B5}$$

are, respectively, the magnitude of the transverse momentum and the invariant mass of the $\ell^+\ell^-$ system in dilepton $t\bar{t}$ events. To reduce the background, one could focus on the opposite flavor channel ($e\mu$) only (Aaboud *et al.*, 2017a) and further could consider angular leptonic observables like the differences in pseudorapidity or azimuthal angle (Czakon, Mitov, and Poncelet, 2021). The advantages of such leptonic kinematic observables include avoiding the need for explicit top quark reconstruction, minimal sensitivity to the modeling

of long-distance effects, and competitive precision, with theoretical errors on the extracted top mass of the order of 0.8 GeV (Frixione and Mitov, 2014).

Based on purely leptonic measurements, it has been proposed to correlate the top quark mass to a suitably defined integral of the energy distribution of prompt leptons (Kawabata *et al.*, 2015). The quantity of interest is an integral of the energy distribution times a special weight function w, which is derived from kinematic properties of the top quark decay in perturbation theory as

$$I(\hat{m}) = \int dE_\ell \frac{d\Gamma(\hat{m})}{dE_\ell} w(E_\ell). \tag{B6}$$

Therefore, when the integral is computed for the true value m realized in data, one expects $I(\hat{m} = m) = 0$.

The idea of using only leptons to construct an observable sensitive to the top quark mass has also been explored in the context of pairs of leptons arising from the same top quark, for instance, one lepton from the leptonic decay of the W boson and the muon originating from the semileptonic decay of the b-quark-initiated hadrons. This type of measurement (Aaltonen *et al.*, 2009; Aad *et al.*, 2023) is called soft-leptons, as it uses a nonprompt, soft muon from the decay of the B hadron appearing in the top decay. The computation of templates for

$$m_{\ell\mu} = \sqrt{(p_\ell + p_\mu)^2} \tag{B7}$$

relies on the hadronic physics of B hadrons and their semileptonic decays. Thus, this method is important for understanding hadronization effects. Variations of this idea have also been considered: for example, it has been proposed to use the invariant mass

$$m_{3\ell} = \sqrt{\left(\sum p_\ell\right)^2} \tag{B8}$$

formed by three leptons from the same top quark, following an early proposal to use rare $B \to J/\psi + X$ decays, which can be tagged (Kharchilava, 2000) in clean leptonic modes of the J/ψ.

A top quark mass measurement has also been proposed using only the measured spectrum of the b-jet energy E_b (Agashe, Franceschini, and Kim, 2013; Agashe, Franceschini, Kim, and Schulze, 2016); see also Sec. VI.A. Like the approaches based on leptonic variables, this method does not require a definition of a reconstructed top quark. In addition, the position of the peak of the distribution is predicted to be insensitive to the production mechanism of the top quarks as long as the sample of measured b jets arises from unpolarized top quarks, i.e., an equal mixture of left-handed and right-handed top quarks (Agashe, Franceschini, and Kim, 2013). The observable is simple enough that it can be reliably computed in perturbation theory, to date up to NLO in QCD both at the jet level and at the hadronic level (Agashe, Franceschini, Kim, and Schulze, 2016), where the relevant uncertainties are those from jet energy measurements and from hadronization, respectively.

Given the preponderance of methods based on kinematic variables with units of GeV (energy, mass, or momentum), alternative approaches utilizing variables with different dimensions have also been proposed, as they present truly independent determinations of the top quark mass. One such proposal was put forward by Hill, Incandela, and Lamb (2005). The idea was to measure B hadron flight lengths in the detector, relying on the fact that the hadron decay is controlled by its proper lifetime and its boost, with the latter being larger when the B mother is a heavier particle. From the experimental point of view this method has the advantages of using length measurements, which are precise thanks to tracking, and of being largely unaffected by jet energetics or choice of jet definition. Thus far this method has been implemented only in experiments measuring the transverse decay length L_{xy} flown in the plane orthogonal to the beam axis

$$L_{xy} = \sqrt{L_x^2 + L_y^2}. \tag{B9}$$

The m_t measurement (CMS Collaboration, 2013a; Khachatryan *et al.*, 2016) has proven to be sensitive to hadronization effects, which is expected since the nature of the B hadrons impacts the result via their proper lifetime and boost. A sensitivity to the top quark production mechanism has also been noted: a different production mechanism leading to harder top quarks can mimic a larger boost of the B hadrons. This problem can be mitigated by focusing on suitable variables that are less sensitive to the production mechanism, for instance, the peak of the B hadron boost distribution (Agashe *et al.*, 2022) that is in a one-to-one relation with the previously discussed b energy peak.

Other mass measurement methods have to do with threshold effects, which manage to exploit basic kinematic inequalities in the context of pp collisions in which some quantities are not readily accessible or controllable. One important observation is that the production rate of a massive particle is sensitive to the available energy; for example, the formation of a pair of massive particles is suppressed when the available center-of-mass energy is below twice the mass of the particle. The rate quickly rises once the center-of-mass energy passes this threshold, and then the cross section follows the usual geometrical scaling. With this idea in mind, it has been proposed to study $t\bar{t}j$ events at the LHC and to use the hardness of the extra jet to control the total invariant mass that enters the actual partonic process $gg \to t\bar{t}j$ or $q\bar{q} \to t\bar{t}j$. Exploiting the dependence of the rate on the hardness of the jet, or using a more comprehensive measure of the partonic center-of-mass energy such as

$$\sqrt{s_{t\bar{t}j}} = \sqrt{(p_t + p_{\bar{t}} + p_j)^2} \tag{B10}$$

given by Alioli *et al.* (2013) and Aad *et al.* (2019a), a method has been proposed using templates computed at NLO in perturbation theory. Like other previously discussed approaches that do not require an object called a top quark

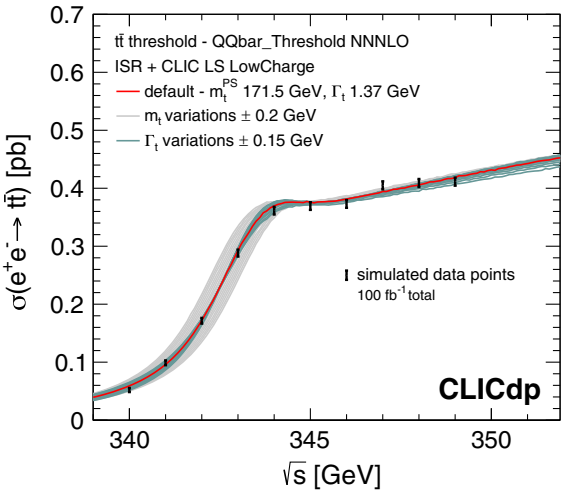

FIG. 31. Top quark mass from a high precision rate calculation at e^+e^- collider. From Abramowicz *et al.*, 2019.

to be reconstructed, this method lends itself to an interpretation of the measurement as the dependence of a suitable observable on a Lagrangian parameter. It is thus considered to give theoretically cleaner results compared to the invariant mass peak method of Eq. (B1). A related proposal has been put forward to identify the top quark mass from bound state effects in the diphoton mass spectrum (Kawabata and Yokoya, 2017). This approach would benefit from a clean definition of the top quark mass in quantum field theory relevant for this phenomenon.

A good understanding of hadronization in top quark events is required for most of the previously discussed m_t measurement methods, in particular, those based on hadrons or soft leptons. Corcella, Franceschini, and Kim (2018) revealed that QCD phenomena must be under control up to minute effects in the description of radiation and hadronization to ensure sub-GeV precision in the top quark mass extraction. When we keep this ambitious goal for hadron-based measurements in mind, traditional variables (Aad *et al.*, 2015a, 2021a, 2022b) as well as newer variables (Corcella, Franceschini, and Kim, 2018) can be used to calibrate these effects on real data.

The need for proper evaluation of theoretical uncertainties and precision control of detector effects is even stronger in the context of measurements to be carried out at future colliders. That is the case for the measurement of the top quark using the dependence of the production cross section on the center-of-mass energy (Seidel, Simon, and Tesar, 2012; Seidel *et al.*, 2013; Maier, 2020; Nowak and Zarnecki, 2021), i.e., a fit of the cross-section measurements to precise theory predictions upon variations of m_t and other relevant quantities (for instance, Γ_t and m_t shown in Fig. 31). In this context it is of the utmost importance to compute rates taking into account (Strassler and Peskin, 1991; Hoang and Teubner, 1998, 1999; Beneke, Jantzen, and Ruiz-Femenia, 2010; Beneke, Piclum, and Rauh, 2014; Beneke *et al.*, 2015, 2016) bound state dynamics, off-shell effects, nonrelativistic

TABLE V. Summary of public codes for numerically computing kinematic variables. Refer to the table footnotes for Web page or repository details.

Code	Reference(s)	Language (requirement)	Kinematic variables
M_{T2}[a]	Lester and Nachman (2015)	PYTHON	M_{T2}
Oxbridge Kinetics Library[b]	Barr, Lester, and Stephens (2003)	PYTHON, C++, ROOT	α_T, M_{T2}, $M_{T\mathrm{Gen}}$ M_{2C}, M_C, M_{CT}, M_{CT2}
OPTIMASS[c]	Cho, Gainer *et al.* (2016)	PYTHON, C++, ROOT	M_2 and the like
YAM2[d]	Park (2021b)	C++	M_2
KLFitter[e]	Erdmann *et al.* (2014)	C++, ROOT	Top quark reconstruction
RestFrames[f]	Jackson and Rogan (2017)	C++, ROOT	Recursive jigsaw reconstruction
MoMEMta[g]	Brochet *et al.* (2019)	C++, ROOT	Modular matrix element method
ROOT[h]	Antcheva *et al.* (2009, 2011)	ROOT	Basic kinematic variables and M_T
WIMPMASS[i]	Cheng *et al.*, 2007, 2008, 2009) and Cheng and Han (2008)	C++, ROOT	M_{T2} using bisection method
CLHEP[j]	Lonnblad (1994)	C++	Basic kinematic variables and M_T
FastJet[k]	Cacciari, Salam, and Soyez (2012)	C++	Basic kinematic variables and E_T

[a]See https://pypi.org/project/mt2/.
[b]See https://www.hep.phy.cam.ac.uk/~lester/mt2/.
[c]See https://github.com/hepkosmos/OptiMass.
[d]See https://github.com/cbpark/YAM2.
[e]See https://github.com/KLFitter/KLFitter.
[f]See http://restframes.com.
[g]See https://github.com/MoMEMta/MoMEMta.
[h]See https://root.cern.ch/.
[i]See http://particle.physics.ucdavis.edu/hefti/projects/doku.php?id=wimpmass.
[j]See https://proj-clhep.web.cern.ch/proj-clhep/.
[k]See http://fastjet.fr/.

corrections, electroweak effects, soft corrections that may need resummation, and transfer factors that account for the fraction of the total cross section that ends up in the detector acceptance (Hoang and Stahlhofen, 2014; Chokoufé Nejad *et al.*, 2016; Bach *et al.*, 2018). For the matching between the measured fiducial cross sections and the theoretically cleaner total ones, it will be essential to exploit suitably defined kinematic variables that can serve as diagnostics of the theoretical computations. Furthermore, methods applicable above the threshold will be of much importance in validating the precise measurement from the threshold scan (Boronat *et al.*, 2020).

APPENDIX C: TOOLS AND CODES FOR KINEMATIC VARIABLES

For the benefit of the users of kinematic variables, in Table V we list a few popular public codes for numerically computing some of the kinematic variables described in the main text. We also provide the corresponding reference, language, and system requirements.

REFERENCES

Aaboud, M., *et al.* (ATLAS Collaboration), 2017a, "Measurement of lepton differential distributions and the top quark mass in $t\bar{t}$ production in pp collisions at $\sqrt{s} = 8$ TeV with the ATLAS detector," Eur. Phys. J. C **77**, 804.

Aaboud, M., *et al.* (ATLAS Collaboration), 2017b, "Identification and rejection of pile-up jets at high pseudorapidity with the ATLAS detector," Eur. Phys. J. C **77**, 580.

Aaboud, M., *et al.* (ATLAS Collaboration), 2017c, "Search for dark matter at $\sqrt{s} = 13$ TeV in final states containing an energetic photon and large missing transverse momentum with the ATLAS detector," Eur. Phys. J. C **77**, 393.

Aaboud, M., *et al.* (ATLAS Collaboration), 2017d, "Search for dark matter in association with a Higgs boson decaying to two photons at $\sqrt{s} = 13$ TeV with the ATLAS detector," Phys. Rev. D **96**, 112004.

Aaboud, M., *et al.* (ATLAS Collaboration), 2017e, "Search for Dark Matter Produced in Association with a Higgs Boson Decaying to $b\bar{b}$ Using 36 fb^{-1} of pp Collisions at $\sqrt{s} = 13$ TeV with the ATLAS Detector," Phys. Rev. Lett. **119**, 181804.

Aaboud, M., *et al.* (ATLAS Collaboration), 2017f, "Top-quark mass measurement in the all-hadronic $t\bar{t}$ decay channel at $\sqrt{s} = 8$ TeV with the ATLAS detector," J. High Energy Phys. 09, 118.

Aaboud, M., *et al.* (ATLAS Collaboration), 2018a, "Search for an invisibly decaying Higgs boson or dark matter candidates produced in association with a Z boson in pp collisions at $\sqrt{s} = 13$ TeV with the ATLAS detector," Phys. Lett. B **776**, 318–337.

Aaboud, M., *et al.* (ATLAS Collaboration), 2018b, "Search for dark matter in events with a hadronically decaying vector boson and missing transverse momentum in pp collisions at $\sqrt{s} = 13$ TeV with the ATLAS detector," J. High Energy Phys. 10, 180.

Aaboud, M., *et al.* (ATLAS Collaboration), 2018c, "Search for the Higgs boson produced in association with a vector boson and decaying into two spin-zero particles in the $H \to aa \to 4b$ channel in pp collisions at $\sqrt{s} = 13$ TeV with the ATLAS detector," J. High Energy Phys. 10, 031.

Aaboud, M., *et al.* (ATLAS Collaboration), 2018d, "Measurement of the Higgs boson mass in the $H \to ZZ^* \to 4\ell$ and $H \to \gamma\gamma$ channels with $\sqrt{s} = 13$ TeV pp collisions using the ATLAS detector," Phys. Lett. B **784**, 345–366.

Aaboud, M., *et al.* (ATLAS Collaboration), 2018e, "Measurement of the W-boson mass in pp collisions at $\sqrt{s} = 7$ TeV with the ATLAS detector," Eur. Phys. J. C **78**, 110.

Aaboud, M., *et al.* (ATLAS Collaboration), 2018f, "Measurements of $t\bar{t}$ differential cross-sections of highly boosted top quarks decaying to all-hadronic final states in pp collisions at $\sqrt{s} = 13$ TeV using the ATLAS detector," Phys. Rev. D **98**, 012003.

Aaboud, M., *et al.* (ATLAS Collaboration), 2018g, "Performance of missing transverse momentum reconstruction with the ATLAS detector using proton-proton collisions at $\sqrt{s} = 13$ TeV," Eur. Phys. J. C **78**, 903.

Aaboud, M., *et al.* (ATLAS Collaboration), 2018h, "Search for dark matter and other new phenomena in events with an energetic jet and large missing transverse momentum using the ATLAS detector," J. High Energy Phys. 01, 126.

Aad, Georges, *et al.* (ATLAS Collaboration), 2012a, "Jet mass and substructure of inclusive jets in $\sqrt{s} = 7$ TeV pp collisions with the ATLAS experiment," J. High Energy Phys. 05, 128.

Aad, Georges, *et al.* (ATLAS Collaboration), 2012b, "Observation of a new particle in the search for the standard model Higgs boson with the ATLAS detector at the LHC," Phys. Lett. B **716**, 1–29.

Aad, Georges, *et al.* (ATLAS Collaboration), 2014, "Light-quark and gluon jet discrimination in pp collisions at $\sqrt{s} = 7$ TeV with the ATLAS detector," Eur. Phys. J. C **74**, 3023.

Aad, Georges, *et al.* (ATLAS Collaboration), 2015a, "Determination of the Ratio of b-Quark Fragmentation Fractions f_s/f_d in pp Collisions at $\sqrt{s} = 7$ TeV with the ATLAS Detector," Phys. Rev. Lett. **115**, 262001.

Aad, Georges, *et al.* (ATLAS Collaboration), 2015b, "Search for long-lived, weakly interacting particles that decay to displaced hadronic jets in proton-proton collisions at $\sqrt{s} = 8$ TeV with the ATLAS detector," Phys. Rev. D **92**, 012010.

Aad, Georges, *et al.* (ATLAS Collaboration), 2019a, "Measurement of the top-quark mass in $t\bar{t} + 1$-jet events collected with the ATLAS detector in pp collisions at $\sqrt{s} = 8$ TeV," J. High Energy Phys. 11, 150.

Aad, Georges, *et al.* (ATLAS Collaboration), 2019b, "Search for heavy neutral leptons in decays of W bosons produced in 13 TeV pp collisions using prompt and displaced signatures with the ATLAS detector," J. High Energy Phys. 10, 265.

Aad, Georges, *et al.* (ATLAS Collaboration), 2021a, "Measurement of b-quark fragmentation properties in jets using the decay $B^{\pm} \to J/\psi K^{\pm}$ in pp collisions at $\sqrt{s} = 13$ TeV with the ATLAS detector," J. High Energy Phys. 12, 131.

Aad, Georges, *et al.* (ATLAS Collaboration), 2021b, "Measurement of hadronic event shapes in high-p_T multijet final states at $\sqrt{s} = 13$ TeV with the ATLAS detector," J. High Energy Phys. 01, 188; 01, 188(E) (2021).

Aad, Georges, *et al.* (ATLAS Collaboration), 2021c, "Search for new phenomena in events with an energetic jet and missing transverse momentum in pp collisions at $\sqrt{s} = 13$ TeV with the ATLAS detector," Phys. Rev. D **103**, 112006.

Aad, Georges, *et al.* (ATLAS Collaboration), 2022a, "AtlFast3: The next generation of fast simulation in ATLAS," Comput. Softw. Big Sci. **6**, 7.

Aad, Georges, *et al.* (ATLAS Collaboration), 2022b, "Measurements of jet observables sensitive to b-quark fragmentation in $t\bar{t}$ events at the LHC with the ATLAS detector," Phys. Rev. D **106**, 032008.

Aad, Georges, *et al.* (ATLAS Collaboration), 2023, "Measurement of the top-quark mass using a leptonic invariant mass in pp collisions

at $\sqrt{s} = 13$ TeV with the ATLAS detector," J. High Energy Phys. 06, 019.

Aaltonen, T., *et al.* (CDF Collaboration), 2009, "Measurement of the top quark mass using the invariant mass of lepton pairs in soft muon b-tagged events," Phys. Rev. D **80**, 051104.

Aaltonen, T., *et al.* (CDF Collaboration), 2010, "Measurement of the top quark mass in the dilepton channel using m_{T2} at CDF," Phys. Rev. D **81**, 031102.

Aaltonen, T., *et al.* (CDF Collaboration), 2022, "High-precision measurement of the W boson mass with the CDF II detector," Science **376**, 170–176.

Aaltonen, Timo Antero, *et al.* (CDF and D0 Collaborations), 2013, "Combination of CDF and D0 W-boson mass measurements," Phys. Rev. D **88**, 052018.

Abdallah, J., *et al.* (DELPHI Collaboration), 2003, "A study of the energy evolution of event shape distributions and their means with the DELPHI detector at LEP," Eur. Phys. J. C **29**, 285–312.

Abercrombie, Daniel, *et al.*, 2020, "Dark matter benchmark models for early LHC run-2 searches: Report of the ATLAS/CMS dark matter forum," Phys. Dark Universe **27**, 100371.

Abramowicz, H., *et al.* (CLICdp Collaboration), 2019, "Top-quark physics at the CLIC electron-positron linear collider," J. High Energy Phys. 11, 003.

Abulaiti, Yiming, 2022, "Status of searches for dark matter at the LHC," ATLAS Report No. ATL-PHYS-PROC-2022-003.

Abulencia, A., *et al.* (CDF Collaboration), 2007, "Measurement of the top quark mass in $p\bar{p}$ collisions at $\sqrt{s} = 1.96$ TeV using the decay length technique," Phys. Rev. D **75**, 071102,.

Agarwal, Garvita, Lauren Hay, Ia Iashvili, Benjamin Mannix, Christine McLean, Margaret Morris, Salvatore Rappoccio, and Ulrich Schubert, 2021, "Explainable AI for ML jet taggers using expert variables and layerwise relevance propagation," J. High Energy Phys. 05, 208.

Agashe, K., 2020, "(Towards a) production model-independent top mass measurement using b-hadron decay length," slide presentation, EF03 Heavy Flavor and Top Topical Group Meeting, 2020, https://indico.fnal.gov/event/43738/contributions/188710/attachments/129229/156809/B-hadron_CMS.pdf.

Agashe, Kaustubh, Sagar Airen, Roberto Franceschini, Doojin Kim, and Deepak Sathyan, 2022, "Snowmass2021—White paper, implications of energy peak for collider phenomenology: Top quark mass determination and beyond," arXiv:2204.02928.

Agashe, Kaustubh, Yanou Cui, Lina Necib, and Jesse Thaler, 2014, "(In)direct detection of boosted dark matter," J. Cosmol. Astropart. Phys. 10, 062.

Agashe, Kaustubh, Roberto Franceschini, Sungwoo Hong, and Doojin Kim, 2016, "Energy spectra of massive two-body decay products and mass measurement," J. High Energy Phys. 04, 151.

Agashe, Kaustubh, Roberto Franceschini, and Doojin Kim, 2013, "Simple 'invariance' of two-body decay kinematics," Phys. Rev. D **88**, 057701.

Agashe, Kaustubh, Roberto Franceschini, and Doojin Kim, 2014, "Using energy peaks to measure new particle masses," J. High Energy Phys. 11, 059.

Agashe, Kaustubh, Roberto Franceschini, Doojin Kim, and Markus Schulze, 2016, "Top quark mass determination from the energy peaks of b-jets and B-hadrons at NLO QCD," Eur. Phys. J. C **76**, 636.

Agashe, Kaustubh, Roberto Franceschini, Doojin Kim, and Kyle Wardlow, 2013, "Using energy peaks to count dark matter particles in decays," Phys. Dark Universe **2**, 72–82.

Agashe, Kaustubh, Roberto Franceschini, Doojin Kim, and Kyle Wardlow, 2016, "Mass measurement using energy spectra in three-body decays," J. High Energy Phys. 05, 138.

Agashe, Kaustubh, Doojin Kim, Manuel Toharia, and Devin G. E. Walker, 2010, "Distinguishing dark matter stabilization symmetries using multiple kinematic edges and cusps," Phys. Rev. D **82**, 015007.

Agashe, Kaustubh, Doojin Kim, Devin G. E. Walker, and Lijun Zhu, 2011, "Using M_{T2} to distinguish dark matter stabilization symmetries," Phys. Rev. D **84**, 055020,.

Agrawal, Prateek, Can Kilic, Craig White, and Jiang-Hao Yu, 2014, "Improved mass measurement using the boundary of many-body phase space," Phys. Rev. D **89**, 015021.

Aguilar-Arevalo, A. A., *et al.* (MiniBooNE-DM Collaboration), 2018, "Dark matter search in nucleon, pion, and electron channels from a proton beam dump with MiniBooNE," Phys. Rev. D **98**, 112004.

Aguilar-Arevalo, A. A., *et al.* (CCM Collaboration), 2022a, "First dark matter search results from Coherent CAPTAIN-Mills," Phys. Rev. D **106**, 012001.

Aguilar-Arevalo, A. A., *et al.* (CCM Collaboration), 2022b, "First Leptophobic Dark Matter Search from the Coherent–CAPTAIN-Mills Liquid Argon Detector," Phys. Rev. Lett. **129**, 021801.

Aielli, Giulio, *et al.*, 2020, "Expression of interest for the CODEX-b detector," Eur. Phys. J. C **80**, 1177.

Akimov, D., *et al.* (COHERENT Collaboration), 2017, "Observation of coherent elastic neutrino-nucleus scattering," Science **357**, 1123–1126.

Akimov, D., *et al.* (COHERENT Collaboration), 2018, "COHERENT 2018 at the Spallation Neutron Source," arXiv:1803.09183.

Akimov, D, *et al.* (COHERENT Collaboration), 2020, "Sensitivity of the COHERENT experiment to accelerator-produced dark matter," Phys. Rev. D **102**, 052007.

Akrawy, M. Z., *et al.* (OPAL Collaboration), 1990, "A study of jet production rates and a test of QCD on the Z^0 resonance," Phys. Lett. B **235**, 389–398.

Albertsson, Kim, *et al.*, 2018, "Machine learning in high energy physics community white paper," J. Phys. Conf. Ser. **1085**, 022008.

Albrow, M. G., *et al.*, 1976, "A search for narrow resonances in proton proton collisions at 53-GeV center-of-mass energy," Nucl. Phys. **B114**, 365–379.

Alhazmi, Haider, Zhongtian Dong, Li Huang, Jeong Han Kim, Kyoungchul Kong, and David Shih, 2022, "Resolving combinatorial ambiguities in dilepton $t\bar{t}$ event topologies with neural networks," Phys. Rev. D **105**, 115011.

Alhazmi, Haider, Kyoungchul Kong, Gopolang Mohlabeng, and Jong-Chul Park, 2017, "Boosted dark matter at the deep underground neutrino experiment," J. High Energy Phys. 04, 158.

Alimena, Juliette, *et al.*, 2020, "Searching for long-lived particles beyond the standard model at the Large Hadron Collider," J. Phys. G **47**, 090501.

Alioli, Simone, Patricia Fernandez, Juan Fuster, Adrian Irles, Sven-Olaf Moch, Peter Uwer, and Marcel Vos, 2013, "A new observable to measure the top-quark mass at hadron colliders," Eur. Phys. J. C **73**, 2438.

Allanach, B. C., C. G. Lester, Michael Andrew Parker, and B. R. Webber, 2000, "Measuring sparticle masses in nonuniversal string inspired models at the LHC," J. High Energy Phys. 09, 004.

Ally, D., L. Carpenter, T. Holmes, L. Lee, and P. Wagenknecht, 2022, "Strategies for beam-induced background reduction at muon colliders," arXiv:2203.06773.

Altunkaynak, Baris, Can Kilic, and Matthew D. Klimek, 2017, "Multidimensional phase space methods for mass measurements and decay topology determination," Eur. Phys. J. C **77**, 61.

Alves, Alexandre, Oscar Eboli, and Tilman Plehn, 2006, "It's a gluino," Phys. Rev. D **74**, 095010.

Alves, Alexandre, and C. H. Yamaguchi, 2022, "Reconstruction of missing resonances combining nearest neighbors regressors and neural network classifiers," Eur. Phys. J. C **82**, 746.

Alwall, Johan, Kenji Hiramatsu, Mihoko M. Nojiri, and Yasuhiro Shimizu, 2009, "Novel Reconstruction Technique for New Physics Processes with Initial State Radiation," Phys. Rev. Lett. **103**, 151802.

Amoroso, Simone, *et al.* (HSF Physics Event Generator Working Group), 2021, "Challenges in Monte Carlo event generator software for High-Luminosity LHC," Comput. Softw. Big Sci. **5**, 12.

An, Haipeng, Ran Huo, and Lian-Tao Wang, 2013, "Searching for low mass dark portal at the LHC," Phys. Dark Universe **2**, 50–57.

Andari, Nansi (ATLAS and CMS Collaborations), 2017, "W boson mass measurement," ATLAS Report No. ATL-PHYS-PROC-2017-051.

Andrews, M., J. Alison, S. An, Patrick Bryant, B. Burkle, S. Gleyzer, M. Narain, M. Paulini, B. Poczos, and E. Usai, 2020, "End-to-end jet classification of quarks and gluons with the CMS Open Data," Nucl. Instrum. Methods Phys. Res., Sect. A **977**, 164304.

Andrews, M., M. Paulini, S. Gleyzer, and B. Poczos, 2020, "End-to-end physics event classification with CMS Open Data: Applying image-based deep learning to detector data for the direct classification of collision events at the LHC," Comput. Softw. Big Sci. **4**, 6.

Antcheva, I, *et al.*, 2009, "ROOT: A C++ framework for petabyte data storage, statistical analysis and visualization," Comput. Phys. Commun. **180**, 2499–2512.

Antcheva, I, *et al.*, 2011, "ROOT: A C++ framework for petabyte data storage, statistical analysis and visualization," Comput. Phys. Commun. **182**, 1384–1385.

Arjona Martínez, J., Olmo Cerri, Maurizio Pierini, Maria Spiropulu, and Jean-Roch Vlimant, 2019, "Pileup mitigation at the Large Hadron Collider with graph neural networks," Eur. Phys. J. Plus **134**, 333.

Arkani-Hamed, Nima, Savas Dimopoulos, and G. R. Dvali, 1998, "The hierarchy problem and new dimensions at a millimeter," Phys. Lett. B **429**, 263–272.

Arkani-Hamed, Nima, Gordon L. Kane, Jesse Thaler, and Lian-Tao Wang, 2006, "Supersymmetry and the LHC inverse problem," J. High Energy Phys. 08, 070.

Arnison, G., *et al.* (UA1 Collaboration), 1983a, "Experimental observation of isolated large transverse energy electrons with associated missing energy at $\sqrt{s} = 540$ GeV," Phys. Lett. **122B**, 103–116.

Arnison, G., *et al.* (UA1 Collaboration), 1983b, "Experimental observation of lepton pairs of invariant mass around 95 GeV/c^2 at the CERN SPS collider," Phys. Lett. **126B**, 398–410.

Ask, Stefan, *et al.*, 2012, "From Lagrangians to events: Computer tutorial at the MC4BSM-2012 Workshop," arXiv:1209.0297.

Athanasiou, Christiana, Christopher G. Lester, Jennifer M. Smillie, and Bryan R. Webber, 2006, "Distinguishing spins in decay chains at the Large Hadron Collider," J. High Energy Phys. 08, 055.

ATLAS Collaboration, 2016, "Estimate of the m_H shift due to interference between signal and background processes in the $H \to \gamma\gamma$ channel, for the $\sqrt{s} = 8$ TeV dataset recorded by ATLAS," Report No. ATL-PHYS-PUB-2016-009.

ATLAS Collaboration, 2018a, "Prospects for the measurement of the W-boson mass at the HL- and HE-LHC," Report No. ATL-PHYS-PUB-2018-026.

ATLAS Collaboration, 2018b, "Technical proposal: A high-granularity timing detector for the ATLAS Phase-II upgrade," Report No. LHCC-P-012.

ATLAS Collaboration 2020, "Deep sets based neural networks for impact parameter flavour tagging in ATLAS," Report No. ATL-PHYS-PUB-2020-014.

Aubert, J. J., *et al.* (E598 Collaboration), 1974, "Experimental Observation of a Heavy Particle J," Phys. Rev. Lett. **33**, 1404–1406.

Augustin, J. E., *et al.* (SLAC-SP-017 Collaboration), 1974, "Discovery of a Narrow Resonance in e^+e^- Annihilation," Phys. Rev. Lett. **33**, 1406–1408.

Avery, Paul, *et al.*, 2013, "Precision studies of the Higgs boson decay channel $H \to ZZ \to 4\ell$ with MEKD," Phys. Rev. D **87**, 055006.

Azzurri, Paolo, 2021, "The W mass and width measurement challenge at FCC-ee," Eur. Phys. J. Plus **136**, 1203.

Baak, M., J. Cúth, J. Haller, A. Hoecker, R. Kogler, K. Mönig, M. Schott, and J. Stelzer (Gfitter Group), 2014, "The global electroweak fit at NNLO and prospects for the LHC and ILC," Eur. Phys. J. C **74**, 3046.

Bach, Fabian, Bijan Chokoufé Nejad, Andre Hoang, Wolfgang Kilian, Jürgen Reuter, Maximilian Stahlhofen, Thomas Teubner, and Christian Weiss, 2018, "Fully-differential top-pair production at a lepton collider: From threshold to continuum," J. High Energy Phys. 03, 184.

Badea, Anthony, William James Fawcett, John Huth, Teng Jian Khoo, Riccardo Poggi, and Lawrence Lee, 2022, "Solving combinatorial problems at particle colliders using machine learning," Phys. Rev. D **106**, 016001.

Bae, Kyu Jung, Tae Hyun Jung, and Myeonghun Park, 2017, "Spectral Decomposition of Missing Transverse Energy at Hadron Colliders," Phys. Rev. Lett. **119**, 261801.

Baer, Howard, Vernon Barger, James S. Gainer, Peisi Huang, Michael Savoy, Dibyashree Sengupta, and Xerxes Tata, 2017, "Gluino reach and mass extraction at the LHC in radiatively-driven natural SUSY," Eur. Phys. J. C **77**, 499.

Bagnaia, P., *et al.* (UA2 Collaboration), 1983, "Evidence for $Z^0 \to e^+e^-$ at the CERN $\bar{p}p$ collider," Phys. Lett. **129B**, 130–140.

Bagnaschi, E., and A. Vicini, 2021, "Parton Density Uncertainties and the Determination of Electroweak Parameters at Hadron Colliders," Phys. Rev. Lett. **126**, 041801.

Bai, Yang, Patrick J. Fox, and Roni Harnik, 2010, "The Tevatron at the frontier of dark matter direct detection," J. High Energy Phys. 12, 048.

Ball, A., *et al.* (milliQan Collaboration), 2021, "Sensitivity to millicharged particles in future proton-proton collisions at the LHC with the milliQan detector," Phys. Rev. D **104**, 032002.

Banfi, Andrea, 2010, "Event-shape variables at hadron colliders," in *Proceedings of Physics at the LHC 2010, Hamburg, 2010*, edited by Markus Diehl, Johannes Haller, Thomas Schörner-Sadenius, and Georg Steinbruck, pp. 186–189, https://indico.desy.de/event/1964/contributions/35840/.

Banfi, Andrea, Gavin P. Salam, and Giulia Zanderighi, 2010, "Phenomenology of event shapes at hadron colliders," J. High Energy Phys. 06, 038.

Banner, M., *et al.* (UA2 Collaboration), 1983, "Observation of single isolated electrons of high transverse momentum in events with missing transverse energy at the CERN $\bar{p}p$ collider," Phys. Lett. **122B**, 476–485.

Barger, Vernon D., and R. J. N. Phillips, 1987, *Collider Physics* (Addison-Wesley, Reading, MA).

Baringer, Philip, Kyoungchul Kong, Mathew McCaskey, and Daniel Noonan, 2011, "Revisiting combinatorial ambiguities at hadron colliders with M_{T2}," J. High Energy Phys. 10, 101.

Barnard, James, Peter Cox, Tony Gherghetta, and Andrew Spray, 2016, "Long-lived, colour-triplet scalars from unnaturalness," J. High Energy Phys. 03, 003.

Barr, A. J., 2004, "Determining the spin of supersymmetric particles at the LHC using lepton charge asymmetry," Phys. Lett. B **596**, 205–212.

Barr, A. J., C. Gwenlan, C. G. Lester, and C. J. S. Young, 2011, "Comment on 'Amplification of endpoint structure for new particle mass measurement at the LHC,' " Phys. Rev. D **83**, 118701.

Barr, A. J., T. J. Khoo, P. Konar, K. Kong, C. G. Lester, K. T. Matchev, and M. Park, 2011, "Guide to transverse projections and mass-constraining variables," Phys. Rev. D **84**, 095031.

Barr, Alan, Christopher Lester, and P. Stephens, 2003, "m_{T2}: The truth behind the glamour," J. Phys. G **29**, 2343–2363.

Barr, Alan J., Ben Gripaios, and Christopher G. Lester, 2008, "Weighing wimps with kinks at colliders: Invisible particle mass measurements from endpoints," J. High Energy Phys. 02, 014.

Barr, Alan J., Ben Gripaios, and Christopher G. Lester, 2009, "Transverse masses and kinematic constraints: From the boundary to the crease," J. High Energy Phys. 11, 096.

Barr, Alan J., Sky T. French, James A. Frost, and Christopher G. Lester, 2011, "Speedy Higgs boson discovery in decays to tau lepton pairs: $h \to \tau\tau$," J. High Energy Phys. 10, 080.

Barr, Alan J., and Christopher G. Lester, 2010, "A review of the mass measurement techniques proposed for the Large Hadron Collider," J. Phys. G **37**, 123001.

Bartosik, Nazar, *et al.*, 2019, "Preliminary report on the study of beam-induced background effects at a muon collider," arXiv:1905.03725.

Bartosik, Nazar, *et al.*, 2022, "Simulated detector performance at the muon collider," arXiv:2203.07964.

Basham, C. L., L. S. Brown, S. D. Ellis, and S. T. Love, 1979, "Energy correlations in electron-positron annihilation in quantum chromodynamics: Asymptotically free perturbation theory," Phys. Rev. D **19**, 2018.

Basham, C. Louis, Lowell S. Brown, Stephen D. Ellis, and Sherwin T. Love, 1978, "Energy Correlations in Electron-Positron Annihilation: Testing QCD," Phys. Rev. Lett. **41**, 1585.

Bayatian, G. L., *et al.* (CMS Collaboration), 2007, "CMS technical design report, volume II: Physics performance," J. Phys. G **34**, 995–1579.

Behring, Arnd, Federico Buccioni, Fabrizio Caola, Maximilian Delto, Matthieu Jaquier, Kirill Melnikov, and Raoul Röntsch, 2021, "Estimating the impact of mixed QCD-electroweak corrections on the W-mass determination at the LHC," Phys. Rev. D **103**, 113002.

Belanger, Genevieve, and Jong-Chul Park, 2012, "Assisted freeze-out," J. Cosmol. Astropart. Phys. 03, 038.

Beneke, M., B. Jantzen, and P. Ruiz-Femenia, 2010, "Electroweak non-resonant NLO corrections to $e^+e^- \to W^+W^-b\bar{b}$ in the $t\bar{t}$resonance region," Nucl. Phys. **B840**, 186–213.

Beneke, M., Y. Kiyo, A. Maier, and J. Piclum, 2016, "Near-threshold production of heavy quarks with `QQbar_threshold`," Comput. Phys. Commun. **209**, 96–115.

Beneke, M., P. Marquard, P. Nason, and M. Steinhauser, 2017, "On the ultimate uncertainty of the top quark pole mass," Phys. Lett. B **775**, 63–70.

Beneke, M., J. Piclum, and T. Rauh, 2014, "P-wave contribution to third-order top-quark pair production near threshold," Nucl. Phys. **B880**, 414–434.

Beneke, M., *et al.*, 2000, "Top quark physics," in *Proceedings of the Workshop on Standard Model Physics (and More) at the LHC, Geneva, 1999*, edited by Michelangelo L. Mangano and Guido Altarelli, pp. 419–529, http://cds.cern.ch/record/429963.

Beneke, Martin, Yuichiro Kiyo, Peter Marquard, Alexander Penin, Jan Piclum, and Matthias Steinhauser, 2015, "Next-to-Next-to-Next-to-Leading Order QCD Prediction for the Top Antitop S-Wave Pair Production Cross Section near Threshold in e^+e^- Annihilation," Phys. Rev. Lett. **115**, 192001.

Berger, Joshua, Yanou Cui, and Yue Zhao, 2015, "Detecting boosted dark matter from the Sun with large volume neutrino detectors," J. Cosmol. Astropart. Phys. 02, 005.

Bernaciak, Catherine, Malte Sean Andreas Buschmann, Anja Butter, and Tilman Plehn, 2013, "Fox-Wolfram moments in Higgs physics," Phys. Rev. D **87**, 073014.

Bertolini, Daniele, Philip Harris, Matthew Low, and Nhan Tran, 2014, "Pileup per particle identification," J. High Energy Phys. 10, 059.

Bertuzzo, Enrico, Sudip Jana, Pedro A. N. Machado, and Renata Zukanovich Funchal, 2018, "Dark Neutrino Portal to Explain MiniBooNE Excess," Phys. Rev. Lett. **121**, 241801.

Betancur, Amalia, Dipsikha Debnath, James S. Gainer, Konstantin T. Matchev, and Prasanth Shyamsundar, 2019, "Measuring the mass, width, and couplings of semi-invisible resonances with the matrix element method," Phys. Rev. D **99**, 116007.

Bhardwaj, Akanksha, Partha Konar, Pankaj Sharma, and Abhaya Kumar Swain, 2019, "Exploring CP phase in τ-lepton Yukawa coupling in Higgs decays at the LHC," J. Phys. G **46**, 105001.

Bianchini, Lorenzo, and Gigi Rolandi, 2019, "A critical point in the distribution of lepton energies from the decay of a spin-1 resonance," J. High Energy Phys. 05, 044.

Birkedal, Andreas, Konstantin Matchev, and Maxim Perelstein, 2004, "Dark matter at colliders: A model independent approach," Phys. Rev. D **70**, 077701.

Bisset, M., R. Lu, and N. Kersting, 2011, "Improving SUSY spectrum determinations at the LHC with wedgebox technique," J. High Energy Phys. 05, 095.

Bjorken, J. D., and Stanley J. Brodsky, 1970, "Statistical model for electron-positron annihilation into hadrons," Phys. Rev. D **1**, 1416–1420.

Boddy, Kimberly, Jason Kumar, Danny Marfatia, and Pearl Sandick, 2018, "Model-independent constraints on dark matter annihilation in dwarf spheroidal galaxies," Phys. Rev. D **97**, 095031.

Boddy, Kimberly K., Keith R. Dienes, Doojin Kim, Jason Kumar, Jong-Chul Park, and Brooks Thomas, 2016, "Lines and boxes: Unmasking dynamical dark matter through correlations in the MeV gamma-ray spectrum," Phys. Rev. D **94**, 095027.

Boddy, Kimberly K., Keith R. Dienes, Doojin Kim, Jason Kumar, Jong-Chul Park, and Brooks Thomas, 2017, "Boxes, boosts, and energy duality: Understanding the Galactic Center gamma-ray excess through dynamical dark matter," Phys. Rev. D **95**, 055024.

Bolognesi, Sara, Yanyan Gao, Andrei V. Gritsan, Kirill Melnikov, Markus Schulze, Nhan V. Tran, and Andrew Whitbeck, 2012, "On the spin and parity of a single-produced resonance at the LHC," Phys. Rev. D **86**, 095031.

Bomark, N. E., A. Kvellestad, S. Lola, P. Osland, and A. R. Raklev, 2014, "Long lived charginos in natural SUSY?," J. High Energy Phys. 05, 007.

Boronat, Marça, Esteban Fullana, Juan Fuster, Pablo Gomis, André Hoang, Vicent Mateu, Marcel Vos, and Angelika Widl, 2020, "Top quark mass measurement in radiative events at electron-positron colliders," Phys. Lett. B **804**, 135353.

Bozzi, G., J. Rojo, and A. Vicini, 2011, "The impact of PDF uncertainties on the measurement of the W boson mass at the Tevatron and the LHC," Phys. Rev. D **83**, 113008.

Bozzi, Giuseppe, Luca Citelli, Mika Vesterinen, and Alessandro Vicini, 2015, "Prospects for improving the LHC W boson mass measurement with forward muons," Eur. Phys. J. C **75**, 601.

Bozzi, Giuseppe, Luca Citelli, and Alessandro Vicini, 2015, "Parton density function uncertainties on the W boson mass measurement from the lepton transverse momentum distribution," Phys. Rev. D **91**, 113005.

Brandt, S., C. Peyrou, R. Sosnowski, and A. Wroblewski, 1964, "The principal axis of jets: An attempt to analyze high-energy collisions as two-body processes," Phys. Lett. **12**, 57–61.

Brochet, Sébastien, Christophe Delaere, Brieuc François, Vincent Lemaître, Alexandre Mertens, Alessia Saggio, Miguel Vidal Marono, and Sébastien Wertz, 2019, "MoMEMta, a modular toolkit for the matrix element method at the LHC," Eur. Phys. J. C **79**, 126.

Burns, Michael, Kyoungchul Kong, Konstantin T. Matchev, and Myeonghun Park, 2008, "A general method for model-independent measurements of particle spins, couplings and mixing angles in cascade decays with missing energy at hadron colliders," J. High Energy Phys. 10, 081.

Burns, Michael, Kyoungchul Kong, Konstantin T. Matchev, and Myeonghun Park, 2009, "Using subsystem M_{T2} for complete mass determinations in decay chains with missing energy at hadron colliders," J. High Energy Phys. 03, 143.

Burns, Michael, Konstantin T. Matchev, and Myeonghun Park, 2009, "Using kinematic boundary lines for particle mass measurements and disambiguation in SUSY-like events with missing energy," J. High Energy Phys. 05, 094.

Butler, Joel N., and Tommaso Tabarelli de Fatis (CMS Collaboration), 2019, "A MIP timing detector for the CMS Phase-2 upgrade," Fermi National Accelerator Laboratory Report No. FERMILAB-PUB-20-718-CMS.

Butterworth, Jon, *et al.*, 2016, "PDF4LHC recommendations for LHC run II," J. Phys. G **43**, 023001.

Byers, N., and C. N. Yang, 1964, "Physical regions in invariant variables for n particles and the phase-space volume element," Rev. Mod. Phys. **36**, 595–609.

Cacciari, Matteo, Gavin P. Salam, and Gregory Soyez, 2012, "FastJet user manual," Eur. Phys. J. C **72**, 1896.

Campbell, John, Marcela Carena, Roni Harnik, and Zhen Liu, 2017, "Interference in the $gg \to h \to \gamma\gamma$ On-Shell Rate and the Higgs Boson Total Width," Phys. Rev. Lett. **119**, 181801.

Carlson, A. G., J. E. Hooper, and D. T. King, 1950, "LXIII. Nuclear transmutations produced by cosmic-ray particles of great energy.—Part V. The neutral mesons," Philos. Mag. Ser. 7 **41**, 701–724.

Catani, S., Yuri L. Dokshitzer, M. Olsson, G. Turnock, and B. R. Webber, 1991, "New clustering algorithm for multi-jet cross-sections in e^+e^- annihilation," Phys. Lett. B **269**, 432–438.

Cepeda, M., *et al.*, 2019, "Report from Working Group 2: Higgs physics at the HL-LHC and HE-LHC," CERN Yellow Rep. Monogr. **7**, 221–584.

Cesarotti, Cari, Matthew Reece, and Matthew J. Strassler, 2021, "The efficacy of event isotropy as an event shape observable," J. High Energy Phys. 07, 215.

Cesarotti, Cari, and Jesse Thaler, 2020, "A robust measure of event isotropy at colliders," J. High Energy Phys. 08, 084.

Chakraborty, Dhiman, Jacobo Konigsberg, and David L. Rainwater, 2003, "Review of top quark physics," Annu. Rev. Nucl. Part. Sci. **53**, 301–351.

Chang, Spencer, Timothy Cohen, and Bryan Ostdiek, 2018, "What is the machine learning?," Phys. Rev. D **97**, 056009.

Chatrchyan, Serguei, *et al.* (CMS Collaboration), 2011a, "Missing transverse energy performance of the CMS detector," J. Instrum. **6**, P09001.

Chatrchyan, Serguei, *et al.* (CMS Collaboration), 2011b, "Search for Supersymmetry at the LHC in Events with Jets and Missing Transverse Energy," Phys. Rev. Lett. **107**, 221804.

Chatrchyan, Serguei, *et al.* (CMS Collaboration), 2012, "Observation of a new boson at a mass of 125 GeV with the CMS experiment at the LHC," Phys. Lett. B **716**, 30–61.

Chatrchyan, Serguei, *et al.* (CMS Collaboration), 2013a, "Measurement of masses in the $t\bar{t}$ system by kinematic endpoints in pp collisions at $\sqrt{s} = 7$ TeV," Eur. Phys. J. C **73**, 2494.

Chatrchyan, Serguei, *et al.* (CMS Collaboration), 2013b, "Search for supersymmetry in final states with missing transverse energy and 0, 1, 2, or at least 3 b-quark jets in 7 TeV pp collisions using the variable α_T," J. High Energy Phys. 01, 077.

Chatrchyan, Serguei, *et al.* (CMS Collaboration), 2014, "Search for supersymmetry with razor variables in pp collisions at $\sqrt{s} = 7$ TeV," Phys. Rev. D **90**, 112001.

Chekanov, S., *et al.* (ZEUS Collaboration), 2002, "Measurement of high-Q^2 charged current cross sections in e^-P deep inelastic scattering at HERA," Phys. Lett. B **539**, 197–217.

Chen, Chunhui, 2012, "New approach to identifying boosted hadronically decaying particle using jet substructure in its center-of-mass frame," Phys. Rev. D **85**, 034007.

Cheng, Hsin-Chia, Dalit Engelhardt, John F. Gunion, Zhenyu Han, and Bob McElrath, 2008, "Accurate Mass Determinations in Decay Chains with Missing Energy," Phys. Rev. Lett. **100**, 252001.

Cheng, Hsin-Chia, and Jiayin Gu, 2011, "Measuring invisible particle masses using a single short decay chain," J. High Energy Phys. 10, 094.

Cheng, Hsin-Chia, John F. Gunion, Zhenyu Han, Guido Marandella, and Bob McElrath, 2007, "Mass determination in SUSY-like events with missing energy," J. High Energy Phys. 12, 076.

Cheng, Hsin-Chia, John F. Gunion, Zhenyu Han, and Bob McElrath, 2009, "Accurate mass determinations in decay chains with missing energy. II," Phys. Rev. D **80**, 035020.

Cheng, Hsin-Chia, and Zhenyu Han, 2008, "Minimal kinematic constraints and m_{T2}," J. High Energy Phys. 12, 063.

Cheng, Hsin-Chia, Konstantin T. Matchev, and Martin Schmaltz, 2002a, "Bosonic supersymmetry? Getting fooled at the CERN LHC," Phys. Rev. D **66**, 056006.

Cheng, Hsin-Chia, Konstantin T. Matchev, and Martin Schmaltz, 2002b, "Radiative corrections to Kaluza-Klein masses," Phys. Rev. D **66**, 036005.

Cheung, Kingman, Wai-Yee Keung, and Tzu-Chiang Yuan, 2007, "Collider Signals of Unparticle Physics," Phys. Rev. Lett. **99**, 051803.

Cho, Won Sang, Kiwoon Choi, Yeong Gyun Kim, and Chan Beom Park, 2008a, "Gluino Stransverse Mass," Phys. Rev. Lett. **100**, 171801.

Cho, Won Sang, Kiwoon Choi, Yeong Gyun Kim, and Chan Beom Park, 2008b, "Measuring superparticle masses at hadron collider using the transverse mass kink," J. High Energy Phys. 02, 035.

Cho, Won Sang, Kiwoon Choi, Yeong Gyun Kim, and Chan Beom Park, 2009, "M_{T2}-assisted on-shell reconstruction of missing momenta and its application to spin measurement at the LHC," Phys. Rev. D **79**, 031701.

Cho, Won Sang, James S. Gainer, Doojin Kim, Sung Hak Lim, Konstantin T. Matchev, Filip Moortgat, Luc Pape, and Myeonghun Park, 2016, "OPTIMASS: A package for the minimization of kinematic mass functions with constraints," J. High Energy Phys. 01, 026.

Cho, Won Sang, James S. Gainer, Doojin Kim, Konstantin T. Matchev, Filip Moortgat, Luc Pape, and Myeonghun Park, 2014, "On-shell constrained M_2 variables with applications to mass

measurements and topology disambiguation," J. High Energy Phys. 08, 070.
Cho, Won Sang, James S. Gainer, Doojin Kim, Konstantin T. Matchev, Filip Moortgat, Luc Pape, and Myeonghun Park, 2015, "Improving the sensitivity of stop searches with on-shell constrained invariant mass variables," J. High Energy Phys. 05, 040.
Cho, Won Sang, Doojin Kim, Kyoungchul Kong, Sung Hak Lim, Konstantin T. Matchev, Jong-Chul Park, and Myeonghun Park, 2016, "750 GeV Diphoton Excess May Not Imply a 750 GeV Resonance," Phys. Rev. Lett. **116**, 151805.
Cho, Won Sang, Doojin Kim, Konstantin T. Matchev, and Myeonghun Park, 2014, "Probing Resonance Decays to Two Visible and Multiple Invisible Particles," Phys. Rev. Lett. **112**, 211801.
Cho, Won Sang, Jihn E. Kim, and Ji-Hun Kim, 2010, "Amplification of endpoint structure for new particle mass measurement at the LHC," Phys. Rev. D **81**, 095010.
Cho, Won Sang, William Klemm, and Mihoko M. Nojiri, 2011, "Mass measurement in boosted decay systems at hadron colliders," Phys. Rev. D **84**, 035018.
Choi, Kiwoon, Suyong Choi, Jae Sik Lee, and Chan Beom Park, 2009, "Reconstructing the Higgs boson in dileptonic W decays at hadron collider," Phys. Rev. D **80**, 073010.
Choi, Kiwoon, Jae Sik Lee, and Chan Beom Park, 2010, "Measuring the Higgs boson mass with transverse mass variables," Phys. Rev. D **82**, 113017.
Chokoufé Nejad, Bijan, Wolfgang Kilian, Jonas M. Lindert, Stefano Pozzorini, Jürgen Reuter, and Christian Weiss, 2016, "NLO QCD predictions for off-shell $t\bar{t}$ and $t\bar{t}H$ production and decay at a linear collider," J. High Energy Phys. 12, 075.
Cieri, Leandro, Francesco Coradeschi, Daniel de Florian, and Nerina Fidanza, 2017, "Transverse-momentum resummation for the signal-background interference in the $H \to \gamma\gamma$ channel at the LHC," Phys. Rev. D **96**, 054003.
Cirigliano, Vincenzo, *et al.*, 2022, "Neutrinoless double-beta decay: A roadmap for matching theory to experiment," arXiv:2203.12169.
CMS Collaboration, 2012, "Mass determination in the $t\bar{t}$ system with kinematic endpoints," Report No. CMS-PAS-TOP-11-027.
CMS Collaboration, 2013a, "Measurement of the top quark mass using the B-hadron lifetime technique," Report No. CMS-PAS-TOP-12-030.
CMS Collaboration, 2013b, "Performance of quark/gluon discrimination in 8 TeV pp data," Report No. CMS-PAS-JME-13-002.
CMS Collaboration, 2013c, "Projected improvement of the accuracy of top-quark mass measurements at the upgraded LHC," Report No. CMS-PAS-FTR-13-017.
CMS Collaboration, 2014, "Determination of the top-quark mass from the m_{lb} distribution in dileptonic $t\bar{t}$ events at $\sqrt{s} = 8$ TeV," Report No. CMS-PAS-TOP-14-014.
CMS Collaboration, 2015, "Measurement of the top-quark mass from the b jet energy spectrum," Report No. CMS-PAS-TOP-15-002.
CMS Collaboration, 2016, "Measurement of the top quark mass in the dileptonic $t\bar{t}$ decay channel using the $M_{b\ell}$, M_{T2}, and $M_{b\ell\nu}$ observables," Report No. CMS-PAS-TOP-15-008.
CMS Collaboration, 2017, "Technical proposal for a MIP timing detector in the CMS experiment Phase 2 upgrade," Report No. LHCC-P-009.
CMS Collaboration, 2022a, "A projection of the precision of the Higgs boson mass measurement in the diphoton decay channel at the High Luminosity LHC," Report No. CMS-PAS-FTR-21-008.
CMS Collaboration, 2022b, "Projection of the Higgs boson mass and on-shell width measurements in $H \to ZZ \to 4\ell$ decay channel at the HL-LHC," Report No. CMS-PAS-FTR-21-007.
Coccaro, Andrea, David Curtin, H. J. Lubatti, Heather Russell, and Jessie Shelton, 2016, "Data-driven model-independent searches for long-lived particles at the LHC," Phys. Rev. D **94**, 113003.
Cogan, Josh, Michael Kagan, Emanuel Strauss, and Ariel Schwartzman, 2015, "Jet-images: Computer vision inspired techniques for jet tagging," J. High Energy Phys. 02, 118.
Conway, J., 1998, "PGS 4: Pretty good simulation of high energy collisions," https://conway.physics.ucdavis.edu/research/software/pgs/pgs4-general.htm.
Coradeschi, F., D. de Florian, L. J. Dixon, N. Fidanza, S. Höche, H. Ita, Y. Li, and J. Mazzitelli, 2015, "Interference effects in the $H(\to \gamma\gamma) + 2$ jets channel at the LHC," Phys. Rev. D **92**, 013004.
Corcella, Gennaro, 2019, "The top-quark mass: Challenges in definition and determination," Front. Phys. **7**, 54.
Corcella, Gennaro, Roberto Franceschini, and Doojin Kim, 2018, "Fragmentation uncertainties in hadronic observables for top-quark mass measurements," Nucl. Phys. **B929**, 485–526.
Costanzo, Davide, and Daniel R. Tovey, 2009, "Supersymmetric particle mass measurement with invariant mass correlations," J. High Energy Phys. 04, 084.
Cranmer, Kyle, Juan Pavez, and Gilles Louppe, 2015, "Approximating likelihood ratios with calibrated discriminative classifiers," arXiv:1506.02169.
Csaki, Csaba, Johannes Heinonen, and Maxim Perelstein, 2007, "Testing gluino spin with three-body decays," J. High Energy Phys. 10, 107.
Curtin, David, 2012, "Mixing it up with M_{T2}: Unbiased mass measurements at hadron colliders," Phys. Rev. D **85**, 075004.
Curtin, David, *et al.*, 2019, "Long-lived particles at the energy frontier: The MATHUSLA physics case," Rep. Prog. Phys. **82**, 116201.
Czakon, Michał, Terry Generet, Alexander Mitov, and Rene Poncelet, 2021, "B-hadron production in NNLO QCD: Application to LHC $t\bar{t}$ events with leptonic decays," J. High Energy Phys. 10, 216.
Czakon, Michał, Alexander Mitov, and Rene Poncelet, 2021, "NNLO QCD corrections to leptonic observables in top-quark pair production and decay," J. High Energy Phys. 05, 212.
Dalitz, R. H., and Gary R. Goldstein, 1992, "Decay and polarization properties of the top quark," Phys. Rev. D **45**, 1531–1543.
Dasgupta, Mrinal, and Gavin P. Salam, 2004, "Event shapes in e^+e^- annihilation and deep inelastic scattering," J. Phys. G **30**, R143.
Datta, AseshKrishna, Kyoungchul Kong, and Konstantin T. Matchev, 2005, "Discrimination of supersymmetry and universal extra dimensions at hadron colliders," Phys. Rev. D **72**, 096006.
Datta, Kaustuv, Andrew Larkoski, and Benjamin Nachman, 2019, "Automating the construction of jet observables with machine learning," Phys. Rev. D **100**, 095016.
Debnath, Dipsikha, James S. Gainer, Can Kilic, Doojin Kim, Konstantin T. Matchev, and Yuan-Pao Yang, 2016, "Identifying phase space boundaries with Voronoi tessellations," Eur. Phys. J. C **76**, 645.
Debnath, Dipsikha, James S. Gainer, Can Kilic, Doojin Kim, Konstantin T. Matchev, and Yuan-Pao Yang, 2017, "Detecting kinematic boundary surfaces in phase space: Particle mass measurements in SUSY-like events," J. High Energy Phys. 06, 092.
Debnath, Dipsikha, James S. Gainer, Can Kilic, Doojin Kim, Konstantin T. Matchev, and Yuan-Pao Yang, 2019, "Enhancing the discovery prospects for SUSY-like decays with a forgotten kinematic variable," J. High Energy Phys. 05, 008.
Debnath, Dipsikha, James S. Gainer, Doojin Kim, and Konstantin T. Matchev, 2016, "Edge detecting new physics the Voronoi way," Europhys. Lett. **114**, 41001.

Debnath, Dipsikha, Doojin Kim, Jeong Han Kim, Kyoungchul Kong, and Konstantin T. Matchev, 2017, "Resolving combinatorial ambiguities in dilepton $t\bar{t}$ event topologies with constrained M_2 variables," Phys. Rev. D **96**, 076005.

de Favereau, J., C. Delaere, P. Demin, A. Giammanco, V. Lemaître, A. Mertens, and M. Selvaggi (DELPHES 3 Collaboration), 2014, "DELPHES3, a modular framework for fast simulation of a generic collider experiment," J. High Energy Phys. 02, 057.

de Florian, Daniel, Nerina Fidanza, R. J. Hernández-Pinto, Javier Mazzitelli, Yamila Rotstein Habarnau, and German F. R. Sborlini, 2013, "A complete $O(\alpha_S^2)$ calculation of the signal-background interference for the Higgs diphoton decay channel," Eur. Phys. J. C **73**, 2387.

Delgado, Andrea, and Jesse Thaler, 2022, "Quantum annealing for jet clustering with thrust," Phys. Rev. D **106**, 094016.

deNiverville, Patrick, and Claudia Frugiuele, 2019, "Hunting sub-GeV dark matter with the NOνA near detector," Phys. Rev. D **99**, 051701.

deNiverville, Patrick, Maxim Pospelov, and Adam Ritz, 2015, "Light new physics in coherent neutrino-nucleus scattering experiments," Phys. Rev. D **92**, 095005.

De Romeri, Valentina, Kevin J. Kelly, and Pedro A. N. Machado, 2019, "DUNE-PRISM sensitivity to light dark matter," Phys. Rev. D **100**, 095010.

De Rujula, A., and A. Galindo, 2012, "Singular ways to search for the Higgs boson," J. High Energy Phys. 06, 091.

Dev, P. S. Bhupal, Doojin Kim, and Rabindra N. Mohapatra, 2016, "Disambiguating seesaw models using invariant mass variables at hadron colliders," J. High Energy Phys. 01, 118.

Dharmapalan, R., *et al.* (MiniBooNE Collaboration), 2012, "Low mass WIMP searches with a neutrino experiment: A proposal for further MiniBooNE running," https://digital.library.unt.edu/ark:/67531/metadc830679/.

Di Benedetto, V., C. Gatto, A. Mazzacane, N. V. Mokhov, S. I. Striganov, and N. K. Terentiev, 2018, "A study of muon collider background rejection criteria in silicon vertex and tracker detectors," J. Instrum. **13**, P09004.

Dienes, Keith R., Doojin Kim, Tara T. Leininger, and Brooks Thomas, 2022, "Sequential displaced vertices: Novel collider signature for long-lived particles," Phys. Rev. D **106**, 095012.

Dixon, Lance J., and Ye Li, 2013, "Bounding the Higgs Boson Width through Interferometry," Phys. Rev. Lett. **111**, 111802.

Dixon, Lance J., Ming-Xing Luo, Vladyslav Shtabovenko, Tong-Zhi Yang, and Hua Xing Zhu, 2018, "Analytical Computation of Energy-Energy Correlation at Next-to-Leading Order in QCD," Phys. Rev. Lett. **120**, 102001.

Dixon, Lance J., and M. Stewart Siu, 2003, "Resonance Continuum Interference in the Diphoton Higgs Signal at the LHC," Phys. Rev. Lett. **90**, 252001.

Djidjev, Hristo N., Guillaume Chapuis, Georg Hahn, and Guillaume Rizk, 2018, "Efficient combinatorial optimization using quantum annealing," arXiv:1801.08653.

Dolinski, Michelle J., Alan W. P. Poon, and Werner Rodejohann, 2019, "Neutrinoless double-beta decay: Status and prospects," Annu. Rev. Nucl. Part. Sci. **69**, 219–251.

Dutta, Bhaskar, Doojin Kim, Shu Liao, Jong-Chul Park, Seodong Shin, and Louis E. Strigari, 2020, "Dark Matter Signals from Timing Spectra at Neutrino Experiments," Phys. Rev. Lett. **124**, 121802.

Dutta, Bhaskar, Doojin Kim, Shu Liao, Jong-Chul Park, Seodong Shin, Louis E. Strigari, and Adrian Thompson, 2022, "Searching for dark matter signals in timing spectra at neutrino experiments," J. High Energy Phys. 01, 144.

Edelhauser, Lisa, Konstantin T. Matchev, and Myeonghun Park, 2012, "Spin effects in the antler event topology at hadron colliders," J. High Energy Phys. 11, 006.

Englert, Christoph, Michael Spannowsky, and Michihisa Takeuchi, 2012, "Measuring Higgs *CP* and couplings with hadronic event shapes," J. High Energy Phys. 06, 108.

Erdmann, Johannes, Stefan Guindon, Kevin Kroeninger, Boris Lemmer, Olaf Nackenhorst, Arnulf Quadt, and Philipp Stolte, 2014, "A likelihood-based reconstruction algorithm for top-quark pairs and the KLFitter framework," Nucl. Instrum. Methods Phys. Res., Sect. A **748**, 18–25.

Erdmann, M., E. Geiser, Y. Rath, and M. Rieger, 2019, "Lorentz boost networks: Autonomous physics-inspired feature engineering," J. Instrum. **14**, P06006.

Evans, Jared A., and Jessie Shelton, 2016, "Long-lived staus and displaced leptons at the LHC," J. High Energy Phys. 04, 056.

Farhi, Edward, 1977, "A QCD Test for Jets," Phys. Rev. Lett. **39**, 1587–1588.

Farhi, Edward, Jeffrey Goldstone, and Sam Gutmann, 2014, "A quantum approximate optimization algorithm," arXiv:1411.4028.

Faucett, Taylor, Jesse Thaler, and Daniel Whiteson, 2021, "Mapping machine-learned physics into a human-readable space," Phys. Rev. D **103**, 036020.

Feickert, Matthew, and Benjamin Nachman, 2021, "A living review of machine learning for particle physics," arXiv:2102.02770.

Feng, Jonathan L., Iftah Galon, Felix Kling, and Sebastian Trojanowski, 2018, "ForwArd Search ExpeRiment at the LHC," Phys. Rev. D **97**, 035001.

Feng, Jonathan L., *et al.*, 2023, "The Forward Physics Facility at the High-Luminosity LHC," J. Phys. G **50**, 030501.

Ferrario Ravasio, Silvia, 2019, "Top-mass observables: All-orders behaviour, renormalons and NLO + parton shower effects", Ph.D. thesis (University of Milano-Bicocca) [arXiv:1902.05035].

Ferrario Ravasio, Silvia, Tomáš Ježo, Paolo Nason, and Carlo Oleari, 2018, "A theoretical study of top-mass measurements at the LHC using NLO + PS generators of increasing accuracy," Eur. Phys. J. C **78**, 458.

Flowers, Zachary, Quinn Meier, Christopher Rogan, Dong Woo Kang, and Seong Chan Park, 2020, "Timing information at HL-LHC: Complete determination of masses of dark matter and long lived particle," J. High Energy Phys. 03, 132.

Ford, Matthew Thomas, 2004, "Studies of event shape observables with the OPAL detector at LEP", Ph.D. thesis (University of Cambridge) [arXiv:hep-ex/0405054].

Fox, Geoffrey C., and Stephen Wolfram, 1978, "Observables for the Analysis of Event Shapes in e^+e^- Annihilation and Other Processes," Phys. Rev. Lett. **41**, 1581.

Fox, Geoffrey C., and Stephen Wolfram, 1979, "Event shapes in e^+e^- annihilation," Nucl. Phys. **B149**, 413.

Franceschini, Roberto, 2017, "Energy peaks: A high energy physics outlook," Mod. Phys. Lett. A **32**, 1730034.

Franzosi, Diogo Buarque, *et al.*, 2022, "Vector boson scattering processes: Status and prospects," Rev. Phys. **8**, 100071.

Freitas, Ayres, Kyoungchul Kong, and Daniel Wiegand, 2018, "Radiative corrections to masses and couplings in universal extra dimensions," J. High Energy Phys. 03, 093.

Frixione, Stefano, and Alexander Mitov, 2014, "Determination of the top quark mass from leptonic observables," J. High Energy Phys. 09, 012.

Fuster, J., A. Irles, D. Melini, P. Uwer, and M. Vos, 2017, "Extracting the top-quark running mass using $t\bar{t}$ + 1-jet events produced at the Large Hadron Collider," Eur. Phys. J. C **77**, 794.

Gainer, James S., *et al.*, 2018, "Adding pseudo-observables to the four-lepton experimentalist's toolbox," J. High Energy Phys. 10, 073.

Gao, Yanyan, Andrei V. Gritsan, Zijin Guo, Kirill Melnikov, Markus Schulze, and Nhan V. Tran, 2010, "Spin determination of single-produced resonances at hadron colliders," Phys. Rev. D **81**, 075022.

Georgi, Howard, 2007, "Unparticle Physics," Phys. Rev. Lett. **98**, 221601.

Giunti, Carlo, Julieta Gruszko, Benjamin Jones, Lisa Kaufman, Diana Parno, and Andrea Pocar, 2022, "Report of the Topical Group on Neutrino Properties for Snowmass 2021," arXiv:2209.03340.

Gjelsten, B. K., D. J. Miller, and P. Osland, 2004, "Measurement of SUSY masses via cascade decays for SPS 1a," J. High Energy Phys. 12, 003.

Gjelsten, B. K., D. J. Miller, and P. Osland, 2005a, "Resolving ambiguities in mass determinations at future colliders," eConf **C050318**, 0211, https://www.slac.stanford.edu/econf/C050318/papers/0211.PDF.

Gjelsten, B. K., D. J. Miller, and P. Osland, 2005b, "Measurement of the gluino mass via cascade decays for SPS 1a," J. High Energy Phys. 06, 015.

Gjelsten, B. K., D. J. Miller, P. Osland, and A. R. Raklev, 2006, "Mass ambiguities in cascade decays," Conf. Proc. C **060726**, 1171–1174 [arXiv:hep-ph/0611080].

Gonçalves, Dorival, Jeong Han Kim, Kyoungchul Kong, and Yongcheng Wu, 2022, "Direct Higgs-top *CP*-phase measurement with $t\bar{t}h$ at the 14 TeV LHC and 100 TeV FCC," J. High Energy Phys. 01, 158.

Gonçalves, Dorival, Kyoungchul Kong, and Jeong Han Kim, 2018, "Probing the top-Higgs Yukawa *CP* structure in dileptonic $t\bar{t}h$ with M_2-assisted reconstruction," J. High Energy Phys. 06, 079.

Goodman, Jessica, Masahiro Ibe, Arvind Rajaraman, William Shepherd, Tim M. P. Tait, and Hai-Bo Yu, 2010, "Constraints on dark matter from colliders," Phys. Rev. D **82**, 116010.

Graesser, Michael L., and Jessie Shelton, 2013, "Hunting Mixed Top Squark Decays," Phys. Rev. Lett. **111**, 121802.

Gripaios, Ben, 2008, "Transverse observables and mass determination at hadron colliders," J. High Energy Phys. 02, 053.

Gritsan, Andrei V., Jeffrey Roskes, Ulascan Sarica, Markus Schulze, Meng Xiao, and Yaofu Zhou, 2020, "New features in the JHU generator framework: Constraining Higgs boson properties from on-shell and off-shell production," Phys. Rev. D **102**, 056022.

Grojean, Christophe, Ayan Paul, and Zhuoni Qian, 2021, "Resurrecting $b\bar{b}h$ with kinematic shapes," J. High Energy Phys. 04, 139.

Grossman, Yuval, Mario Martone, and Dean J. Robinson, 2011, "Kinematic edges with flavor oscillation and non-zero widths," J. High Energy Phys. 10, 127.

Guadagnoli, Diego, and Chan Beom Park, 2014, "M_{T2}-reconstructed invisible momenta as spin analizers, and an application to top polarization," J. High Energy Phys. 01, 030.

Guest, Dan, Kyle Cranmer, and Daniel Whiteson, 2018, "Deep learning and its application to LHC physics," Annu. Rev. Nucl. Part. Sci. **68**, 161–181.

Han, Tao, 2005, "Collider phenomenology: Basic knowledge and techniques," in *Proceedings of the Theoretical Advanced Study Institute in Elementary Particle Physics (TASI 2004): Physics in D≥4*, edited by John Terning, Carlos E. M. Wagner, and Dieter Zeppenfeld (World Scientific, Singapore), pp. 407–454.

Han, Tao, Ian-Woo Kim, and Jeonghyeon Song, 2010, "Kinematic cusps: Determining the missing particle mass at colliders," Phys. Lett. B **693**, 575–579.

Han, Tao, Ian-Woo Kim, and Jeonghyeon Song, 2013, "Kinematic cusps with two missing particles. I: Antler decay topology," Phys. Rev. D **87**, 035003.

Herb, S. W., *et al.*, 1977, "Observation of a Dimuon Resonance at 9.5 GeV in 400-GeV Proton-Nucleus Collisions," Phys. Rev. Lett. **39**, 252–255.

Hewett, JoAnne L., Ben Lillie, Manuel Masip, and Thomas G. Rizzo, 2004, "Signatures of long-lived gluinos in split supersymmetry," J. High Energy Phys. 09, 070.

Hill, C. S., J. R. Incandela, and J. M. Lamb, 2005, "Method for measurement of the top quark mass using the mean decay length of b hadrons in $t\bar{t}$ events," Phys. Rev. D **71**, 054029.

Hinchliffe, I., F. E. Paige, M. D. Shapiro, J. Soderqvist, and W. Yao, 1997, "Precision SUSY measurements at CERN LHC," Phys. Rev. D **55**, 5520–5540.

Hoang, A. H., and T. Teubner, 1998, "Top quark pair production at threshold: Complete next-to-next-to-leading order relativistic corrections," Phys. Rev. D **58**, 114023.

Hoang, A. H., and T. Teubner, 1999, "Top quark pair production close to threshold: Top mass, width and momentum distribution," Phys. Rev. D **60**, 114027.

Hoang, André H., 2014, "The top mass: Interpretation and theoretical uncertainties," arXiv:1412.3649.

Hoang, André H., 2020, "What is the top quark mass?," Annu. Rev. Nucl. Part. Sci. **70**, 225–255.

Hoang, André H., and Maximilian Stahlhofen, 2014, "The top-antitop threshold at the ILC: NNLL QCD uncertainties," J. High Energy Phys. 05, 121.

Hoeche, Stefan, Frank Krauss, Nils Lavesson, Leif Lonnblad, Michelangelo Mangano, Andreas Schalicke, and Steffen Schumann, 2005, "Matching parton showers and matrix elements," in *Proceedings of HERA and the LHC: A Workshop on the Implications of HERA for LHC Physics, Geneva, 2004–2005*, edited by A. De Roeck and H. Jung, pp. 288–289, http://cds.cern.ch/record/926597.

Huang, Li, Su-beom Kang, Jeong Han Kim, Kyoungchul Kong, and Jun Seung Pi, 2022, "Portraying double Higgs at the Large Hadron Collider II," J. High Energy Phys. 08, 114.

Huang, P., N. Kersting, and H. H. Yang, 2008, "Hidden thresholds: A technique for reconstructing new physics masses at hadron colliders," arXiv:0802.0022.

Hubisz, Jay, Joseph Lykken, Maurizio Pierini, and Maria Spiropulu, 2008, "Missing energy look-alikes with 100 pb^{-1} at the LHC," Phys. Rev. D **78**, 075008.

Husemann, Ulrich, 2017, "Top-quark physics: Status and prospects," Prog. Part. Nucl. Phys. **95**, 48–97.

Idaszek, Berenika, 2019, "Reconstruction of the neutrino momentum in top pair aassociated Higgs boson production using deep learning," bachelor's thesis (RWTH Aachen University).

Izaguirre, Eder, Gordan Krnjaic, Philip Schuster, and Natalia Toro, 2014, "Physics motivation for a pilot dark matter search at Jefferson Laboratory," Phys. Rev. D **90**, 014052.

Jackson, Paul, and Christopher Rogan, 2017, "Recursive jigsaw reconstruction: HEP event analysis in the presence of kinematic and combinatoric ambiguities," Phys. Rev. D **96**, 112007.

Ježo, Tomáš, Jonas M. Lindert, Paolo Nason, Carlo Oleari, and Stefano Pozzorini, 2016, "An NLO + PS generator for $t\bar{t}$ and Wt production and decay including non-resonant and interference effects," Eur. Phys. J. C **76**, 691.

Jung, Philipp, 2019, "A deep learning based reconstruction of two neutrinos in the di-lepton decays of top quark pairs with the CMS experiment," bachelor's thesis (RWTH Aachen University).

Jungman, Gerard, Marc Kamionkowski, and Kim Griest, 1996, "Supersymmetric dark matter," Phys. Rep. **267**, 195–373.

Kachulis, C., *et al.* (Super-Kamiokande Collaboration), 2018, "Search for Boosted Dark Matter Interacting with Electrons in Super-Kamiokande," Phys. Rev. Lett. **120**, 221301.

Kagan, Michael, 2022, "Image-based jet analysis," in *Artificial Intelligence for High Energy Physics*, edited by Paolo Calafiura, David Rousseau, and Kazuhiro Terao (World Scientific, Singapore), pp. 439–496.

Karapostoli, Georgia, 2008, "Observation and measurement of the supersymmetric process $\tilde{\chi}_2^0 \to \tilde{\chi}_1^0 \ell\ell$ with the CMS experiment at LHC," Ph.D. thesis (University of Athens).

Kawabata, S., Y. Shimizu, Y. Sumino, and H. Yokoya, 2013, "Measurement of physical parameters with a weight function method and its application to the Higgs boson mass reconstruction," J. High Energy Phys. 08, 129.

Kawabata, Sayaka, Yasuhiro Shimizu, Yukinari Sumino, and Hiroshi Yokoya, 2015, "Weight function method for precise determination of top quark mass at Large Hadron Collider," Phys. Lett. B **741**, 232–238.

Kawabata, Sayaka, and Hiroshi Yokoya, 2017, "Top-quark mass from the diphoton mass spectrum," Eur. Phys. J. C **77**, 323.

Kawagoe, K., M. M. Nojiri, and G. Polesello, 2005, "New SUSY mass reconstruction method at the CERN LHC," Phys. Rev. D **71**, 035008.

Kehoe, R., M. Narain, and A. Kumar, 2008, "Review of top quark physics results," Int. J. Mod. Phys. A **23**, 353–470.

Khachatryan, Vardan, *et al.* (CMS Collaboration), 2015a, "Search for long-lived neutral particles decaying to quark-antiquark pairs in proton-proton collisions at $\sqrt{s} = 8$ TeV," Phys. Rev. D **91**, 012007.

Khachatryan, Vardan, *et al.* (CMS Collaboration), 2015b, "Search for supersymmetry using razor variables in events with b-tagged jets in pp collisions at $\sqrt{s} = 8$ TeV," Phys. Rev. D **91**, 052018.

Khachatryan, Vardan, *et al.* (CMS Collaboration), 2016, "Measurement of the top quark mass using charged particles in pp collisions at $\sqrt{s} = 8$ TeV," Phys. Rev. D **93**, 092006.

Kharchilava, Avto, 2000, "Top mass determination in leptonic final states with J/ψ," Phys. Lett. B **476**, 73–78.

Kilic, Can, Lian-Tao Wang, and Itay Yavin, 2007, "On the existence of angular correlations in decays with heavy matter partners," J. High Energy Phys. 05, 052.

Kim, Doojin, 2016, "Distinguishing dark matter stabilization symmetries at hadron colliders," AIP Conf. Proc. **1743**, 020007.

Kim, Doojin, and Kyoungchul Kong, 2015, "Kinematic discrimination of tW and $t\bar{t}$ productions using initial state radiation," Phys. Lett. B **751**, 512–524.

Kim, Doojin, Kyoungchul Kong, Konstantin T. Matchev, Myeonghun Park, and Prasanth Shyamsundar, 2023, "Deep-learned event variables for collider phenomenology," Phys. Rev. D **107**, L031904.

Kim, Doojin, Hye-Sung Lee, and Myeonghun Park, 2015, "Invisible dark gauge boson search in top decays using a kinematic method," J. High Energy Phys. 03, 134.

Kim, Doojin, and Konstantin T. Matchev, 2018, "How to prove that a E_T excess at the LHC is not due to dark matter," Phys. Rev. D **98**, 055018.

Kim, Doojin, Konstantin T. Matchev, Filip Moortgat, and Luc Pape, 2017, "Testing invisible momentum ansatze in missing energy events at the LHC," J. High Energy Phys. 08, 102.

Kim, Doojin, Konstantin T. Matchev, and Myeonghun Park, 2016, "Using sorted invariant mass variables to evade combinatorial ambiguities in cascade decays," J. High Energy Phys. 02, 129.

Kim, Doojin, Konstantin T. Matchev, and Prasanth Shyamsundar, 2019, "Kinematic focus point method for particle mass measurements in missing energy events," J. High Energy Phys. 10, 154.

Kim, Doojin, and Jong-Chul Park, 2015, "An alternative interpretation for cosmic ray peaks," Phys. Lett. B **750**, 552–558.

Kim, Doojin, and Jong-Chul Park, 2016, "Energy peak: Back to the Galactic Center GeV gamma-ray excess," Phys. Dark Universe **11**, 74–78.

Kim, Doojin, Jong-Chul Park, and Seodong Shin, 2017, "Dark Matter 'Collider' from Inelastic Boosted Dark Matter," Phys. Rev. Lett. **119**, 161801.

Kim, Ian-Woo, 2010, "Algebraic Singularity Method for Mass Measurement with Missing Energy," Phys. Rev. Lett. **104**, 081601.

Kim, Jeong Han, Minho Kim, Kyoungchul Kong, Konstantin T. Matchev, and Myeonghun Park, 2019, "Portraying double Higgs at the Large Hadron Collider," J. High Energy Phys. 09, 047.

Kim, Jeong Han, Kyoungchul Kong, Konstantin T. Matchev, and Myeonghun Park, 2019, "Probing the Triple Higgs Self-Interaction at the Large Hadron Collider," Phys. Rev. Lett. **122**, 091801.

Kim, Minho, Pyungwon Ko, Jae-hyeon Park, and Myeonghun Park, 2021, "Leveraging quantum annealer to identify an event-topology at high energy colliders," arXiv:2111.07806.

Klimek, Matthew D., 2022, "The time substructure of jets and boosted object tagging," J. Phys. G **49**, 045008.

Kogler, Roman, *et al.*, 2019, "Jet substructure at the Large Hadron Collider: Experimental review," Rev. Mod. Phys. **91**, 045003.

Komiske, Patrick T., Eric M. Metodiev, Benjamin Nachman, and Matthew D. Schwartz, 2017, "Pileup mitigation with machine learning (PUMML)," J. High Energy Phys. 12, 051.

Komiske, Patrick T., Eric M. Metodiev, and Matthew D. Schwartz, 2017, "Deep learning in color: Towards automated quark/gluon jet discrimination," J. High Energy Phys. 01, 110.

Komiske, Patrick T., Eric M. Metodiev, and Jesse Thaler, 2018, "Energy flow polynomials: A complete linear basis for jet substructure," J. High Energy Phys. 04, 013.

Komiske, Patrick T., Eric M. Metodiev, and Jesse Thaler, 2019, "Energy flow networks: Deep sets for particle jets," J. High Energy Phys. 01, 121.

Konar, Partha, Kyoungchul Kong, and Konstantin T. Matchev, 2009, "$\sqrt{\hat{s}}_{\min}$: A global inclusive variable for determining the mass scale of new physics in events with missing energy at hadron colliders," J. High Energy Phys. 03, 085.

Konar, Partha, Kyoungchul Kong, Konstantin T. Matchev, and Myeonghun Park, 2010a, "Dark matter particle spectroscopy at the LHC: Generalizing M_{T2} to asymmetric event topologies," J. High Energy Phys. 04, 086.

Konar, Partha, Kyoungchul Kong, Konstantin T. Matchev, and Myeonghun Park, 2010b, "Superpartner Mass Measurement Technique Using 1D Orthogonal Decompositions of the Cambridge Transverse Mass Variable M_{T2}," Phys. Rev. Lett. **105**, 051802.

Konar, Partha, Kyoungchul Kong, Konstantin T. Matchev, and Myeonghun Park, 2011, "RECO level $\sqrt{s}_{\min}$ and subsystem $\sqrt{\hat{s}}_{\min}$: Improved global inclusive variables for measuring the new physics mass scale in E_T events at hadron colliders," J. High Energy Phys. 06, 041.

Konar, Partha, and Abhaya Kumar Swain, 2016a, "Mass reconstruction with M_2 under constraint in semi-invisible production at a hadron collider," Phys. Rev. D **93**, 015021.

Konar, Partha, and Abhaya Kumar Swain, 2016b, "Reconstructing semi-invisible events in resonant tau pair production from Higgs," Phys. Lett. B **757**, 211–215.

Konar, Partha, and Abhaya Kumar Swain, 2017, "Mass restricting variables in semi-invisible production at the LHC," Pramana **89**, 56.

Kong, Kyoungchul, Gopolang Mohlabeng, and Jong-Chul Park, 2015, "Boosted dark matter signals uplifted with self-interaction," Phys. Lett. B **743**, 256–266.

Lally, Colin H., and Christopher G. Lester, 2012, "Properties of M_{T2} in the massless limit," arXiv:1211.1542.

LeCompte, Thomas J., and Stephen P. Martin, 2011, "Large Hadron Collider reach for supersymmetric models with compressed mass spectra," Phys. Rev. D **84**, 015004.

Lee, Jason Sang Hun, Inkyu Park, Ian James Watson, and Seungjin Yang, 2020, "Zero-permutation jet-parton assignment using a self-attention network," arXiv:2012.03542.

Lee, Lawrence, Christian Ohm, Abner Soffer, and Tien-Tien Yu, 2019, "Collider searches for long-lived particles beyond the standard model," Prog. Part. Nucl. Phys. **106**, 210–255.

Lenz, Alexander, Michael Spannowsky, and Gilberto Tetlalmatzi-Xolocotzi, 2018, "Double-charming Higgs boson identification using machine-learning assisted jet shapes," Phys. Rev. D **97**, 016001.

Lester, C. G., and D. J. Summers, 1999, "Measuring masses of semi-invisibly decaying particles pair produced at hadron colliders," Phys. Lett. B **463**, 99–103.

Lester, Christopher, and Alan Barr, 2007, "MTGEN: Mass scale measurements in pair-production at colliders," J. High Energy Phys. 12, 102.

Lester, Christopher G., 2011, "The stransverse mass, M_{T2}, in special cases," J. High Energy Phys. 05, 076.

Lester, Christopher G., and Benjamin Nachman, 2015, "Bisection-based asymmetric M_{T2} computation: A higher precision calculator than existing symmetric methods," J. High Energy Phys. 03, 100.

Lester, Christopher Gorham, 2001, "Model independent sparticle mass measurements at ATLAS," Ph.D. thesis (University of Cambridge).

Lim, Sung Hak, 2016, "Identifying the production process of new physics at colliders; symmetric or asymmetric?," J. High Energy Phys. 06, 105.

Linthorne, Dylan, and Daniel Stolarski, 2021, "Triggering on emerging jets," Phys. Rev. D **104**, 035019.

Liu, Jia, Zhen Liu, and Lian-Tao Wang, 2019, "Enhancing Long-Lived Particles Searches at the LHC with Precision Timing Information," Phys. Rev. Lett. **122**, 131801.

Liu, Zhen, and Brock Tweedie, 2015, "The fate of long-lived superparticles with hadronic decays after LHC run 1," J. High Energy Phys. 06, 042.

Lonnblad, Leif, 1994, "CLHEP: A project for designing a C++ class library for high-energy physics," Comput. Phys. Commun. **84**, 307–316.

Low, F. E., 1958, "Bremsstrahlung of very low-energy quanta in elementary particle collisions," Phys. Rev. **110**, 974–977.

Low, Ian, 2013, "Polarized charginos (and top quarks) in scalar top quark decays," Phys. Rev. D **88**, 095018.

Mahbubani, Rakhi, Konstantin T. Matchev, and Myeonghun Park, 2013, "Re-interpreting the Oxbridge stransverse mass variable M_{T2} in general cases," J. High Energy Phys. 03, 134.

Maier, A., 2020, "Top pair production and mass determination," CERN Yellow Rep. Monogr. **3**, 117–122.

Maltoni, F., 2013, "Basics of QCD for the LHC," in *Proceedings of the 7th CERN–Latin-American School of High-Energy Physics (CLASHEP 2013), Arequipa, Peru, 2013*, edited by M. Mulders and G. Perez (CERN, Geneva), https://indico.cern.ch/event/208901/contributions/1501065/attachments/323330/450947/Maltoni_L2.pdf.

Maltoni, F., *et al.*, 2022, "TF07 Snowmass report: Theory of collider phenomena," arXiv:2210.02591.

Martin, Stephen P., 2007, "Compressed supersymmetry and natural neutralino dark matter from top squark-mediated annihilation to top quarks," Phys. Rev. D **75**, 115005.

Martin, Stephen P., 2012, "Shift in the LHC Higgs diphoton mass peak from interference with background," Phys. Rev. D **86**, 073016.

Martin, Stephen P., 2013, "Interference of Higgs diphoton signal and background in production with a jet at the LHC," Phys. Rev. D **88**, 013004.

Matchev, Konstantin T., Filip Moortgat, and Luc Pape, 2019, "Dreaming awake: Disentangling the underlying physics in case of a SUSY-like discovery at the LHC," J. Phys. G **46**, 115002.

Matchev, Konstantin T., Filip Moortgat, Luc Pape, and Myeonghun Park, 2009, "Precise reconstruction of sparticle masses without ambiguities," J. High Energy Phys. 08, 104.

Matchev, Konstantin T., Filip Moortgat, Luc Pape, and Myeonghun Park, 2010, "Precision sparticle spectroscopy in the inclusive same-sign dilepton channel at LHC," Phys. Rev. D **82**, 077701.

Matchev, Konstantin T., and Myeonghun Park, 2011, "General Method for Determining the Masses of Semi-Invisibly Decaying Particles at Hadron Colliders," Phys. Rev. Lett. **107**, 061801.

Matchev, Konstantin T., Alexander Roman, and Prasanth Shyamsundar, 2020, "Finding wombling boundaries in LHC data with Voronoi and Delaunay tessellations," J. High Energy Phys. 12, 137.

Matchev, Konstantin T., and Prasanth Shyamsundar, 2020, "Singularity variables for missing energy event kinematics," J. High Energy Phys. 04, 027.

Matchev, Konstantin T., and Prasanth Shyamsundar, 2021, "OASIS: Optimal analysis-specific importance sampling for event generation," SciPost Phys. **10**, 034.

Matsumoto, Shigeki, Mihoko M. Nojiri, and Daisuke Nomura, 2007, "Hunting for the top partner in the littlest Higgs model with T parity at the CERN LHC," Phys. Rev. D **75**, 055006.

Meade, Patrick, Matthew Reece, and David Shih, 2010, "Long-lived neutralino NLSPs," J. High Energy Phys. 10, 067.

Mikos, Patryk, and Elzbieta Richter-Was, 2015, "AcerDET-2.0[1]: A particle level fast simulation and reconstruction package for phenomenological studies on high p_T physics at LHC," arXiv:1507.00995.

Miller, D. J., P. Osland, and A. R. Raklev, 2006, "Invariant mass distributions in cascade decays," J. High Energy Phys. 03, 034.

Mirabelli, Eugene A., Maxim Perelstein, and Michael E. Peskin, 1999, "Collider Signatures of New Large Space Dimensions," Phys. Rev. Lett. **82**, 2236–2239.

Moult, Ian, Lina Necib, and Jesse Thaler, 2016, "New angles on energy correlation functions," J. High Energy Phys. 12, 153.

Mulders, M., and G. Perez, 2015, Eds., *Proceedings of the 7th CERN–Latin-American School of High-Energy Physics (CLASHEP2013), Arequipa, Peru, 2013* (CERN, Geneva), https://cds.cern.ch/record/1484921.

Nachman, Ben, *et al.*, 2022, "Jets and jet substructure at future colliders," Front. Phys. **10**, 897719.

Necib, Lina, Jarrett Moon, Taritree Wongjirad, and Janet M. Conrad, 2017, "Boosted dark matter at neutrino experiments," Phys. Rev. D **95**, 075018.

Nojiri, M. M., G. Polesello, and D. R. Tovey, 2003, "Proposal for a new reconstruction technique for SUSY processes at the LHC," in *Proceedings of the 3rd Les Houches Workshop on Physics at TeV Colliders, Les Houches, France, 2003*, edited by G. Belanger, F. Boudjema, J. P. Guillet, and E. Pilon [arXiv:hep-ph/0312317].

Nojiri, Mihoko M., Giacomo Polesello, and Daniel R. Tovey, 2008, "A Hybrid method for determining SUSY particle masses at the

LHC with fully identified cascade decays," J. High Energy Phys. 05, 014.

Nojiri, Mihoko M., Daisuke Toya, and Tomio Kobayashi, 2000, "Lepton energy asymmetry and precision SUSY study at hadron colliders," Phys. Rev. D **62**, 075009.

Nowak, Kacper, and Aleksander Filip Zarnecki, 2021, "Optimising top-quark threshold scan at CLIC using genetic algorithm," J. High Energy Phys. 07, 070.

Okabe, Atsuyuki, Barry Boots, and Kokichi Sugihara, 1992, *Spatial Tessellations: Concepts and Applications of Voronoi Diagrams* (John Wiley & Sons, New York).

Papaefstathiou, Andreas, and Bryan Webber, 2009, "Effects of QCD radiation on inclusive variables for determining the scale of new physics at hadron colliders," J. High Energy Phys. 06, 069.

Park, Chan Beom, 2011, "Reconstructing the heavy resonance at hadron colliders," Phys. Rev. D **84**, 096001.

Park, Chan Beom, 2020, "A singular way to search for heavy resonances in missing energy events," J. High Energy Phys. 07, 089.

Park, Chan Beom, 2021a, "Could M_{T2} be a singularity variable?," J. High Energy Phys. 11, 042.

Park, Chan Beom, 2021b, "`YAM2`: Yet another library for the M_2 variables using sequential quadratic programming," Comput. Phys. Commun. **264**, 107967.

Perazzini, Stefano, Fabio Ferrari, and Vincenzo Maria Vagnoni (LHCb ECAL Upgrade-2 R&D Group), 2022, "Development of an MCP-based timing layer for the LHCb ECAL Upgrade-2," Instruments **6**, 7.

Perelstein, Maxim, 2011, "Introduction to collider physics," in *Physics of the Large and the Small: Proceeding of the Theoretical Advanced Study Institute in Elementary Particle Physics (TASI 2009)*, edited by Csaba Csaki and Scott Dodelson (World Scientific, Singapore), pp. 421–486.

Pili, Martina (LHCb Collaboration), 2019, "Towards a W boson mass measurement with LHCb," Proc. Sci., DIS2019, 131 [arXiv:1907.02029].

Pinfold, James, *et al.* (MoEDAL Collaboration), 2009, "Technical design report of the MoEDAL experiment," CERN Reports No. CERN-LHCC-2009-006 and No. MoEDAL-TDR-001.

Pires, Diogo, Pedrame Bargassa, João Seixas, and Yasser Omar, 2021, "A digital quantum algorithm for jet clustering in high-energy physics," arXiv:2101.05618.

Pires, Diogo, Yasser Omar, and João Seixas, 2023, "Adiabatic quantum algorithm for multijet clustering in high energy physics," Phys. Lett. B **843**, 138000.

Randall, Lisa, and David Tucker-Smith, 2008, "Dijet Searches for Supersymmetry at the LHC," Phys. Rev. Lett. **101**, 221803.

Richter-Was, Elzbieta, 2002, "`AcerDET`: A particle level fast simulation and reconstruction package for phenomenological studies on high p_T physics at LHC," arXiv:hep-ph/0207355.

Rizzi, Andrea, Fabrizio Palla, and Gabriele Segneri, 2006, "Track impact parameter based b-tagging with CMS," CERN Technical Report No. CERN-CMS-NOTE-2006-019.

Robens, Tania, 2012, "$\sqrt{\hat{s}}_{\min}$ resurrected," J. High Energy Phys. 02, 051.

Rogan, Christopher, 2010, "Kinematical variables towards new dynamics at the LHC," arXiv:1006.2727.

Ross, Graham G., and Mario Serna, 2008, "Mass determination of new states at hadron colliders," Phys. Lett. B **665**, 212–218.

Rujula, A., and A. Galindo, 2011, "Measuring the W-boson mass at a hadron collider: A study of phase-space singularity methods," J. High Energy Phys. 08, 023.

Schael, S., *et al.* (ALEPH, DELPHI, L3, and OPAL Collaborations and LEP Electroweak Working Group), 2013, "Electroweak measurements in electron-positron collisions at W-boson-pair energies at LEP," Phys. Rep. **532**, 119–244.

Schwaller, Pedro, Daniel Stolarski, and Andreas Weiler, 2015, "Emerging Jets," J. High Energy Phys. 05, 059.

Schwartz, Matthew D., 2018, "TASI lectures on collider physics," in *Proceedings of the Theoretical Advanced Study Institute in Elementary Particle Physics (TASI 2016): Anticipating the Next Discoveries in Particle Physics, Boulder, CO, 2016*, edited by Rouven Essig and Ian Low (World Scientific, Singapore), pp. 65–100.

Seidel, K., F. Simon, and M Tesar, 2012, "Prospects for the measurement of the top mass in a threshold scan at CLIC and ILC," CERN Report No. LCD-Note-2012-013, https://cds.cern.ch/record/1498599/files/LCD-2012-013.pdf.

Seidel, Katja, Frank Simon, Michal Tesar, and Stephane Poss, 2013, "Top quark mass measurements at and above threshold at CLIC," Eur. Phys. J. C **73**, 2530.

Shimmin, Chase, and Daniel Whiteson, 2016, "Boosting low-mass hadronic resonances," Phys. Rev. D **94**, 055001.

Shmakov, Alexander, Michael James Fenton, Ta-Wei Ho, Shih-Chieh Hsu, Daniel Whiteson, and Pierre Baldi, 2022, "SPANet: Generalized permutationless set assignment for particle physics using symmetry preserving attention," SciPost Phys. **12**, 178.

Sirunyan, Albert M., *et al.* (CMS Collaboration), 2017a, "Measurement of the top quark mass in the dileptonic $t\bar{t}$ decay channel using the mass observables $M_{b\ell}$, M_{T2}, and $M_{b\ell\nu}$ in pp collisions at $\sqrt{s} = 8$ TeV," Phys. Rev. D **96**, 032002.

Sirunyan, Albert M., *et al.* (CMS Collaboration), 2017b, "Search for dark matter and unparticles in events with a Z boson and missing transverse momentum in proton-proton collisions at $\sqrt{s} = 13$ TeV," J. High Energy Phys. 03, 061.

Sirunyan, Albert M., *et al.* (CMS Collaboration), 2017c, "Search for dark matter produced with an energetic jet or a hadronically decaying W or Z boson at $\sqrt{s} = 13$ TeV," J. High Energy Phys. 07, 014.

Sirunyan, Albert M., *et al.* (CMS Collaboration), 2017d, "Search for new physics in the monophoton final state in proton-proton collisions at $\sqrt{s} = 13$ TeV," J. High Energy Phys. 10, 073.

Sirunyan, Albert M., *et al.* (CMS Collaboration), 2019a, "Inclusive search for supersymmetry in pp collisions at $\sqrt{s} = 13$ TeV using razor variables and boosted object identification in zero and one lepton final states," J. High Energy Phys. 03, 031.

Sirunyan, Albert M., *et al.* (CMS Collaboration), 2019b, "Search for new particles decaying to a jet and an emerging jet," J. High Energy Phys. 02, 179.

Sirunyan, Albert M., *et al.* (CMS Collaboration), 2020a, "A measurement of the Higgs boson mass in the diphoton decay channel," Phys. Lett. B **805**, 135425.

Sirunyan, Albert M., *et al.* (CMS Collaboration), 2020b, "Measurement of the Jet Mass Distribution and Top Quark Mass in Hadronic Decays of Boosted Top Quarks in pp Collisions at $\sqrt{s} =$ TeV," Phys. Rev. Lett. **124**, 202001.

Sirunyan, Albert M., *et al.* (CMS Collaboration), 2020c, "Search for dark matter particles produced in association with a Higgs boson in proton-proton collisions at $\sqrt{s} = 13$ TeV," J. High Energy Phys. 03, 025.

Sirunyan, Albert M., *et al.* (CMS Collaboration), 2021a, "Search for dark matter produced in association with a leptonically decaying Z boson in proton-proton collisions at $\sqrt{s} = 13$ TeV," Eur. Phys. J. C **81**, 13.

Sirunyan, Albert M., *et al.* (CMS Collaboration), 2021b, "Search for long-lived particles using displaced jets in proton-proton collisions at $\sqrt{s} = 13$ TeV," Phys. Rev. D **104**, 012015.

Smillie, Jennifer M., and Bryan R. Webber, 2005, "Distinguishing spins in supersymmetric and universal extra dimension models at the large hadron collider," J. High Energy Phys. 10, 069.

Smith, J., W. L. van Neerven, and J. A. M. Vermaseren, 1983, "Transverse Mass and Width of the W Boson," Phys. Rev. Lett. **50**, 1738–1740.

Soyez, Grégory, 2019, "Pileup mitigation at the LHC: A theorist's view," Phys. Rep. **803**, 1–158.

Stewart, Iain W., Frank J. Tackmann, and Wouter J. Waalewijn, 2010, "N Jettiness: An Inclusive Event Shape to Veto Jets," Phys. Rev. Lett. **105**, 092002.

Strassler, Matthew J., and Michael E. Peskin, 1991, "Threshold production of heavy top quarks: QCD and the Higgs boson," Phys. Rev. D **43**, 1500–1514.

Swain, Abhaya Kumar, and Partha Konar, 2015, "Constrained $\sqrt{\hat{S}_{\min}}$ and reconstructing with semi-invisible production at hadron colliders," J. High Energy Phys. 03, 142.

Thaler, Jesse, and Ken Van Tilburg, 2011, "Identifying boosted objects with N-subjettiness," J. High Energy Phys. 03, 015.

Tovey, D. R., 2001, "Measuring the SUSY mass scale at the LHC," Phys. Lett. B **498**, 1–10.

Tovey, Daniel R., 2008, "On measuring the masses of pair-produced semi-invisibly decaying particles at hadron colliders," J. High Energy Phys. 04, 034.

Tucker-Smith, David, and Neal Weiner, 2001, "Inelastic dark matter," Phys. Rev. D **64**, 043502.

Tumasyan, Armen, *et al.* (CMS Collaboration), 2021a, "Search for Long-Lived Particles Decaying in the CMS End Cap Muon Detectors in Proton-Proton Collisions at $\sqrt{s} = 13$ TeV," Phys. Rev. Lett. **127**, 261804.

Tumasyan, Armen, *et al.* (CMS Collaboration), 2021b, "Search for new particles in events with energetic jets and large missing transverse momentum in proton-proton collisions at $\sqrt{s} = 13$ TeV," J. High Energy Phys. 11, 153.

Wang, Lian-Tao, and Itay Yavin, 2007, "Spin measurements in cascade decays at the LHC," J. High Energy Phys. 04, 032.

Webber, Bryan, 2009, "Mass determination in sequential particle decay chains," J. High Energy Phys. 09, 124.

Weber, Matthias, 2011, "Measurement of hadronic event shapes with the CMS detector in 7 TeV pp collisions at the LHC," Ph.D. thesis (ETH Zurich).

Weber, Matthias A. (CMS Collaboration), 2009, "Hadronic event shapes at CMS," in *Proceedings of the 17th International Workshop on Deep-Inelastic Scattering and Related Subjects, Madrid, 2009* (Science Wise Publishing, Berlin), p. 82.

Wei, Annie Y., Preksha Naik, Aram W. Harrow, and Jesse Thaler, 2020, "Quantum algorithms for jet clustering," Phys. Rev. D **101**, 094015.

Wells, Pippa, 2014, "Pileup mitigation at the HL-LHC," lecture, 2nd ECFA High Luminosity LHC Experiments Workshop, Aix-les-Bains, France, 2014, https://cds.cern.ch/record/1957370/files/ATL-PHYS-SLIDE-2014-753.pdf.

Zaheer, Manzil, Satwik Kottur, Siamak Ravanbakhsh, Barnabas Poczos, Russ R. Salakhutdinov, and Alexander J. Smola, 2017, "Deep sets," in *Advances in Neural Information Processing Systems*, Vol. 30, edited by I. Guyon, U. Von Luxburg, S. Bengio, H. Wallach, R. Fergus, S. Vishwanathan, and R. Garnett (Curran Associates, Red Hook, NY).

Zyla, P. A., *et al.* (Particle Data Group), 2020, "Review of particle physics," Prog. Theor. Exp. Phys. 083C01.